UNIVERSIDAD DE CHILE
FACULTAD DE CIENCIAS FÍSICAS Y MATEMÁTICAS
DEPARTAMENTO DE GEOLOGÍA

CHEMICAL WEATHERING RATES IN CONTINENTAL VOLCANIC ARCS AND THEIR IMPLICATIONS IN THE GLOBAL CYCLE OF CO₂: INSIGHTS FROM THE SOUTHERN ANDES (38°-42° S)

TESIS PARA OPTAR AL GRADO DE MAGÍSTER EN CIENCIAS, MENCIÓN GEOLOGÍA
MEMORIA PARA OPTAR AL TÍTULO DE GEÓLOGA

AMANDA SOFÍA PEÑA ECHEVERRÍA

PROFESORA GUÍA:
ALIDA PÉREZ FODICH

MIEMBROS DE LA COMISIÓN:
LINDA DANIELE
DANIELE TARDANI

SANTIAGO DE CHILE
2023

TASAS DE METEORIZACIÓN QUÍMICA EN ARCOS VOLCÁNICOS CONTINENTALES Y SU IMPLICANCIA EN EL CICLO DEL CO_2: PERSPECTIVAS DESDE LOS ANDES DEL SUR (38°–42°S)

Esta investigación evalúa el impacto de los flujos de meteorización de silicatos en las tasas de consumo de CO_2 dentro de la Zona Volcánica del Sur Central de los Andes (ZVSC) (38–42°S). El área de estudio abarca 22 cuencas hidrográficas y 16 fuentes termales. El objetivo es mejorar la comprensión de los procesos de meteorización en regiones volcánicas y la influencia que ejercen los sistemas hidrotermales mediante el uso de trazadores geoquímicos. Este enfoque también contribuye a establecer una línea base hidrogeoquímica en la región.

Los trazadores químicos seleccionados (B, Cl, $\delta^{13}C$, $\delta^{11}B$, Ge/Si) diferencian eficazmente los ríos influenciados por la actividad hidrotermal. Se identificaron aportes hidrotermales en 14 de las 22 cuencas analizadas. Para estos ríos, se utilizan las relaciones X_{ion}/Cl y Ge/Si como trazadores para estimar las cargas disueltas de origen hidrotermal, obteniendo un promedio de 11% en la ZVSC. Combinando las concentraciones de solutos en los ríos con los caudales anuales para cada cuenca, fue posible calcular los flujos de meteorización química, obteniendo una tasa de flujo de solutos de 33 a 386 ton/km²/año. Los flujos de meteorización para cada cuenca se utilizaron para extrapolar el flujo total de consumo de carbono por meteorización para la ZVSC. Considerando la extensión total de la ZVSC (78,617 km2), el flujo total de consumo de carbono por meteorización es de 0.11 x 10^{12} mol/año, equivalente a 0.0013 PgC/año. Éste representa alrededor del 1% del carbono global consumido por la meteorización de los continentes. Los análisis de $\delta^{13}C$ permiten establecer que la contribución de CO_2 atmosférico en la meteorización de las rocas de la ZVS, es notablemente inferior del total de solutos, equivalente al ~60-90% del flujo de alcalinidad de la región.

Este estudio revela que una parte sustancial del carbono magmático se retiene como carbono inorgánico disuelto en aguas continentales en lugar de liberarse como CO_2 a la atmósfera. Además, subraya la importancia de estudiar arcos volcánicos continentales a gran escala para mejorar nuestra comprensión en los procesos de meteorización de silicatos y su rol en el ciclo global del carbono.

CHEMICAL WEATHERING RATES IN CONTINENTAL VOLCANIC ARCS AND THEIR IMPLICATIONS IN THE GLOBAL CYCLE OF CO_2: INSIGHTS FROM THE SOUTHERN ANDES (38°-42° S)

This research assesses the impact of silicate weathering fluxes on CO_2 consumption rates within the Central Southern Volcanic Zone (CSVZ) of the Andes (38-42°S). The study area comprises 22 watersheds and 16 hydrothermal manifestations. This thesis aims to improve our comprehension of weathering processes in volcanic regions and the influence of hydrothermal systems by employing distinct geochemical tracers. This approach also contributes to establishing a hydrogeochemical baseline within the area.

Selected chemical tracers (B, Cl, $\delta^{13}C$, $\delta^{11}B$, Ge/Si) effectively differentiate rivers influenced by hydrothermal activity. Hydrothermal input was observed in 14 of 22 rivers. I used X_{ion}/Cl ratios and Ge/Si as tracers to estimate the hydrothermal input in the dissolved load of the watersheds in the CSVZ, which in average amounts to 11%. I combined river solute concentrations with annual discharge at each catchment to estimate chemical weathering fluxes, yielding silicate export rates that range between 33 to 386 ton/km^2/yr in the studied watersheds. Using the silicate export rates, I calculate the total carbon consumption via weathering of the total CSVZ area (78,617 km^2). As a result, the total weathering carbon consumption via weathering in the CSVZ is 0.11x 10^{12} mol/yr, equivalent to 0.0013 PgC/yr, which is around 1% of the global carbon silicate weathering on the continents. The $\delta^{13}C$ analyses show that the contribution of atmospheric CO_2 to the weathering of rocks in the CSVZ is notably lower than that of the total budget, equivalent to ~60 to 90% of alkalinity flux in the region.

This study reveals that a substantial portion of magmatic carbon is retained as dissolved inorganic carbon in continental waters rather than released as CO_2 to the atmosphere. Moreover, it underscores the significance of studying large-scale continental volcanic arcs to enhance our understanding of silicate weathering's feedback in the global carbon cycle.

"...Las interacciones entre todos estos elementos, entre lo vivo y lo no vivo, conforman un equilibrio de flujos muy sutiles. Para que una gota de agua pase a convertirse en la lágrima de un animal hay un proceso muy complejo de por medio"

Adriana Hoffmann

Agradecimientos

Daniele Tardani, Gerdhard Jessen, Pablo Sánchez, Fernanda Álvarez y Francisco Delgado que nos acompañaron y colaboraron en gran parte de las campañas de terreno enseñándome las curiosidades de los sistemas hidrotermales en el sur de nuestro país. Agradezco de manera especial a todas las personas que voluntariamente y con muchas ganas de aprender nos ayudaron a realizar cada uno de los terrenos, en especial a todas esas lindas personas que conocí de la Universidad Austral. Por último, y dado que nada de esto hubiese pasado sin ella, me gustaría agradecer a mi profesora guía: Dra. Alida Pérez. Ella regresó el año 2020 al departamento con un perfil de investigación que me causó curiosidad de manera inmediata, hablaba de temas nuevos y encajaba con mi inquietud de interdisciplina. Gracias Profe por haber confiado en mí, por entregarme tantas oportunidades y haber hecho de este magíster una experiencia desafiante, novedosa e increíble (aunque a veces estresante). Sobre todo, gracias por haberme mostrado la academia y la geología desde una nueva perspectiva.

En segundo lugar, gracias a mis amigos que sin ellos Plan Común no hubiese sido lo mismo, gracias por los viajes que tuvimos y los que vendrán, gracias por las horas de estudios, los carretes, las conversas, el apañe y el cariño (Contre, Waton, Nati, Oscarito, Tole, Cami, Maru, Colo, Coto, Nibaldo). Gracias a las cabras de futbolito, por las pichangas y haberme

TABLE OF CONTENT

List of Tables

List of Figures

Chapter 1 : Introduction

1.1. Motivation

The weathering of rocks and the transport of chemicals from rivers to the ocean fulfill a fundamental function in nutrient supply and the morphology of the Earth's surface. Understanding the impact of various system variables, such as discharge (Godsey et al., 2009; Harrison et al., 2005; Hem, 1948, 1985; Johnson et al., 1969), land cover (Mattsson et al., 2005), vegetation (Gislason et al., 1996; Kardjilov et al., 2006), precipitation (Clair et al., 1999), temperature (Brady, 1991; Brady et al., 1999; Velbel, 1993) and winter snowpack (Clair & Ehrman, 1998) on chemical fluxes is essential, especially in global warming and uncertain future climate scenarios. Active volcanic provinces, mainly those rich in mafic rocks, play a prominent role in chemical weathering fluxes (Dessert et al., 2009; Gaillardet et al., 2011; Gaspard et al., 2021; Hartmann, 2009; Louvat & Allegre, 1997; Rad et al., 2007; Schopka et al., 2011; Schopka & Derry, 2012). The reactive volcanic glass, presence of acid gases, and frequent volcanic eruptions make these regions major contributors to weathering processes, serving as significant sources of rock-derived nutrients transported from streams to oceans. Additionally, the mineralogical composition of volcanic regions promotes the consumption of CO_2 in continental waters, enhancing their impact on biogeochemical cycles. The focus of previous studies on volcanic weathering fluxes has mainly been on intra-plate oceanic volcanoes and island arcs. Gislason et al. (1996) was the first in determine the chemical weathering rates for Iceland (59 t/km²/yr), these authors and following studies (Eiriksdottir et al., 2008; Gislason et al., 2009; Louvat et al., 2008) showed the dependence with runoff, vegetation cover, physical erosion, and the age of the drained rocks. Louvat & Allegre (1997) were the first assessment chemical weathering rates of 110 t/km²/yr in Reunion Island, and for the Azores archipelago with a silicate weathering rate of 26-50 t/km²/yr (Louvat & Allegre, 1998). Multiple studies have focused on the island arc made by the Antilles archipelago, where several authors have determined a wide range of weathering rates, from 50 to 400 t/km²/yr (Dessert et al., 2015; Goldsmith et al., 2010; Jones et al., 2011; Rad et al., 2006, 2007). Weathering rates in the Philippines are among the highest measured from rivers, with up to 100-400 t/km²/yr (Schopka et al., 2011). The case of New Zealand was studied by Goldsmith et al. (2008) and the chemical weathering rates obtained were 15-300 t/km²/yr. Hawaii island was

studied by Dessert et al. (2003) and Schopka & Derry (2012) where was concluded a chemical weathering rate of 34.4 t/km2/yr while the CO_2 consumption from streams and surface water budgets is 618 x 10^6 mol/yr. Hartmann (2009) determined the CO_2 consumed by chemical weathering in the Japanese archipelago, obtaining 6.05tC/ km²/yr, the rate is 3.2 time above the global average, then in Hartmann et al. (2010) studied the predictive variations in river flows of silica and showed that the Japanese archipelago is a hyperactive region with a DSi performance 6.6 higher than the world average. In contrast, limited attention has been given to continental volcanic arcs. Only a few recent studies have reported chemical weathering rates from river solutes draining other continental arc regions: Dessert et al. (2009) determine a chemical weathering rate in Kamchatka of 23-29 t/km²/yr, Central America was studied in central Nicaragua by Carey et al. (2015) and in west-central Panama by Harmon et al. (2016), the silicate weathering rates correspond to 28 and 6.9-70 t/km²/yr respectively. Moreover, in Cascade, Rasmussen et al. (2010) evaluated the climatic controls of weathering and pedogenic processes on basalt-derived soil, demonstrating the limitations of processes in low and high elevations for water availability and soil temperature. The continental volcanic arcs show an opportunity to understand the variability in weathering rates due to distinctive environmental and climatological conditions, in addition to having large extensions that allow increasing the scale of the studies.

In this study, we focus on characterizing the weathering budget from the Southern Andean Volcanic Zone, ubicated between 33° and 46°S and an extension of 1,400 km. This continental volcanic arc has been characterized as one of the most active volcanic regions (Galetto et al., 2023) with high precipitation rates of >2000 mm/yr and numerous catchments feeding larger rivers draining towards the ocean. The tectonic setting provides a high magma extrusion rate, highlighting its central zone (37°S–42°S) with a rate of 14.9 km³/km/Ma (Jacques et al., 2014; Völker et al., 2011) due to decreasing crustal thickness (Tassara & Yañez, 2003). Additionally, this region hosts more than 200 hydrothermal manifestations (Hauser, 1997). Volcanic gases and hydrothermal waters can increase rock weathering in active volcanic regions and add dissolved solutes to surface waters. The compositional variability of the hydrothermal springs is explained by different structural domains controlling the permeability of the hydrothermal reservoirs, which allow for varying degrees of interaction between superficial and deep fluids (Daniele et al., 2020; Roquer et al., 2017; Sánchez-Alfaro et al., 2013; Wrage et al., 2017). Despite the numerous of studies focused on these hydrothermal manifestations (Daniele et al., 2020; Held et al., 2018; Pérez-Estay et al., 2022; Pérez-Flores et al., 2016, 2017; Pérez-Moreno et al., 2021; Ray et al., 2009; Risacher et al., 2011; Roquer

et al., 2017; Sánchez-Alfaro et al., 2013; Tardani et al., 2016; Wrage et al., 2017), none of the aforementioned studies have explored the interaction between rivers and hydrothermal waters in the area.

Our research provides a deeper insight into understanding the natural solute fluxes resulting from the weathering of Southern Andean arc that affect biogeochemical cycles of rock-derived elements delivered to the Pacific Ocean. This study is the first to quantify chemical weathering fluxes from rivers draining volcanic watersheds in the Southern Andes. Additionally, we use several geochemical tracers (Ge, δ^{11}B, δ^{13}C) to investigate the influence of hydrothermal activity on weathering fluxes. A total of 22 volcanic basins and 16 hot springs were selected and sampled during dry and rainy seasons to quantify the solute fluxes and their sources. This approach will shed light on the role of continental arcs and hydrothermal activity in CO_2 consumption rates. Furthermore, this research provides a geochemical environmental baseline for water and geothermal resource management and preservation in the Chilean Southern Andes.

1.2. Background

1.2.1. Weathering fluxes in volcanic regions

Two distinct processes explain the global carbon cycle: (1) The short-term cycle is active in the surface reservoirs only (oceans, atmosphere, biosphere, and soils), where organic and inorganic carbon is transferred between reservoirs at rates ranging from seconds to decades and millennia. (2) The long-term carbon cycle is controlled by two major processes that act as carbon sinks for the CO_2 released from volcanic and metamorphic degassing and petrogenic organic matter oxidation (Berner, 1992). The first process is organic carbon burial of plant and microbial photosynthetic products (France-Lanord & Derry, 1997). The second process is weathering silicate rocks, transforming carbon dioxide in the atmosphere into alkalinity (Kump et al., 2000). These two processes act as the significant temperature-stabilizing mechanisms at geological timescales because of their capability to offset elevated CO_2 concentrations in the atmosphere (Berner et al., 1983; Hilton & West, 2020; Holland, 1978; Kump et al., 2000; Royer et al., 2007; Walker et al., 1981). Weathering of silicate rocks participates in the carbon cycle by neutralizing carbonic acid (H_2CO_3) that forms when CO_2 in the atmos-

phere dissolves in rainfall and freshwater. The primary reaction during the chemical weathering of rocks is the dissolution of primary minerals, which leads to the export of soluble cations and the precipitation of clays. As an example, the congruent dissolution of forsterite and anorthite:

Reaction (1) $MgSiO_{4(s)} + 4CO_{2(g)} + 4H_2O \rightarrow 2Mg^{2+}_{(aq)} + 4HCO_3^{-}_{(aq)} + H_4SiO_{4(aq)}$

Reaction (2) $CaAl_2Si_2O_{8(s)} + 2CO_{2(g)} + 3H_2O \rightarrow Ca^{2+}_{(aq)} + 2HCO_3^{-}_{(aq)} + Al_2Si_2O_5(OH)_{4(s)}$
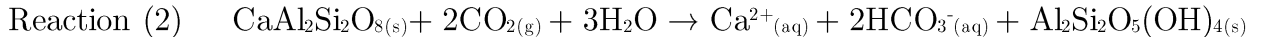
During the dissolution of one mole of olivine (Reaction (1)), four moles of atmospheric carbon are neutralized, and removed from the atmosphere in the aqueous solution as bicarbonate. Furthermore, two moles of magnesium and one mole of silicic acid are released into the solution. It is important to note that no solid products -such as clays- are formed, and thus, weathering of forsterite proceeds congruently. In the case of reaction (2), the Ca-feldspar dissolves incongruently: releasing solutes and precipitating secondary minerals (kaolinite). One mole of Ca-feldspar mineral dissolution neutralizes two moles of atmospheric carbon upon dissolution. The complete sequestration of atmospheric carbon occurs when carbonate minerals precipitate in the ocean as organisms utilize the released alkalinity and divalent cations to construct carbonate shells, such as $CaCO_3$ or $MgCO_3$. However, the dissolution of silicate minerals containing alkalis (Na and K) is a less efficient mechanism for neutralizing and sequestering CO_2 in the form of carbonate minerals. Reactions (1) and (2) highlight the influence of various lithologies on the global carbon cycle, as silicate rocks consist of different combinations of silicate minerals with diverse compositions. As a result, weathering reactions involving different types of rocks contribute to varying extents to CO_2 consumption.

Estimating global atmospheric CO_2 consumption rates from silicate weathering involves calculating weathering fluxes from continental-scale reactions. Garrels & Mackenzie (1971), using elemental dissolved concentrations in river geochemistry, made initial estimates. Subsequently, global weathering and atmospheric CO_2 budgets used data from the largest rivers of the world (e.g., Meybeck, 1987; Gaillardet et al., 1999; Moon et al., 2014). These rivers cover extensive areas of the continental crust and capture many surface processes. However, integrating diverse lithologies and chemical reactions within these rivers presents challenges. Negrel et al. (1993) developed an inverse method to allocate different solutes to various sources,

including rainfall, atmospheric deposition, and different lithologies (such as silicates and car-bonates), utilizing the measured elemental ratios and Sr-isotopic composition in the rivers and those know from the different reservoirs. This method was further applied by Gaillardet et al. (1999) for global weathering fluxes, and several authors have applied it to regional studies (Burke et al., 2018; Dellinger et al., 2014; Jiang et al., 2020; Kemeny & Torres, 2021; Louvat & Allegre, 1997; Moon et al., 2014; Moquet et al., 2011; Negrel et al., 1993; Negrel & Des-champs, 1996; Roy et al., 1999). Some of these studies have focused on catchments dominated by basaltic rocks, revealing the significant role of weathering fluxes from these regions in consuming atmospheric CO_2 (Balagizi et al., 2015; Dessert et al., 2001, 2015; Eiriksdottir et al., 2013, 2015; Gaillardet et al., 2011; Gislason et al., 1996; Grard et al., 2005; Ibarra et al., 2016; Louvat & Allegre, 1997, 1998; Pokrovsky et al., 2005; Schopka et al., 2011; Schopka & Derry, 2012). The relevance of the volcanic regions in weathering fluxes results from the abundance of mafic to intermediate volcanic deposits containing reactive silicates rich in Mg, Ca, and Fe(II) compared to alkali silicates in felsic rocks (Horton et al., 1999; Ibarra et al., 2016; Vasyukova et al., 2019; Wymore et al., 2017). The presence of reactive volcanic glass in these rocks further enhances their dissolution. To calculate the silicate weathering rates (W) it is crucial to determine the solute flux provided by each of the solute sources (atmospheric, lithological, and hydrothermal). By multiplying the concentration of a given element X (X=$SiO_{2(aq)}$, HCO_3^-, Na^+, K^+, Ca^{2+}, Mg^{2+}, Cl^-, SO_4^{2-}) with the discharge water from a water-shed (Q), the flux (F) of that element can be established (Eq (1)). In the silicate weathering flux, the riverine dissolved solutes will come from silicate minerals (X_{rock}) and is calculated multiplying by Q/A, representing the mean annual runoff (Q) normalized for the area (A), to compare watersheds/regions (Eq (2)).

$$F = [X] \text{ x } Q \qquad (1)$$

$$W \text{ (mol/yr/km}^2) = [X_{rock}] \text{ x } (Q/A) \qquad (2)$$

Rivers draining active volcanic regions contribute significantly to the global flux of so-lutes to the ocean (Dessert et al., 2003; Gaillardet et al., 2011; Goldsmith et al., 2008; Jones et al., 2011; Schopka et al., 2011). Due to the presence of hydrothermal fluid circulation in these systems, it is important to consider their potential influence on the high weathering rates observed. In active volcano-hydrothermal systems, a significant portion, around 40%, of river solutes originates from reactions involving high-temperature water(gas)-rock interactions

(Dessert et al., 2009; Gaillardet et al., 2011; Henchiri et al., 2014; Ide et al., 2018; Louvat et al., 2008, 2011, 2014; Louvat & Allegre, 1997, 1998; Rivé et al., 2013). These reactions can result from the release of CO_2 from magma or deep crustal rocks through processes such as metamorphism. (Dessert et al., 2009; Gaillardet et al., 2011; Hurwitz et al., 2010; Rivé et al., 2013; Schopka et al., 2011). In addition, other acids, particularly chloridric and sulfuric acids can further enhance weathering rates. These reactions involve the dissolution of rocks by the hydrothermal acid inputs and the precipitation of secondary minerals (Giggenbach, 1988). Thus, to estimate the atmospheric CO_2 consumption rates in volcanic provinces, it is necessary to quantify the effect of hydrothermal activity on the solute chemical weathering flux (Gaillardet et al., 2011; Gaspard et al., 2021; Schopka et al., 2011). Estimating hydrothermal inputs to river waters and how much these consume magmatic CO_2 through weathering is not straightforward; as many of the magmatic or volcanic sources of acidity are also supplied by atmospheric inputs (CO_2), sulfate from human activities, oceans or magmatic source, or chloride from oceans and magmatic gases. The first and most straightforward method is to study catchments with and without the influence of geothermal systems (e.g., Gaspard et al., 2021; Gislason et al., 1996). However, this approach requires independent knowledge to discriminate between both groups. Another well-developed approach is based on allocating elemental ratios based on a chloride mass balance (using X/Cl ratios, with X = [HCO_3, SO_4, Na, Ca, Mg, SiO_2(aq)]) (Dessert et al., 2009, 2015; Gaillardet, et al., 2011; Hurwitz et al., 2010; Louvat et al., 2008; Louvat & Allegre, 1997, 1998). This approach allows quantifying the hydrothermal influence, however since Cl^- can also be of volcanic origin, this method might underestimate hydrothermal additions (Hurwitz et al., 2010). Additionally, other authors have used different geochemical tracers to allocate the hydrothermal input. Evans et al. (2004) determine the thermal input using Ge/Si ratios, assuming the Ge/Si in the stream is the weighted sum of the hot spring and rock weathering contributions and that Ge and Si behave conservatively while mixing. Both tracers (Cl and Ge/Si) have limitations, which depend on their behavior in relation to other processes that may affect the solutes in rivers and streams (for example, vegetation, residence time, young volcanic deposits). Therefore, in heterogeneous region, a combination of multiple tracers and major element chemical compositions normalized to a dominant ion (e.g., X/Na) might yield better results, particularly applying an inverse method to quantify hydrothermal fluxes (e.g., Gaillardet et al., 1999; Negrel et al., 1993 ; Roy et al., 1999; Louvat and Allegre, 1997; Moquet et al., 2011; Dellinger et al., 2014; Moon et al., 2014; Burke et al., 2018; Jiang et al., 2020; Kemeny and Torres, 2021).

Isotopic systems such as boron isotopes (δ^{11}B), carbon isotopes (δ^{13}C), and the relation between Ge and Si have shown promising results, as both systems have distinctive magmatic/hydrothermal signatures in comparison to atmospheric inputs (Figure 1). Boron is used in geochemistry to understand processes such as water-rock interactions and biogeochemical cycling (Palmer and Sturchio, 1990; Cividini et al., 2010; Gaillardet & Lemarchand, 2018; Lemarchand & Gaillardet, 2006; Rose et al., 2000; Schmitt et al., 2012). At low temperatures, boron is adsorbed and incorporated into clay minerals or adsorbed on clays and ferric oxides/hydroxides (Goldberg & Glaubig, 1985; Harder, 1970), with the light ^{10}B isotope preferentially uptaken into these phases, leaving dissolved boron enriched in ^{11}B (~30‰; Cividini et al., 2010; Marschall & Foster, 2018). However, the mixing between weathering reactions, atmospheric input, and biological recycling, results in rivers with δ^{11}B values in a range from -6‰ to 44‰ (Chetelat et al., 2009; Chetelat & Gaillardet, 2005; Lemarchand et al., 2002; Lemarchand & Gaillardet, 2006; Marschall & Foster, 2018; Rose et al., 2000; Spivack et al., 1987). In the case of hydrothermal waters, the fractionation of boron isotopes is due to the separation of water vapor and the interaction with altered secondary minerals (Palmer et al., 1987; Spivack et al., 1987). This last mechanism is not uncommon; however, it does not lead to significant changes in boron isotopic composition (Aggarwal et al., 2000). As a result, the boron isotope values found in geothermal waters are primarily influenced by the δ^{11}B signatures of their deeper sources: such as magmatic fluids given that δ^{11}B in MORB and mantle is uniform at -7±1‰ (Marschall et al., 2017); or the lithology of the reservoir rocks (-20‰ to 10‰; Marschall & Jiang, 2011; Pennisi et al., 2006; Vengosh et al., 1994; Xiao et al., 2013). Complementarily Ge/Si ratios have been used to trace weathering and the silicon cycle in active volcano-hydrothermal systems (e.g., Arnórsson, 1984; Escoube et al., 2015; Gaspard et al., 2021; Siebert et al., 2006). Different types of silicate rocks show Ge/Si ratios ranging from ~1 to 3 µmol/mol (Bernstein, 1985; Argollo & Schilling, 1978; Mortlock & Froelich, 1987; He et al., 2019; Kurtz et al., 2002). During incongruent weathering, Ge is partitioned between the fluid phase and secondary minerals, as Ge is preferentially incorporated into the solid phase (Kurtz et al., 2002). This results in high Ge/Si ratios (>3 µmol/mol) in soils and regolith, and low Ge/Si ratios in most river catchments fed by baseflow (0.1-3 µmol/mol; see Anders et al., 2003; Baronas, 2017; Baronas et al., 2018; Froelich et al., 1985, 1992; Kurtz et al., 2002, 2011; Lugolobi et al., 2010; Meek et al., 2016; Mortlock & Froelich, 1987; Murnane & Stallard, 1990). Ge/Si values measured in unpolluted (no fly-ash contamination) rivers reflect the mixing in both processes during incongruent weathering of primary silicates and the later congruent dissolution of secondary clays (Froelich et al., 1992; Kurtz et al., 2002;

Mortlock & Froelich, 1987; Murnane & Stallard, 1990). However, high Ge/Si ratios in unpolluted stream waters, higher than those observed in silicate rocks, indicate either, the influence of solutes from geothermal systems (3-185 μmol/mol, in basalt-andesite terrains; see Arnórsson, 1984; Escoube et al., 2015; Gaspard et al., 2021; Siebert et al., 2006; Wheat et al., 2008), and/or sulfide weathering (Anders et al., 2003; Evans et al., 2004; Evans & Derry, 2002; Han et al., 2015; Mortlock & Froelich, 1987; Rosenberg, 2009). The combination of these processes and sources results in a large range reported for rivers draining other volcanic regions, mainly with basalt-andesite compositions (Ge/Si = 0.16-20 μmol/mol; e.g., Baronas et al., 2018, 2020; Derry et al., 2005; Scribner et al., 2006). Finally, carbon isotopes are used as tracers to determine the origin of carbon consumed by weathering reactions (Telmer and Veizer, 1999; Becker et al., 2008; Rivé et al., 2013; Evans et al., 2006; Liu et al., 2022). They differentiate between biogenic CO_2 produced by ecosystem respiration (organic matter decompositions and root respiration) and carbonate dissolution in soils ($< -26‰$, Cerling, 1984; O'leary, 1988), as well as magmatic (from $-10‰$ to $-5‰$, Giggenbach et al., 1983) and atmospheric sources ($\sim -7‰$, Cerling, 1984; Cerling et al., 1991; Giggenbach, 1988; O'leary, 1988). In volcanic contexts, carbon isotopes help to determine the deep carbon and the relationship between heat flux and degassing processes, in addition to evidencing the effect of calcite precipitation on the rise and mixing of hydrothermal fluids with meteoric water (e.g., Chiodini et al., 1998,2011; Evans et al., 2004; Frondini et al., 2008; Appelo y Postma, 2005). Unlike the other two tracers, in the CSVZ, $\delta^{13}C$ data from hot springs have been reported ($-7.45‰$ and $-9.75‰$; Pérez-Moreno et al., 2021; Tardani et al., 2016).
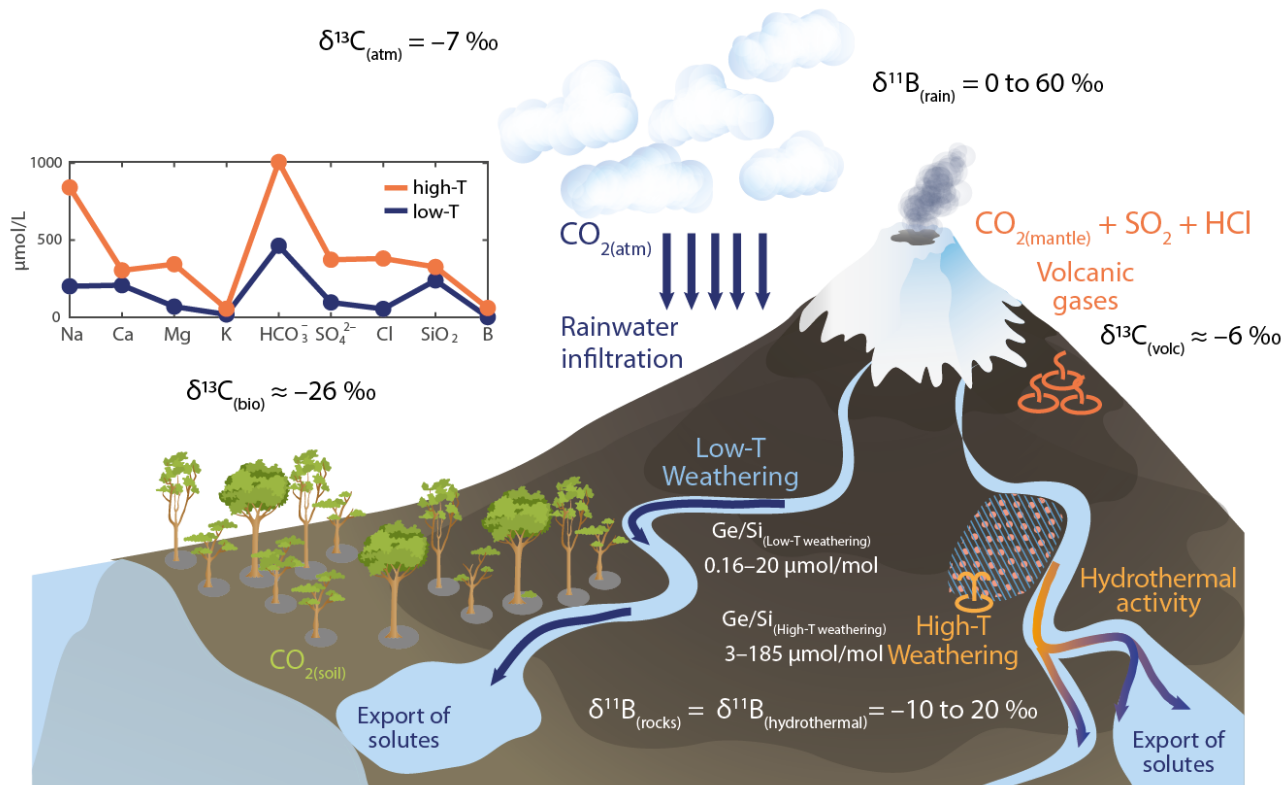
Figure 1: Silicate weathering processes occurring in volcanic regions. Low-temperature weathering results from the interaction of rainfall with atmospheric and soil CO_2, and mineral dissolution. High-T weathering results from the addition of volcanic gases and hydrothermal activity adding CO_2, SO_2 and HCl, and interaction with bedrock. Each reservoir contributing to weathering fluxes is characterized by a range in $\delta^{11}B$ (Marschall & Foster, 2018), $\delta^{13}C$ (Rivé et al., 2013) isotopic compositions and Ge/Si ratios obtained from thermal springs interacting with basalt and basalt-andesite rocks and rivers draining that type of lithology (Gaspard et al., 2021). The solute export diagram shows the expected concentrations of cations and anions (µmol/L) from both low-T and high-T weathering pools based on Dessert et al. (2009). Emphasis is placed on the relative proportions of these pools. The volcanic landscape cartoon is adapted from Sabine et al., (2013) and Perez-Fodich (Fondecyt Iniciación 2020).

1.2.2. Previous studies in South Volcanic Zone (SVZ)

The South Volcanic Zone (SVZ) of Chile extends from the central Chilean Andes at 33°S to the Aysén Region at 46°S. This region is characterized by high volcanic, seismic, and hydrothermal activity, driven by the oblique convergence between the Nazca and South American plates. (e.g., Cembrano & Lara, 2009; Galetto et al., 2023; Rosenau et al., 2006). Subduction occurs at 7 to 9 cm/yr adjacent to all parts of this segment-giving rise to ~60 recently

active volcanic centers as well as three giant silicic caldera systems (Stern, 2004). The present research focuses on the Central South Volcanic Zone (CSVZ) located between 38° and 42°S. This area presents the highest magma extrusion rate (14.9 km3/km/Ma) in the Andes and the SVZ (Galetto et al., 2023; Jacques et al., 2014; Völker et al., 2011). Volcanic products of different compositions cover the basement rocks, with basalts and basaltic-andesites being the most common compositions (Hickey-Vargas et al., 2016; Lara et al., 2006). These volcanic materials have been erupted from Pleistocene-Quaternary stratovolcanoes and monogenetic cones in the region (López-Escobar, 1984) and exhibit primitive magmatic signatures (Cembrano & Lara, 2009; Lara et al., 2006). The basement in this section of volcanic arc (38°S-42°S) is composed of the North Patagonian Batholith, described as plutonic belt of diorites, tonalites, granodiorites and granites emplaced during the Jurassic-Neogene period (Adriasola et al., 2006; Lara et al., 2004; Munizaga et al., 1988; Pankhurst et al., 1999; Suárez & De la Cruz, 2001).

In the last 15 years there have been notable advancements in understanding the formation of the hydrothermal systems in the CSVZ, focusing on the controls of the different fluid compositions (Daniele et al., 2020; Held et al., 2018; Pérez-Estay et al., 2022; Pérez-Flores et al., 2016, 2017; Pérez-Moreno et al., 2021; Ray et al., 2009; Risacher et al., 2011; Roquer et al., 2017; Sánchez-Alfaro et al., 2013; Tardani et al., 2016; Wrage et al., 2017). However, most of them have been oriented to geothermal sources for energy uses, and the efforts have focused on building a model that allows an understanding of the circulation of the thermal fluids through the fractured rocks, tephra layers, and sediments (e.g., Daniele et al., 2020; Pérez-Estay et al., 2022; Pérez-Moreno et al., 2021). All these authors agree that inherent differences between structural domains are observed in the chemical and isotopic composition of associated geothermal fluids, being evident in conservative element ratios such as Cl/B (Sánchez-Alfaro et al., 2013; Wrage et al., 2017), and the isotopic signature of specific volatile components (Ray et al., 2009; Tardani et al., 2016). Broadly speaking, there are two types of hydrothermal manifestations with contrasting chemical compositions: (1) A first group of neutral to high pH waters (7-10), with high Cl/B ratios (~50) and strong correlation between Li, Cs, Rb and Cl. This cluster is associated with Liquiñe Ofqui Fault System (LOFS), one of the regional-scale fault systems (extension of 1,200 km) (Adriasola et al., 2006; Arancibia et al., 1999; Cembrano, Hervé, et al., 1996; Melnick et al., 2006; Rosenau et al., 2006). The predominant mechanism of heat transfer in these systems is thermal conduction from crystalline host rock, and the chemical composition of discharging springs is a product

of heat-fluid-rock interaction at depth after the infiltration of meteoric water in vertical permeability of the basement (Sánchez-Alfaro et al., 2013; Wrage et al., 2017). (2) The second hydrothermal system group has been described with a neutral to low pH (2-7) and low Cl/B ratios (~1); and unlike LOFS-domain does not show a correlation between trace alkali metals and Cl. This cluster is associated with Andean Transverse Faults (ATF) compound by NW-oriented sinistral-reverse faults (up to 300 km long) (Glodny et al., 2008; Lange et al., 2008; Radic, 2010; Rosenau et al., 2006). This structural context provides a suitable condition for the development of magma reservoirs, which are the source of heat and mass for the geothermal systems (Sánchez-Alfaro et al., 2013). The geochemical evolution of these systems is represented by meteoric water absorption of magmatic gases, interaction with volcanic rocks and dilution (Sánchez-Alfaro et al., 2013; Wrage et al., 2017). Gas samples from fumaroles and thermal springs in domain of ATF show a higher degree of crustal contamination according to $^3He/^4He$,$^{13}C-CO_2$, and ^{15}N (Held et al., 2018; Tardani et al., 2016). These two structural can explain the main structural variables that control the distribution and chemistry of the hydrothermal fluids (Sánchez-Alfaro et al., 2013; Wrage et al., 2017). Despite positive advances in the development of the dynamics of hydrothermal systems, there is still a lack of studies that focus on surface processes and how the chemical composition of hydrothermal waters and volcanic gases can increase the chemical weathering of rocks in groundwater and rivers.

Regarding weathering processes and the geochemical composition of rivers in Chile, Pepin et al., (2010) was the first study to estimate suspended sediment flux out of the Chilean Andes and it is relation with different variables such as climate, topography seismicity, and vegetation; with the aim to quantifying the suspended sediment flux to the Pacific Ocean in eleven rivers ubicated between 38° and 42°S in the Central South Volcanic Zone. In the same line, other studies have focused on decadal and millennial erosion rates in the semi-arid Central Andes (Aguilar et al., 2011; Carretier et al., 2015, 2018; Tolorza et al., 2014). Lee et al. (2013) determined the chemical and physical weathering in south Patagonian Rivers (49°–54° S and 69°–73° W). Using Sr and U isotopes, these authors analyzed the solutes sources (rock types) and the intensity of weathering, concluding a chemical denudation rate of 0.07-5 x 10^5 ton/yr and a CO_2 consumption of 0.03-0.5 x 10^5 mol/km²/yr. Klaes et al. (2022) studied the element mobility related to rock weathering and soil formation in the Patagonian Andes (53°S), being the first paper to evaluate the hyper-humid conditions of the biogeochemical processes. Other authors have addressed anthropogenic impacts on water-quality of rivers from industrial processes (mining, forestry, agriculture). For example, Schuller et al. (2013)

and Bravo-Linares et al. (2020) determined the different sources of sediment by land uses in forested catchments draining towards the Pacific Ocean in the south-central Andes (37°S-40°S). Viers et al. (2019) show the impact of mining, lithology, and physical weathering, characterizing the chemical composition of rivers in the Central and northmost Southern Andes (30°S–38°S). In addition, several studies have focused on studying regolith development in the Coastal Cordillera of Chile between 25°S and 40°S (Krone et al., 2021; Lodes et al., 2023; Oeser et al., 2018; Oeser & von Blanckenburg, 2020; Schaller et al., 2018; Schaller & Ehlers, 2022; Vázquez et al., 2016). These studies have focused on determining the architecture of the weathering zone, and denudation rates from in-situ ^{10}Be data in soil profiles. Nonetheless, these researchers have yet to undertake an investigation into denudation processes within the Andean Cordillera. Consequently, the chemical processes occurring at the surface of rivers and streams remain unexplored. Our research seeks to understand and quantify the natural fluxes of solutes resulting from the erosion of rocks of the southern Andean arc. This region is characterized by a temperate rainy climate, large rivers from the mountains to the ocean, and numerous hot springs, suggesting high rates of rock weathering. This study aims to elucidate the role of hydrothermal systems in the export of solutes by quantifying the chemical weathering fluxes that originate from them to the rivers that drain volcanic basins and thereby add to the global understanding of these processes in continental arcs.

1.3. Hypothesis and Experimental Approach

The Southern Volcanic Zone (SVZ) has significant potential to contribute with substantial chemical weathering fluxes, comparable to other volcanic arcs worldwide, such as Kamchatka, the Antilles (Guadeloupe and Martinique), or New Zealand. The rivers and streams in the Central SVZ (38–42°S) drain primarily on Miocene to recent volcanic rocks and deposits, which are predominantly composed of mafic to intermediate materials, such as basalts to basaltic-andesites. Furthermore, the region features numerous thermal springs, high precipitation rates exceeding 2,500 mm/year, and extensive river systems that discharge into the Pacific Ocean, with average runoff reaching 2,000 mm/year. Streams and rivers in the SVZ are probably influenced by hydrothermal systems, leading to increased solute exports and, thus, chemical weathering fluxes. These hydrothermal inputs can be estimated using chemical tracers, including boron isotopes and germanium, alongside conventional ones, such as chloride (Cl) and carbon isotopes.

1.4. Structure of the thesis

The present thesis is organized into three chapters. The current chapter (Chapter 1) presents a brief theoretical background for readers not familiar with the chemical weathering process and the cycle of CO_2, or the use of certain geochemical tools, such as environmental tracers for thermal impact in surface water. Furthermore, a general overview of the problem, along with the research questions and aims of this study. Chapter 2 constitutes the central part of this dissertation, including the methodologies, results, and discussions. This chapter will constitute a manuscript in preparation to be submitted to Earth and Planetary Science Letters. Chapter 3 provides a summarized review of the scientific contributions of this work and their implications, as well as a discussion on future work that may improve our understanding of seasonal variability in river chemical flows and the hydrothermal influence during the year.

In addition, supplementary material to Chapter 2 has been included. Annex A provides trace elements data of rivers and hot springs during the summer and winter seasons. Furthermore, Annex B contains additional figures related to hot springs for readers who are interested in further exploration of these types of waters. Annex C: Assignation of hot springs in each method to determine the thermal input (Cl-Ge/Si) offer a comprehensive description of the equations, boundary conditions, and necessary assumptions underlying the chemical methods used to estimate the high-temperature solutes fluxes that influence the streams, such as Cl, and Ge/Si. Additionally, Annex D: Calcite precipitation curves includes the PHREEQC code developed for calculating the distribution of ^{13}C isotopes during CO_2 degassing and calcite precipitation.

1.5. Publications and abstracts resulting from this dissertation.

Publications

Peña-Echeverría, A., Pérez-Fodich, A., Daniele, T., Louvat, P. (2023) "Effects of hydrothermal systems on chemical weathering fluxes in volcanic catchments in the Southern Andes". Manuscript in preparation for Earth and Planetary Science Letters. (Chapter 2).

Conference abstracts

Pérez-Fodich, A., Louvat, P., Peña-Echeverría, A., Daniele, T. (2022) "The chemical composition and weathering fluxes of rivers draining volcanoes in the Southern Andes", presented at Goldschmidt, Hawaii, USA, July 2022.

Peña-Echeverría, A., Pérez-Fodich, A. (2022) "Caracterización hidrogeoquímica en el arco volcánico continental en el sur de los Andes, entre los 38° y 42° Sur y su influencia en los procesos globales de meteorización química", presented at the I Graduate Congress, Faculty of Physical Sciences and Mathematics, University of Chile, Chile, August 2022.

Peña-Echeverría, A., Pérez-Fodich, A., Daniele, T., Louvat, P. (2023) "Ge/Si and $\delta^{11}B$ for quantifying hydrothermal inputs in river solute fluxes in active volcanoes in the Southern Andes", presented at Goldschmidt, Lyon, France, July 2023.

Peña-Echeverría, A., Pérez-Fodich, A., Daniele, T., Louvat, P. (2023) "Estimación de la influencia termal en los ríos de las cuencas volcánicas de los Andes del Sur (38° a 42°S)", to be presented at Chilean Geological Congress, Santiago, Chile, November 2023.

Peña-Echeverría, A., Pérez-Fodich, A., Daniele, T., Louvat, P. (2023) "Seasonal variability in solute patterns and implications for rock weathering rates in the active volcanic watersheds of Southern Andes", to be presented at American Geophysical Union (AGU) 2023, San Francisco, USA, December 2023.

Chapter 2: Effects of hydrothermal systems on chemical weathering fluxes in volcanic catchments in the Southern Andes

Amanda Peña Echeverría[a], Daniele Tardani[b], Pascale Louvat[c], Alida Perez-Fodich[a*]

[a] *Department of Geology and Andean Geothermal Center of Excellence (CEGA), University of Chile*
[b] *Instituto de Ciencias de la Tierra, Universidad de O'Higgins*
[c] *Institute of Interdisciplinary Research on Environment and Materials (IPREM), Université de Pau et des Pays de l'Adour*

*Corresponding author aliperez@uchile.cl (A. Perez-Fodich)
Keywords: Southern Andes; Chemical weathering, Hydrothermal systems; Volcanic catchments

ABSTRACT

Rivers draining volcanic regions are key to the global flux of solutes towards the ocean and in the consumption of atmospheric CO_2 through silicate weathering. However, in active volcanic regions degassing and hydrothermal inputs can be an additional supply to weathering fluxes from high-temperature water-gas-silicate reactions. Multiple surface hydrothermal manifestations and substantial degassing characterize continental volcanic arcs. Here we focus on the Southern Andes as one of the most active volcanic provinces with more than 200 hydrothermal manifestations, high precipitation rates >2 m/yr, numerous catchments feeding larger rivers draining toward the Pacific Ocean, frequent eruptions, and preferentially mafic volcanic rocks. We sampled 22 rivers and 16 hot springs at high and low discharges from different volcanic basins in the Southern Andes. The volcanic basins present waters of the calcium/magnesium bicarbonate type and the relationship between the Ca+Mg flux and the cationic Na flux is consistent with silicate weathering of mostly basalt-andesite to andesite rocks. Using hydrothermal tracers Ge/Si and the relation between Cl/B vs $\delta^{11}B$ it is possible to identify 14 of 22 rivers affected by hydrothermal inputs with both tracers agreeing in most cases. Using

X/Cl ratios and Ge/Si such as high-T° weathering tracer, was possible to estimate the dissolved silicate load from hydrothermal activity. In line with the global average of ~40% from other volcanic regions, the Central South Volcanic Zone shows a value of 11% on average. We combine the river solute concentrations and annual discharge to calculate the first assessment of chemical weathering fluxes in the Southern Andes. We calculate silicate weathering export rates of 33 to 386 ton/km²/yr in the studied catchments. Using the silicate export rates, we calculate the total carbon consumption via weathering of the total CSVZ area (78,617 km²). As a result, the total weathering carbon consumption via weathering in the CSVZ is 0.11 x 10^{12} mol/yr, equivalent to 0.0013 PgC/yr, which is around 1% of the global carbon silicate weathering on the continents. The $\delta^{13}C$ analyses show that the contribution of atmospheric CO_2 to the weathering of rocks in the CSVZ is notably lower than that of the total budget. Hence, it underscores the significance of other sources of CO_2, originating from hydrothermal or magmatic processes, in chemical rock weathering of CSVZ. The magmatic fraction of CO_2 resulted in a total flux of 10±4 x 10^9 mol/yr normalized by the watersheds area, equivalent to ~60 to 90% of alkalinity flux in the region. This study shows that a significant part of magmatic carbon is not released as CO_2 to the atmosphere but is captured as alkalinity in continental waters to oceans. At the same time, this study is the first assessment of chemical fluxes in rivers of the Southern Andes and underscores the importance of studying large-scale continental volcanic arcs to improve our understanding of the feedback of silicate weathering in the global carbon cycle.

2.1. Introduction

Over geologic time scales two processes drive atmospheric CO_2, including first degassing from arc volcanism, mid-ocean ridge, and metamorphism, whereas storage of CO_2 is driven by chemical weathering of silicate rocks along with organic carbon burial in sedimentary rocks. These two processes control the long-term ($>10^6$ years) climatic evolution of the Earth due to the greenhouse gas properties of atmospheric CO_2 (Berner et al., 1983; Francois & Walker, 1992; Walker et al., 1981). Thus, estimating global weathering fluxes is key to understanding the long-term evolution of the Earth's climate. The global consumption of acid carbonic estimate results from the weathering of volcanic rocks in soils, shallow groundwater, and rivers. This process occurs as atmospheric CO_2 dissolves in water, forming carbonic acid, or through the action of organic acids derived from organic matter in the soil. The reaction produces clay minerals, dissolved cations, and bicarbonate. Bicarbonate and cations are then transported to

the oceans, where they can precipitate as carbonates. The overall outcome of this weathering process is the removal of carbon dioxide from the ocean-atmosphere system.

In active volcanic regions, a significant portion of stream alkalinity arises from water-rock interactions at higher temperatures during hydrothermal circulation. Deep groundwater in volcanic areas, characterized by its acidic nature due to the presence of magmatic acids, exhibits intense rock weathering, resulting in high chemical loads. When determining atmospheric CO_2 uptake, it is important to exclude the influence of magmatic carbon and consider the contributions of solutes to surface fluxes. Additionally, the high sulfate and chloride content in volcanic thermal waters suggests that not only carbonic acid but also sulfuric and hydrochloric acids serve as proton donors for chemical weathering. In the last twenty years, many authors have focused on river geochemistry to quantify the global silicate weathering flux and associated flux of consumed atmospheric CO_2 (e.g., Dessert et al., 2003; Gaillardet et al., 1999; Gaspard et al., 2021; Louvat & Allegre, 1998; Louvat & Allegre, 1997; Negrel et al., 1993; Rad et al., 2013; Rivé et al., 2013; Schopka et al., 2011,). The weathering of rocks occurs through two processes: the chemical, since the rocks and minerals partially dissolve and transport the products of erosion in soluble form; mechanical, by rock fracturing that provides fine-grained material. Global erosion will depend on a priori on many factors, such as flow (Godsey et al., 2009; Harrison et al., 2005; Hem, 1948, 1985; Johnson et al., 1969), land cover (Mattsson et al., 2005), vegetation (Gíslason et al., 1996; Kardjilov et al., 2006), precipitation (Clair et al., 1999), temperature (Brady, 1991; Velbel, 1993) and winter snowpack (Clair & Ehrman, 1998). However, various authors (e.g., Bluth & Kump, 1994; Dupré et al., 2003; Meybeck, 1987; Desser et al., 2003; Hartmann et al., 2009; Wymore et al., 2017; Horton et al., 1999; Ibarra et al., 2016; Rajamani et al., 2009; Maharana et al., 2018) have shown that rocks with a mafic composition are easily weatherable compared to others, highlighting the importance of the lithological variable in the process. Active volcanic provinces, mainly those rich in mafic rocks, play a prominent role in chemical weathering fluxes (Bluth & Kump, 1994; Dessert et al., 2009; Gaillardet et al., 2011; Gaspard et al., 2021; Hartmann, 2009; Louvat & Allegre, 1997; Rad et al., 2007; Schopka et al., 2011; Schopka & Derry, 2012). The reactive volcanic glass, presence of acid gases, and frequent volcanic eruptions make these regions major contributors to weathering processes, serving as significant sources of rock-derived nutrients transported from streams to oceans. Additionally, the mineralogical composition of volcanic regions promotes the consumption of CO_2 in continental waters, enhancing their impact on biogeochemical cycles. According to Dessert et al. (2003) the chemical weathering rate of basalt rocks is 5-10 times higher than the chemical weathering of granite and

gneiss, and probably is responsible for 30% of the modern-day global flux of acidity consumption (Dessert et al., 2003; Dupré et al., 2003), even though these rocks represent only 5% of the Earth's surface area (Dessert et al., 2003; Hartmann & Moosdorf, 2012). The impact on weathering rates due to basin lithology has been heavily studied on volcanic islands (Dessert et al., 2003; Eiriksdottir et al., 2008; Gislason et al., 1996, 2009; Goldsmith et al., 2008, 2010; Hartmann, 2009; Jones et al., 2011; Louvat et al., 2008; Louvat & Allegre, 1997, 1998; Rad et al., 2006, 2007, 2013; Schopka et al., 2011; Schopka & Derry, 2012) and smaller continental volcanic arc regions (Carey et al., 2015; Dessert et al., 2009; Harmon et al., 2016; Rasmussen et al., 2010), despite the extensions (Andes is one of the longest >7500 km), climate conditions and high volcanic activity (material erupted correspond to 0.6 ± 0.2 km³/year vs 0.3 ± 1.1 km³/year in hot spots; see the summary of previous works in Galetto et al., 2023).

The Southern Volcanic Zone (SVZ) of the Andes has been characterized as one of the most active volcanic zones in the world, located between 33° and 46°S and an extension of 1,400 km. The tectonic setting of the region is characterized by a high rate of magma extrusion and intense eruptive events. Between 1990 and 1999, approximately 1% of the total covert lava was extruded, while from 2000 to 2010 increased to 25% of the volcanic material extruded (Galetto et al., 2023). The central zone (38°S-42°S) is particularly noteworthy, with a magma extrusion rate of 14.9 km³/km/Ma (Jacques et al., 2014; Völker et al., 2011). Additionally, this region hosts more than 200 hydrothermal manifestations (Hauser, 1997), that can play a role in the rates of export solutes from volcanic watersheds. The compositional variability of the hydrothermal springs is explained by different structural domains controlling the permeability of the hydrothermal reservoirs, which allow for varying degrees of interaction between superficial and deep fluids (Sanchez et al., 2013; Roquer et al., 2017; Wrage et al., 2017; Daniele et al., 2020). The volcanic region has been described with a template rainy climate (precipitation rates of >2500 mm/yr) and large rivers from mountain to the Pacific Ocean, suggesting a potential contribution to the global chemical weathering fluxes. Our research provides a deeper insight into understanding the natural solute fluxes resulting from the weathering of Southern Andean arc that affect biogeochemical cycles of rock-derived elements delivered to the ocean.

In this paper, we analyze the chemical weathering of 22 catchments and 16 hot springs located in the Southern Andean Cordillera (38-42°S); and identify the hydrothermal influence using two chemical tracers never before measured in the surface and thermal waters of the area: boron isotope and germanium. We attempt to estimate both fluxes of low-temperature

and high-temperature chemical interaction; adopting two different discriminators to do that: Chloride and Ge/Si ratios. Finally, we provide new data on Southern Rivers in the Chilean Andean arc and highlight the importance of continental volcanic arcs in the chemical weathering processes of the Earth.
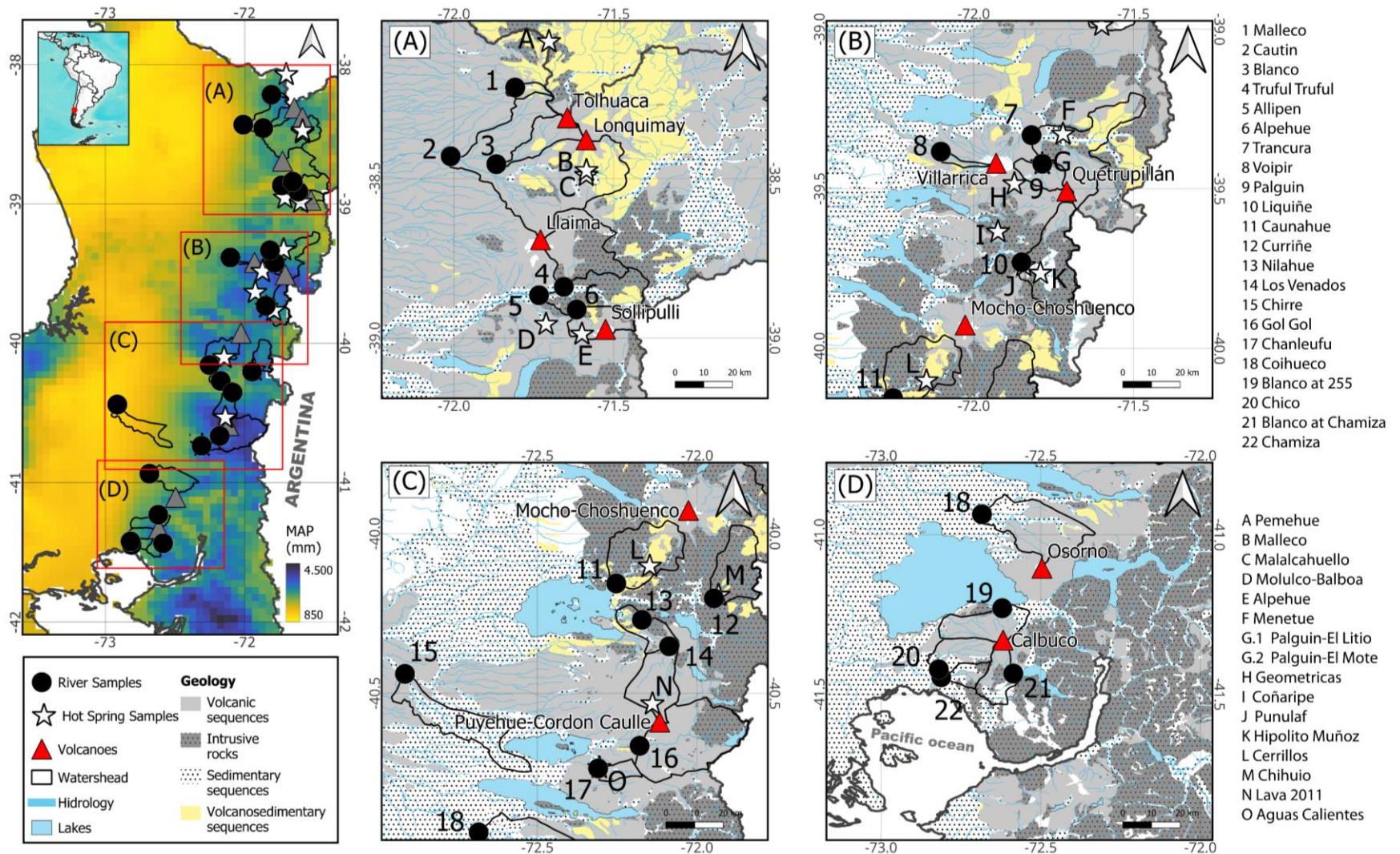
Figure 2: Location and simplified geological setting of the Central South Volcanic Zone (38°S-42°S). The colored map shows the mean accumulated annual precipitation (MAP; 1980-2022) with values >2,000 mm from 400 to 900 m.a.s.l. and close to the ocean (41°S-42°S, 72-73°W). Precipitation data was obtained from CAMELS-CL (Alvarez-Garreton, et al., 2018). The grey triangles correspond to volcanic edifices, the white stars are the locations of the sampled hydrothermal sources, and the black circles are the locations of the gaging stations where the streams were sampled. Catchment areas are shown in all maps in black. The areas marked in red indicate the locations of the four sampling areas to the right in panels A-D. The geologic maps of the four sampling areas show the hydrography in the region and the geologic units mapped at a scale of 1:1,000,000 (SERNAGEOMIN, 1982).

2.2. Geological setting

The Andean Southern Volcanic Zone (SVZ) is a ~1400 km continental volcanic arc on the southwestern margin, stretching from 33°S to 46°S due to the subduction of the Nazca Plate under the South American Plate. It hosts over 60 active stratovolcanoes and 200 surface geothermal features, making it a crucial area for studying volcanic processes (Hauser, 1997; Stern, 2004). The main structural features controlling the location and composition of the hydrothermal manifestations in the Central and Southern SVZ (38°S to 47°S) are the Liquiñe-Ofqui Fault System (LOFS), and the Andean Transverse Fault Zone (ATFs) (Sánchez-Alfaro et al., 2013). The LOFS is a transpressive dextral strike-slip fault, which extends for 1,200 km (38°S to 47°S) (Adriasola et al., 2006; Cembrano et al., 2000, 1996, 1996; Rosenau et al., 2006), whereas the ATFs consists of a series of NW-oriented sinistral-reverse faults (Rosenau et al., 2006; Glodny et al., 2008; Lange et al., 2008; Radic, 2010). In recent years, there have been notable advancements in understanding the formation of the hydrothermal systems in the CSVZ and the controls on the different fluid compositions (Daniele et al., 2020; Held et al., 2018; Pérez-Estay et al., 2022; Pérez-Flores et al., 2016, 2017; Pérez-Moreno et al., 2021; Ray et al., 2009; Risacher et al., 2011; Roquer et al., 2017; Sánchez-Alfaro et al., 2013; Tardani et al., 2016; Wrage et al., 2017). All these authors agree that inherent differences between structural domains are observed in the chemical and isotopic composition of associated geothermal fluids, being evident in conservative element ratios such as Cl/B (Wrage et al., 2017), and the isotopic signature of specific volatile components (Ray et al., 2009; Sánchez-Alfaro et al., 2013; Tardani et al., 2016). These authors recognize two types of hydrothermal manifestations with contrasting chemical compositions: the first group corresponds to neutral to alkaline pH waters (7-10), with high Cl/B ratios (~50) and strong correlation between Li, Cs, Rb and Cl. This cluster is associated with NNE-striking structures of the LOFS. The predominant mechanism of heat transfer in these systems is thermal conduction from crystalline host rock, and the chemical composition of discharging springs is a product of heat-fluid-rock interaction at depth of infiltrating meteoric fluids due to increased vertical permeability of the basement (Sánchez-Alfaro et al., 2013; Wrage et al., 2017). Some hydrothermal manifestations have primitive signatures associated with shallow volcanic/geothermal environment (^{3}He/^{4}He, ^{13}C-CO_2 and ^{15}N), while the rest show higher crustal contamination (Tardani et al., 2016). The second hydrothermal system group corresponds to fluids with neutral to acid pH (2-7), low Cl/B ratios (~1), and unlike those springs on the LOFS-domain, there is little correlation

between trace alkali metals and Cl. This cluster is spatially correlated to the Andean Transverse Faults (ATF), which is associated with the emplacement of magma reservoirs that are the heat sources for the geothermal systems (Sánchez-Alfaro et al., 2013). The geochemical evolution of these systems is represented by a greater degree of interaction with magmatic chambers through degassing, as these fluids experiment absorption of magmatic gases, interaction with volcanic rocks and dilution with meteoric gases (Sánchez-Alfaro et al., 2013; Wrage et al., 2017). The gas isotopes show a higher degree of crustal contamination for those systems associated to LOFS (using ^{3}He/^{4}He,^{13}C-CO$_2$,^{15}N isotopes; Tardani et al., 2016; Held et al., 2018). These two domains have contributed to explaining the main structural variables that control the location of hydrothermal fluids and their relationship with the volcanic-magmatic context of the region.

The geological setting in this study corresponds to the SVZ segment between 38°S and 42°S. To the north of 39° S, the main lithologies correspond to the members of the Cura-Mallín Group (re-defined as such by Pedroza et al. (2017)). This group is composed by volcanic and volcano-sedimentary sequences deposited during the Oligocene-Miocene (Charrier et al., 2007). The Cura-Mallín Group overlays the basement of the current volcanic arc, which is composed by Meso-Cenozoic rocks from the Patagonian Batholith of Late Jurassic and Pleistocene ages (Pankhurst et al., 1999). This plutonic complex extends from 39°S to 47°S and consists of heterogeneously deformed granodioritic to tonalitic rocks (Hervé et al., 1993; Parada et al., 2001). Older rocks from both the Liquiñe Metamorphic Complex (Paleozoic-Triassic) and the Futrono-Riñihue Batholith (Carboniferous-Permian) have been identified in the region. The Liquiñe Metamorphic Complex is composed of limited outcrops of pelitic schists, schists, and amphibolites, and to a lesser extent, ultramafic metamorphic rocks between 38°S and 42°S (Lara et al., 2004). The Futrono-Riñihue Batholith is composed of restricted outcrops of granites, granodiorites, tonalites, and diorites from 40°S onwards. The Quaternary volcanoes have erupted varying volcanic products that have been deposited overlaying the basement rocks and those from the Cura-Mallín Group (Figure 2). The main compositions of lava flows, pyroclastic deposits, and tephra layers ranges from basalt (SiO2 ≤ 52%) to basaltic-andesite (SiO2 = 52-56%) (Hickey-Vargas et al., 2016; Lara et al., 2006). However, some stratovolcanoes at the post caldera stage also have deposits of dacitic to rhyolitic compositions (e.g., Quetrupillán, Lanín and Cordón-Caulle(Cembrano & Lara, 2009; Gerlach et al., 1988; Hickey et al., 1984; Lara et al., 2006; López-Escobar, 1984, 1985; Singer et al., 2008)). López-Escobar (1984) described that basaltic rocks from this province show a high content of Al$_2$O$_3$ (>17 wt. %), high CaO (>8 wt.%), low TiO$_2$ (>1.5 wt. %) and relatively

low Mg/(Mg+Fe$_{total}$) ratios (generally >0.6). At the same time, the predominant mafic minerals in this region are olivine, clinopyroxene and orthopyroxene with Fe-olivine; hornblende is sometime present, the hydrous phenocryst phases are absent and secondary quartz is quite common, the plagioclase (An$_{30}$-An$_{50}$, labradorite mainly) is the most abundant phenocryst and groundmass phase (Ewart, 1976; López-Escobar et al., 1977,1984). These volcanic materials have been erupted from stratovolcanoes and monogenetic cones of Pliocene-Pleistocene and Pleistocene-Holocene ages (López-Escobar, 1984) and exhibit primitive magmatic signatures. The magma extrusion rate in the CSVZ is the highest in the Southern Andes (14.9 km^3/km/Ma) (Völker et al., 2011; Jacques et al., 2014). Galetto et al. (2023) indicates that Southern Andes volcanic arc is the most productive arc, follow by Kamchatka arc, in the four analyzed decades (1980-2019), producing respectively 17.8% and 17.7% of the total subaerial mass erupted from continental arcs, which is similar to the eruption rates to hotspot volcanoes like Hawaii and Iceland.

2.3. Climate and Hydrology

Climate between 38°–40.5°S is classified as temperate rainy with a Mediterranean influence, the mean annual precipitation (MAP) ranges from 2,800 to 4,200 mm (Figure 2), with monthly averages ranging from 80 to 590 mm through the year (database of CAMELS-CL explorer; Alvarez-Garreton et al., 2018). Mean annual temperature (MAT) ranges between 9 and 11.5 °C, with an average between 5.5 and 9°C in winter and between 12.5 and 14°C in summer. Between 40.5S°–42°S the dominant climate is of temperate oceanic rainy type, with two different rainfall regimes depending on the distance from the Pacific Ocean and altitudes. Coastal regions and up to 600 m.a.s.l., MAT is 11 °C, and MAP ranges from 1,800–3,600 mm (Alvarez-Garreton et al., 2018). In altitudes above 600 m.a.s.l., cold mountainous conditions prevail, with MAP ranging between 3,200 mm and 4,200 mm (Alvarez-Garreton et al., 2018), and mean annual temperatures between 6 to 9 °C. Precipitation is largely influenced by topography and increases with latitude (Figure 2). Stream discharge is controlled by rainfall during April and August, with most of them showing increase in discharge from September to December due to the snowmelt, except for those located at lower altitudes (<238 m.a.s.l.; rivers 15, 22, 20, 18, and 21 in Figure 2). The dry season lasts between December and March when rivers are fed by baseflow and few stormflows resulting from discrete summer rainfall events. Mean annual runoff rates in the studied watersheds range between 1,080 and 3,100 mm/yr and increase with latitude (Alvarez-Garreton et al., 2018)(Boisier et al., 2016, 2018;

Garreaud et al., 2017; González et al., 2018). These watersheds are characterized by minimal human intervention (with <3% of the drainage area destined to croplands and conifer plantations; see in Alvarez-Garreton et al., 2018). Land use from 38°–40°S has >48% native forest and ~28% shrub and grass cover. Land use between 40°–42°S an average of 61% native forest cover followed by ~26% shrub and grass cover.

The Andes in central-southern Chile have experimented a drying trend in the last ~60 years that has impacted precipitation and streamflow in watersheds draining towards the Pacific between 38°S-48°S (Boisier et al., 2016, 2018). However, a more acute drought has affected the region in the last 13 years. The drought has caused annual rainfall deficits ranging from 15 to 45% (Boisier et al., 2016, 2018; Garreaud et al., 2017; González et al., 2018). The stations reported in the work show negative trends per decade in both variables, with -5±2.6% decade[-1] in precipitations and -3.4±0.8% decade[-1] in streamflow.

2.4. Methods

2.4.1. Fieldwork and sampling

We sampled 22 watersheds located on igneous rock substrates between 38° and 42°S in the Southern Andes during both the dry and wet seasons in the Austral summer and winter respectively (February and July 2021). This selection was based on the local geology (volcanic or intrusive rocks) and the low anthropic impact, with large coverage of native forest (>50%). We also sampled 16 thermal springs based on their temperature and proximity to volcanic centers following previous surveys (e.g., Risacher et al., 2011; Wrage et al., 2017). Most thermal spring samples were collected during the summer of 2021 and 2022 (February), and only a 4 of them were collected during winter in 2022. Upon sampling, we measured in-situ water temperature (°C), conductivity (µS/cm), pH, OD (% and mg/l), total dissolved solids (TDS, mg/l), redox potential (ORP, mV) with a YSI Pro Quatro multi-parameter probe. All the samples were collected into high-density polyethylene bottles (except those for $\delta^{13}C$ and DIC, which were collected in Exetainer® glass vials), and sampled in the field trough 0.22 µm syringe filters of cellulose acetate (CA) or polyethersulfone (PS) membrane. Sample aliquots for cations, trace elements, silica and boron isotopes were acidified with Surprapur® 4N HNO₃

down to pH < 2 with a dilution factor ~1%. The carbon isotope vials were protected from light upon collection.

2.4.2. Laboratory analyses

The major and trace elements were analyzed in the Fluid Geochemistry Laboratory of the Andean Geothermal Center of Excellence (CEGA). The carbonate and bicarbonate concentrations in water were analyzed using the Giggenbach method in a Hanna HI-902C automatic titrator with a combined glass electrode upon return from the field. Anion (Cl, F, Br, NO_3, SO_4, P) concentrations were determined with a Thermo Scientific Dionex ICS-2100 ion chromatograph with Dionex IonPac™ AS11-HC RFIC™ analytical 4 x 250 mm column, Dionex IonPac™ AG11-HC RFIC™ 4 x 50 mm pre-column. Major cations (Ca, Mg, Na, K) and silica were analyzed by atomic absorption spectrometry (AAS) with a Perkin Elmer PinAAcle 900F, with a standard nebulizer. Trace elements concentrations were analyzed via mass-spectrometry using a single quad inductively coupled plasma source mass spectrometer (Thermo Scientific ICP-MS Q iCAP-Q). Isotopes of boron were analyzed in the Geochemical Laboratory of External Envelopes of the Institute of Physics of the Globe of Paris (IPGP) by MC-ICP-MS with a direct injection nebulizer (d-DIHEN), after boron extraction through ion chromatography, with a 2SD reproducibility between 0.1 and 2.5‰ (generally higher for thermal springs). $^{11}B/^{10}B$ ratios are expressed relative to the boric acid standard NBS 951 (NIST): $\delta^{11}B = \{(^{11}B/^{10}B) \text{ sample } / (^{11}B/^{10}B) \text{ NBS951} - 1\} \times 1000$. The carbon isotopes of DIC were measured using analytical method development by Assayag et al. (2006) The ^{13}C isotopes were measured in a gas chromatograph coupled to an isotope ratio mass spectrometer (GCIRMS – Finnigan delta XP) in the laboratory of the Institute of Physics of the Globe of Paris (IPGP). The germanium concentrations were analyzed using hydride-generation ICP mass-spectrometry (HG-ICP-MS) (Aguirre et al., 2017; Mortlock & Froelich, 1996) at Cornell University and the trace IPGP with a Teledyne Cetac HGX-200 hydride generation system and a Thermo Element 2 ICP-MS. The quantification was by isotope dilution using the $^{70}Ge/^{74}Ge$ ratio with corrections for mass bias and signal drift from sample-standard bracketing.

2.4.3. Monthly and annual discharge in gaged and ungagged streams

The discharge datasets considered in this study were compiled by the method of area transposition. The method uses the similarity principles between catchments for the estimation of flows in ungagged streams or gagged streams with incomplete registers (e.g., Hrachowitz et al., 2013; Oudin et al., 2008, 2010; Parajka et al., 2013). This method provides an estimation of mean annual discharge by building linear regression models with neighboring stations that present a similar runoff regime. The work of Quevedo (2021), focused on Andean catchments in Chile, improves the modeled datasets by incorporating additional physical variables to match up watersheds (area, slope, soil type, MAT, aridity index, others). The model decreases the uncertainties on discharge estimation and temporal resolution in uncontrolled basins. The method starts by selecting the watersheds that meet the "natural regime" criteria, known as a "basin donor" (Mendoza et al., 2021), these criteria are: (1) a human intervention index (according to CAMELS-CL; see in Alvarez-Garreton et al., 2018) less than 0.05; (2) absence of water reservoirs such as dams or lakes; and (3) that the station associated with the basin is not intervened by water extraction. In our study, 13 of the 22 rivers are gaged, but only four meeting the natural regime criteria (Station ID's: 10102001, 10305001, 10322003, and 10432003). The rest of the basin donors were 8351001, 9123001, 9122002, 9404001, 9416001, 10327001, 103430002 (ID station code). The incomplete records are filled with a local lineal regression considering others nearby stations (<200 km). Once the historical data (1980-2022) of the selected natural regime basins has been filled in, the basin with the greatest similarity is chosen (Wegener et al., 2007) to estimate the monthly discharge and rainfall in the rest of the ungagged streams or streams with poor record. We use the modeled monthly discharge data for each year (n=42) to determine a monthly discharge, an annual mean discharge, and subsequently an historical annual discharge with standard deviations of 18-28% of the mean values (Table 1) between 1980-2022. If we compare the value obtained by averaging the raw data from 7 stations and the modeled discharge data between 1980 and 2022, the difference ranges between 1% and 55%, with an average of 17%. Although the model in some gauges does not show the best fit (>20% difference with respect to the real values), the method allows us to preliminarily determine the chemical fluxes for all rivers, especially in ungauged streams (see in Annex E: Monthly and annual discharge in gaged and ungagged streams). The area of the basin used for runoff was delimited using a digital elevation model (DEM) in ArcGis and the exit point of basins corresponds to the sampling site in each of them; being Voipir River the smallest watershed (39 km²) and Cautin River the largest (1,595 km²).

Table 1: Physicochemical parameters (T° in situ, EC, TDS, and pH), major cations and silica concentrations (Na, K, Ca, Mg, and SiO_2) for hydrothermal sources, and rivers during summer and winter seasons in the study area. Mean annual discharge and mean accumulated-annual precipitation (MAP) was determined with a modeled historical record of 42 years (1980-2022) of fluviometric-meteorological stations (General Direction of Water, Chile) (see section Methods). Donor Basin ID corresponds to gagged (with natural regimen) used for estimating the monthly discharge data.

Sample ID	ID	Name	Type	Season	Year	Donor Basin ID	Mean annual discharge	MAP	Area	Lon	Lat	T° in situ	EC	TDS	pH	Na	K	Ca	Mg	SiO₂
							m³/s	mm/yr	km²			°C	µS/cm	mg/L		µmol/L	µmol/L	µmol/L	µmol/L	µmol/L
SVZ030	1	Malleco	River	Summer	2021	8351001	2.7±0.8	3572	58	-71.81	-38.22	14.5	39.2	31.8	7.4	134.5	11.3	96.6	36.2	250.0
SVZ029	2	Cautin	River	Summer	2021	9123001	80.8±18.6	3159	1595	-72.01	-38.43	14.4	82.1	66.9	8.1	243.7	30.0	168.2	101.2	458.3
SVZ031	3	Blanco at Curacautin	River	Summer	2021	9122002	6.9±1.7	3590	202	-71.87	-38.46	19.8	73.7	52.4	8.2	193.0	27.9	138.5	79.8	388.3
SVZ000	4	Truful-Trulf	River	Summer	2021	9404001	27.5±6.2	3069	476	-71.66	-38.84	10.3	67.4	60.8	7.9	316.6	25.1	140.0	84.3	443.3
SVZ033	5	Allipen	River	Summer	2021	9404001	34.2±7.7	2829	593	-71.73	-38.87	11.5	69.0	60.5	7.7	260.3	23.6	126.3	97.9	355.0
SVZ034	6	Alpehue	River	Summer	2021	9404001	11.8±2.7	2919	205	-71.62	-38.91	9.7	41.8	38.0	7.7	186.9	17.7	61.1	93.0	213.3
SVZ028	7	Trancura	River	Summer	2021	10102001	46.4±9.6	4179	564	-71.82	-39.33	14.7	81.2	65.7	7.2	269.0	36.4	169.7	95.5	371.7
SVZ026	8	Voipir	River	Summer	2021	10102001	3.2±0.7	3220	39	-72.10	-39.38	14.7	44.4	35.9	7.2	134.9	17.9	98.3	60.5	341.7
SVZ027	9	Palguin	River	Summer	2021	10102001	10.8±2.2	3794	131	-71.78	-39.42	9.7	58.8	55.0	7.5	227.1	35.4	120.3	76.5	468.3
SVZ019	10	Liquiñe	River	Summer	2021	10102001	36.8±7.6	3511	449	-71.85	-39.73	15.3	69.5	55.5	8.2	231.0	23.1	142.2	61.7	270.0
SVZ017	11	Caunahue	River	Summer	2021	10305001	35.3±9.0	3282	457	-72.25	-40.16	15.4	72.2	57.4	8.4	133.6	14.4	247.0	53.1	210.0
SVZ018	12	Curriñe	River	Summer	2021	10305001	25.6±6.5	3474	331	-71.95	-40.20	13.8	75.8	62.4	7.7	186.0	13.6	237.8	49.4	253.3
SVZ015	13	Nilahue	River	Summer	2021	10322003	39.1±7.2	3733	477	-72.17	-40.27	20.7	465.8	329.6	8.7	2238.0	175.6	635.8	466.2	918.3
SVZ016	14	Los Venados	River	Summer	2021	10322003	24.4±4.5	3331	297	-72.09	-40.35	14.2	89.8	73.6	8.1	469.4	28.5	172.4	81.9	501.7
SVZ006	15	Chirre	River	Summer	2021	10327001	20.1±4.5	4237	444	-72.91	-40.44	15.5	74.6	58.9	8.3	252.4	37.2	136.5	105.3	435.0
SVZ010	16	Gol-Gol	River	Summer	2021	10327001	58.4±10.8	3686	714	-72.18	-40.66	11.9	69.4	60.1	7.7	243.7	31.0	136.7	96.7	428.3
SVZ008	17	Chanleufu	River	Summer	2021	10327001	6.0±1.1	1898	73	-72.31	-40.74	10.8	58.2	51.9	7.6	213.1	15.9	164.9	55.5	273.3
SVZ005	18	Coihueco	River	Summer	2021	10343002	23.3±4.3	2887	484	-72.68	-40.94	12.2	74.0	63.4	7.6	191.3	22.3	153.9	116.0	425.0
SVZ004	19	Blanco at R-225	River	Summer	2021	10432003	18.3±3.3	3248	268	-72.62	-41.23	11.6	45.7	39.6	7.3	140.2	17.4	115.5	52.3	375.0
SVZ003	20	Chico	River	Summer	2021	10432003	13.6±2.4	3644	199	-72.82	-41.42	17.0	95.7	73.5	8.0	326.6	30.8	178.4	136.2	420.0
SVZ001	21	Blanco at Chamiza	River	Summer	2021	10432003	12.5±2.2	2990	183	-72.59	-41.43	11.3	51.0	44.5	7.7	152.8	12.8	123.0	51.8	306.7
SVZ002	22	Chamiza	River	Summer	2021	10432003	6.2±1.1	3243	91	-72.81	-41.45	13.6	81.1	67.4	7.7	277.3	24.6	170.9	107.0	416.7
SVZ115	A	Pemehue	Hot spring	Winter	2022	-	-	-	-	-71.70	-38.07	34.3	6403.0	3201.0	7.8	30567.7	888.5	3642.9	16.5	1494.5
SVZ024	B	Malleco	Hot spring	Summer	2021	-	-	-	-	-71.58	-38.48	92.0	1082.0	519.0	8.1	5209.6	129.7	190.9	4.5	2493.3
SVZ023	C	Malalcahuello	Hot spring	Summer	2021	-	-	-	-	-71.59	-38.49	42.3	409.1	205.9	9.2	2052.4	35.9	89.6	<0.4	778.3
SVZ117	D	Molulco-Balboa	Hot spring	Winter	2022	-	-	-	-	-71.71	-38.96	66.0	1574.0	786.0	6.9	7205.2	351.8	361.5	93.8	2459.3

Table 1: Continued

Sample ID	ID	Name	Type	Season	Year	Lon	Lat	T° in situ	EC	TDS	pH	Na	K	Ca	Mg	SiO$_2$
								°C	µS/cm	mg/L		µmol/L	µmol/L	µmol/L	µmol/L	µmol/L
SVZ045	E	Alpehue	Hot spring	Summer	2021	-71.60	-38.98	95.4	1469.0	816.0	8.9	15807.9	516.9	213.8	<0.4	6115.0
SVZ021	F	Menetue	Hot spring	Summer	2021	-71.72	-39.33	49.0	801.0	356.1	9.1	3427.9	40.8	69.9	1.6	1346.7
SVZ014	G.1	Palguin Alto	Hot spring	Summer	2021	-71.78	-39.42	52.0	669.0	302.8	8.5	2762.0	52.6	133.2	22.6	1048.3
SVZ020	G.2	Palguin Alto	Hot spring	Summer	2021	-71.78	-39.42	44.0	458.0	233.0	8.2	2087.3	71.8	99.6	51.4	1008.3
SVZ022	H	Geometricas	Hot spring	Summer	2021	-71.87	-39.48	86.5	1950.0	857.0	8.0	6244.5	146.4	1177.0	4.9	1491.7
SVZ013	I	Coñaripe	Hot spring	Summer	2021	-71.92	-39.64	70.0	1190.0	527.0	8.1	5371.2	105.6	155.7	15.6	1540.0
SVZ012	J	Punulaf	Hot spring	Summer	2021	-71.84	-39.74	57.9	632.0	286.2	8.8	2914.8	64.4	96.3	3.3	1666.7
SVZ011	K	Hipolito Muñoz	Hot spring	Summer	2021	-71.79	-39.77	78.0	763.0	346.7	8.9	3646.3	65.9	64.9	0.8	1508.3
SVZ009	L	Cerrillos	Hot spring	Summer	2021	-72.15	-40.10	39.0	487.0	249.2	8.8	2323.1	27.4	240.8	9.5	993.3
SVZ133	M	Chiuio	Hot spring	Winter	2022	-72.01	-40.12	82.0	889.0	443.0	9.2	4257.6	102.8	239.8	1.2	1974.0
SVZ083	N	Lava 2011	Hot spring	Summer	2022	-72.14	-40.51	35.6	1915.0	960.0	7.5	6200.9	450.8	2004.3	558.0	511.7

ID	No.	Name	Type	Season	Year											
SVZ068	O	Aguas Calientes	Hot spring	Winter	2022	-72.31	-40.73	66.5	1366.6	671.0	7.7	7117.9	214.6	473.6	34.6	15208.3
SVZ047	1	Malleco	River	Winter	2021	-71.81	-38.22	4.0	26.9	17.5	7.1	83.0	4.1	68.4	22.6	71.7
SVZ048	2	Cautin	River	Winter	2021	-72.01	-38.43	5.1	37.3	39.1	8.9	170.3	19.0	145.5	71.2	330.0
SVZ046	3	Blanco at Cura-cautin	River	Winter	2021	-71.87	-38.46	4.0	25.7	27.8	7.5	122.3	15.4	96.8	53.1	261.7
SVZ050	4	Truful-Trulf	River	Winter	2021	-71.66	-38.84	8.1	51.8	49.7	8.4	272.9	23.3	154.7	80.2	380.0
SVZ049	5	Allipen	River	Winter	2021	-71.73	-38.87	6.7	54.4	54.4	8.2	262.0	23.6	174.2	108.6	376.7
SVZ052	6	Alpehue	River	Winter	2021	-71.62	-38.91	3.1	41.9	46.9	7.9	242.4	21.8	136.0	113.1	336.7
SVZ057	7	Trancura	River	Winter	2021	-71.82	-39.33	4.6	57.0	29.0	7.5	149.3	21.3	133.7	67.5	316.7
SVZ051	8	Voipir	River	Winter	2021	-72.10	-39.38	6.7	57.0	28.0	7.4	165.9	22.6	123.3	74.9	420.0
SVZ056	9	Palguin	River	Winter	2021	-71.78	-39.42	4.2	35.4	38.8	7.5	171.2	23.6	123.5	70.4	385.0
SVZ053	10	Liquiñe	River	Winter	2021	-71.85	-39.73	7.7	36.5	30.0	7.3	128.8	12.6	128.7	40.7	210.0
SVZ063	11	Caunahue	River	Winter	2021	-72.25	-40.16	7.1	38.6	38.1	7.2	91.3	8.7	185.1	38.7	186.7
SVZ060	12	Curriñe	River	Winter	2021	-71.95	-40.20	6.0	40.9	41.9	7.4	139.3	12.6	189.6	46.1	323.3

| SVZ061 | 13 | Nilahue | River | Winter | 2021 | -72.17 | -40.27 | 9.8 | 222.1 | 203.4 | 8.0 | 1235.8 | 97.2 | 454.1 | 290.9 | 603.3 |
| SVZ055 | 14 | Los Venados | River | Winter | 2021 | -72.09 | -40.35 | 6.1 | 50.4 | 51.5 | 7.2 | 286.0 | 21.3 | 165.7 | 76.9 | 430.0 |

Table 1: Continued

Sample ID	ID	Name	Type	Season	Year	Lon	Lat	T° in situ	EC	TDS	pH	Na	K	Ca	Mg	SiO$_2$
								°C	µS/cm	mg/L		µmol/L	µmol/L	µmol/L	µmol/L	µmol/L
SVZ064	15	Chirre	River	Winter	2021	-72.91	-40.44	6.1	31.9	32.5	7.5	148.9	22.1	86.3	57.6	293.3
SVZ058	16	Gol-Gol	River	Winter	2021	-72.18	-40.66	4.6	30.3	32.3	7.4	112.7	12.1	129.0	41.6	270.0
SVZ062	17	Chanleufu	River	Winter	2021	-72.31	-40.74	5.3	32.3	33.7	7.0	132.8	10.5	122.8	42.4	196.7
SVZ065	18	Coihueco	River	Winter	2021	-72.68	-40.94	8.0	32.4	31.2	7.0	114.4	13.3	105.5	61.3	300.0
SVZ066	19	Blanco at R-225	River	Winter	2021	-72.62	-41.23	7.4	28.4	27.8	7.3	95.6	9.5	87.3	32.5	263.3
SVZ067	20	Chico	River	Winter	2021	-72.82	-41.42	8.3	26.3	25.1	7.5	97.8	6.7	58.6	32.5	165.0
SVZ069	21	Blanco at Chamiza	River	Winter	2021	-72.59	-41.43	6.5	26.3	26.4	7.0	108.7	9.0	97.3	35.8	260.0
SVZ070	22	Chamiza	River	Winter	2021	-72.81	-41.45	8.1	34.6	33.2	7.3	130.6	9.5	81.3	40.7	210.0

Table 2: Anion concentrations in µmol/L. Li, B, Fe and Al in ppb and Ge concentrations in ppt, Ge/Si ratios (µmol/mol), δ^{13}C and δ^{11}B in ‰ (n.d.= below detection limit, "-" = was no measured).

SampleID	ID	Name	Type	Season	Cl	SO$_4$	HCO$_3$	CO$_3$	Li	B	Al	Fe	Ge	Ge/Si	δ^{11}B	δ^{13}C	DIC
					µmol/L	µmol/L	µmol/L	µmol/L	ppb	ppb	ppb	ppb	ppt	µmol/mol	‰	‰	µmol/L/

ID	No.	Name	Type	Season													
SVZ030	1	Malleco	River	Summer	26.3	27.0	327.8	n.d.	1.1	227.9	6.3	16.2	30.7	1.7	7.5	-9.1	432
SVZ029	2	Cautin	River	Summer	48.9	54.9	655.6	n.d.	3.8	39.7	6.5	26.8	20.6	0.6	5.6	-7.6	630
SVZ031	3	Blanco at Cura-cautin	River	Summer	23.2	37.2	491.7	n.d.	1.7	52.1	11.1	59.3	26.5	0.9	6.8	-7.7	790
SVZ000	4	Truful-Trulf	River	Summer	49.4	62.8	524.4	n.d.	2.2	16.6	7.7	3.7	25.4	0.8	5.4	-9.3	546
SVZ033	5	Allipen	River	Summer	51.4	43.4	590.0	n.d.	5.0	32.4	17.3	14.3	60.6	2.4	-1.3	-7.1	870
SVZ034	6	Alpehue	River	Summer	47.2	20.2	409.7	n.d.	4.7	28.7	22.8	8.6	0.0	-	-1.3	-1.4	700
SVZ028	7	Trancura	River	Summer	56.8	55.2	606.4	n.d.	3.9	24.5	7.8	115.1	42.1	1.6	2.5	-8.4	890
SVZ026	8	Voipir	River	Summer	15.3	7.9	409.7	n.d.	0.7	6.6	60.0	15.9	22.6	0.9	6.6	-11.7	516
SVZ027	9	Palguin	River	Summer	36.4	54.0	508.1	n.d.	2.6	21.0	4.7	3.3	36.7	1.1	2.6	-8.3	810
SVZ019	10	Liquiñe	River	Summer	44.4	97.4	426.1	n.d.	3.7	40.0	14.6	11.8	86.9	4.4	2.8	-4.8	569
SVZ017	11	Caunahue	River	Summer	33.6	60.2	573.6	n.d.	0.5	19.3	6.8	19.0	12.4	0.8	7.1	-6.9	683
SVZ018	12	Curriñe	River	Summer	24.3	102.8	557.2	n.d.	1.0	4.4	7.0	7.4	42.0	2.3	9.3	-7.3	850
SVZ015	13	Nilahue	River	Summer	2089.3	170.8	2212.5	n.d.	26.5	897.4	3.0	10.6	248.0	3.7	5.8	-4.5	1939
SVZ016	14	Los Venados	River	Summer	31.4	31.5	917.8	n.d.	1.8	55.5	5.9	31.4	25.9	0.7	4.3	-7.1	1180

Table 2: Continued

Sample ID	ID	Name	Type	Season	Cl	SO₄	HCO₃	CO₃	Li	B	Al	Fe	Ge	δ¹¹B	Ge/Si	δ¹³C	DIC
					μmol/L	μmol/L	μmol/L	μmol/L	ppb	ppb	ppb	ppb	ppt	‰	μmol/mol	‰	μmol/L
SVZ006	15	Chirre	River	Summer	55.4	9.4	671.9	n.d.	0.8	10.9	16.2	127.9	13.0	12.2	0.4	-9.1	791
SVZ010	16	Gol-Gol	River	Summer	107.1	46.8	524.4	n.d.	1.4	14.3	5.8	70.4	24.3	5.3	0.8	-7.6	770
SVZ008	17	Chanleufu	River	Summer	86.4	52.1	426.1	n.d.	5.0	26.7	3.3	7.3	30.8	5.4	1.6	-9.2	722
SVZ005	18	Coihueco	River	Summer	48.6	23.0	622.8	n.d.	0.5	9.2	5.2	37.0	14.8	10.5	0.5	-11.4	900
SVZ004	19	Blanco at R-225	River	Summer	42.1	12.0	426.1	n.d.	1.5	6.4	7.3	18.9	12.8	7.6	0.5	-8.1	578
SVZ003	20	Chico	River	Summer	75.7	4.9	803.1	n.d.	0.9	12.2	19.5	231.4	12.8	9.3	0.4	-11.7	1040
SVZ001	21	Blanco at Chamiza	River	Summer	75.1	36.3	163.9	n.d.	0.7	12.3	5.4	178.5	13.1	12.2	0.6	-7.0	451
SVZ002	22	Chamiza	River	Summer	109.0	17.3	671.9	n.d.	1.6	22.3	7.1	393.7	14.8	9.2	0.5	-12.1	799
SVZ115	A	Pemehue	Hot spring	Winter	36363.0	2156.7	360.7	n.d.	1.2	21221.5	61.6	51.00	6595.7	10.2	60.7	-	-
SVZ024	B	Malleco	Hot spring	Summer	1069.5	1021.8	2802.5	n.d.	738.5	69692.2	408.3	3.85	20689.3	3.7	114.2	-9.6	1887
SVZ023	C	Malalcahuello	Hot spring	Summer	385.9	470.3	360.6	50.00	50.0	350.2	9.5	0.24	4854.3	-0.7	85.8	-14.4	810
SVZ117	D	Moluco-Balboa	Hot spring	Winter	6514.7	398.5	2000.0	n.d.	3.4	2089.5	19.4	< 15	12847.5	0.5	71.9	-	-
SVZ045	E	Alpehue	Hot spring	Summer	10725.4	878.2	1671.7	216.70	1384.8	13266.2	115.6	0.28	61090.7	-2.9	137.5	-6.2	1663
SVZ021	F	Menetue	Hot spring	Summer	863.3	747.9	491.7	33.30	142.0	436.7	36.2	2.72	6419.2	1.7	65.6	-13.6	821
SVZ014	G.1	Palguin Alto	Hot spring	Summer	537.9	781.6	737.5	83.30	90.8	647.7	33.9	1.22	4188.7	2.9	55.0	-13.6	929
SVZ020	G.2	Palguin Alto	Hot spring	Summer	354.8	392.2	1573.3	n.d.	28.9	438.6	87.7	7.37	2360.5	4.3	32.2	-15.8	1458
SVZ022	H	Geometricas	Hot spring	Summer	1271.8	3778.4	442.5	n.d.	241.8	2842.6	12.7	0.13	12635.3	2.6	116.6	-12.4	609
SVZ013	I	Coñaripe	Hot spring	Summer	2226.6	1025.4	1409.4	33.30	190.6	3818.7	81.3	0.40	9027.4	0.1	80.7	-10.8	1630
SVZ012	J	Punulaf	Hot spring	Summer	462.1	866.8	803.1	n.d.	76.1	198.5	34.9	2.02	3367.6	4.5	27.8	-14.2	950
SVZ011	K	Hipolito Muñoz	Hot spring	Summer	921.5	637.0	1294.7	n.d.	145.8	429.5	83.4	1.71	9132.2	1.4	83.3	-7.8	1190
SVZ009	L	Cerrillos	Hot spring	Summer	629.9	805.6	442.5	n.d.	23.7	331.6	3.3	0.19	2761.1	5.5	38.3	-	-
SVZ133	M	Chiuio	Hot spring	Winter	377.1	2049.7	426.2	n.d.	27.8	42.7	19.9	< 3	2646.2	6.6	18.5	-	-
SVZ083	N	Lava 2011	Hot spring	Summer	5565.5	471.8	4344.3	n.d.	43.9	2564.8	24.2	< 15	75.5	5.7	2.0	-	-
SVZ068	O	Aguas Calientes	Hot spring	Winter	5531.4	1240.8	49.2	n.d.	486.5	2393.1	14.6	3.00	5310.9	3.7	4.8	-	-
SVZ047	1	Malleco	River	Winter	10.5	8.2	163.9	n.d.	1.07	105.3	7.0	3	-	6.62	-	-	-
SVZ048	2	Cautin	River	Winter	22.6	30.9	459.0	n.d.	2.28	31.4	6.9	18	-	6.35	-	-	-
SVZ046	3	Blanco at Cura-cautin	River	Winter	15.0	11.1	295.1	n.d.	1.15	64.8	7.1	34	-	4.15	-	-	-

Table 2: Continued

Sample ID	ID	Name	Type	Season	Cl	SO$_4$	HCO$_3$	CO$_3$	Li	B	Al	Fe	Ge	δ^{11}B	Ge/Si	δ^{13}C	DIC
					μmol/L	μmol/L	μmol/L	μmol/L	ppb	ppb	ppb	ppb	ppt	‰	μmol/mol	‰	μmol/L
SVZ050	4	Truful-Trulf	River	Winter	29.9	57.2	524.6	n.d.	1.9	15.6	8.0	3	-	14.49	-	-	-
SVZ049	5	Allipen	River	Winter	33.1	45.3	655.7	n.d.	4.8	32.6	8.3	38	-	4.58	-	-	-
SVZ052	6	Alpehue	River	Winter	31.1	29.2	557.4	n.d.	5.6	27.8	17.4	4	-	4.52	-	-	-
SVZ057	7	Trancura	River	Winter	19.8	27.5	426.2	n.d.	1.6	8.6	6.7	79	-	20.31	-	-	-
SVZ051	8	Voipir	River	Winter	14.4	6.9	491.8	n.d.	0.7	9.0	2.3	3	-	14.60	-	-	-
SVZ056	9	Palguin	River	Winter	19.5	37.7	426.2	n.d.	1.5	11.7	4.7	3	-	13.87	-	-	-
SVZ053	10	Liquiñe	River	Winter	18.9	45.3	311.5	n.d.	1.5	12.6	8.5	12	-	11.79	-	-	-
SVZ063	11	Caunahue	River	Winter	17.8	33.3	393.4	n.d.	0.4	9.4	9.0	20	-	4.18	-	-	-
SVZ060	12	Curriñe	River	Winter	19.8	58.8	409.8	n.d.	0.6	2.8	7.6	12	-	9.79	-	-	-
SVZ061	13	Nilahue	River	Winter	1262.1	104.6	1311.5	n.d.	11.2	373.0	7.5	44	-	6.30	-	-	-
SVZ055	14	Los Venados	River	Winter	19.2	11.1	623.0	n.d.	1.2	23.9	6.8	34	-	6.36	-	-	-
SVZ064	15	Chirre	River	Winter	84.2	5.3	295.1	n.d.	0.4	3.7	17.6	66	-	3.87	-	-	-
SVZ058	16	Gol-Gol	River	Winter	20.3	27.0	278.7	n.d.	0.7	3.0	5.6	8	-	2.48	-	-	-
SVZ062	17	Chanleufu	River	Winter	30.5	28.9	311.5	n.d.	2.4	10.1	6.9	7	-	1.32	-	-	-
SVZ065	18	Coihueco	River	Winter	27.4	6.6	344.3	n.d.	0.5	4.2	10.9	23	-	5.29	-	-	-
SVZ066	19	Blanco at R-225	River	Winter	26.3	3.8	245.9	n.d.	0.9	3.2	11.9	17	-	5.00	-	-	-
SVZ067	20	Chico	River	Winter	36.7	2.9	131.1	n.d.	0.4	2.8	121.6	150	-	5.47	-	-	-
SVZ069	21	Blanco at Chamiza	River	Winter	31.6	8.5	245.9	n.d.	0.8	7.3	10.1	138	-	-0.16	-	-	-
SVZ070	22	Chamiza	River	Winter	59.6	4.3	213.1	n.d.	0.8	6.7	44.8	148	-	-0.50	-	-	-

2.5. Results

2.5.1. Geochemistry of river waters

The river water samples analyzed in this study from the CSVZ have temperatures ranging between 9.7 to 20.7°C in the dry season and 4 to 9.8°C in the wet season. The maximum T° is detected in Nilahue River (13) at baseflow conditions. Conductivity values vary from 41.8 to 95.7 µS/cm in the dry season and from 25.7 to 50.4 µS/cm in the rainy season. CSVZ Rivers are characterized by neutral to alkaline pH values (7-8.1). TDS concentrations in the dry season range from 31.8-73.6 mg/l, except for the Nilahue River with TDS=329 mg/l. In the rainy season it is possible to observe dilution in the TDS concentrations, from 17.5-51.5 mg/l in 21 of the rivers, and in the Nilahue River TDS values decrease to 203.4 mg/l.

Figure 3 illustrates the relationship between major ions and silica concentrations with respect to chloride concentrations in all samples (river waters and thermal springs) during the dry and rainy seasons. Rivers have an enrichment of Ca+Mg with respect to K+Na (Figure 3.1-3-4), and bicarbonate is the dominant anion. All rivers are undersaturated in calcite except for Nilahue River (13). Mean SiO_2 concentrations in the rivers vary from 387.4 µmol/l in the dry season compared to an average of 299.5 µmol/l in the wet season. Chloride shows variable concentrations vary within an order of magnitude between the dry and rainy seasons, showing an increase in the dry season according to the base flow. The highest chloride concentrations were found for the Nilahue River with a concentration range of 1,261-2,089 µmol/l between winter and summer. Sulfate concentrations show the largest dilution effect in winter (Figure 3.2). In terms of the trace elements, the CSVZ rivers have B concentration ranges from 4.4 ppb (Curriñe River, 12) up to 897.4 ppb (Nilahue River, 13), with an average of 71.8 ppb. Eight out of the 22 rivers exhibit values below 20 ppb, mostly located south of 41°S. Regarding Li concentrations in the rivers range from 0.47 ppb (Caunahue River, 11) to 26.52 ppb (Nilahue River, 13). Thirteen out of the 22 rivers have values below 2 ppb, and excluding the Nilahue River (13), the average Li is 2.14 ppb. Aluminum and iron exhibit distinct behavior between summer and winter. In the dry season, Al concentration ranges from 3 ppb in Nilahue River (13) to 60 ppb in Voipir River (8), while Fe ranges from 3.3 ppb (Palguin River, 9) to 393.7 ppb (Chamiza River, 22). The average Al concentration is 11.4 ppb. Higher iron (>170 ppb) values are observed south of 41°S. During the rainy

season, Al concentrations increase in 14 of 22 rivers, with ~263% in rivers south of 41°S. Of way contrary, during the wet season iron decreases in 16 rivers (~41%), while the others show an increment of ~93%, with the maximum Fe concentration in Nilahue River (Figure 4).
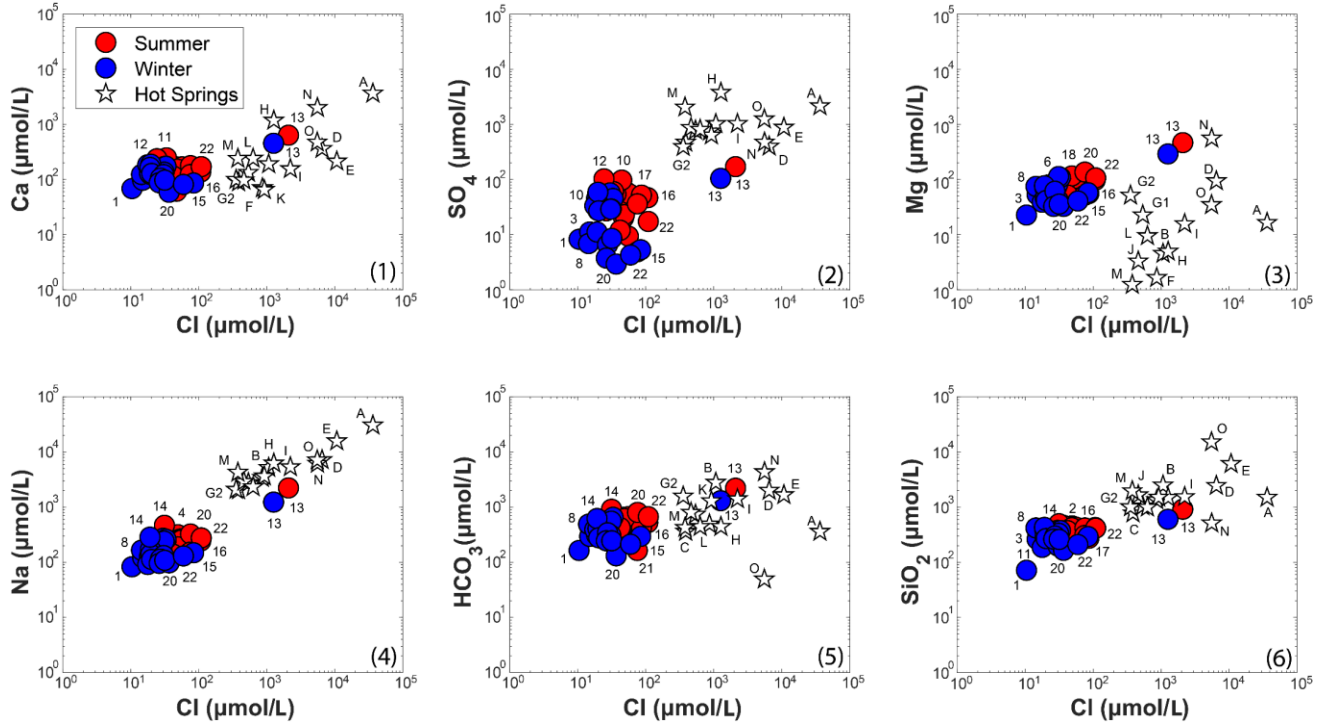
Figure 3: Ca, Na, Mg, SiO$_2$, SO$_4$ and HCO$_3$ concentrations against Cl for the sampled rivers (circles) and hydrothermal hot springs (white stars) in the SVZ. Red circles are river waters sampled during baseflow in the summer (Feb. 2021). The blue circles represent the rivers sampled during the high flow season in the winter (July 2021). For panel (3) it should be noted that two of the hot springs samples (Malalcahuello, C and Alpehue, E) have [Mg] < 0.4 µmol/L and do not plot in the graph space.

2.5.2. Geochemistry of thermal springs

The selected hot springs have a temperature ranging between 39-92°C, with a mean T = 62°C, and pH values from 8 to 9.2. Conductivity varies from 409.1 to 6,403 µS/cm, while TDS concentrations range between 205.9-3,201 mg/l. Na$^+$ and K$^+$ are the dominant cations, with minor concentrations of Ca+Mg. Cl$^-$ and SO$_4^-$ (Figure 3.2) are the principal anions in most of the samples, except for hot springs B, D, E, G.2, and K, where HCO$_3^-$ is the principal anion. Most of the springs are near or above saturation with respect to calcite and supersaturated with respect to quartz. Chloride shows a linear relation with Na (Figure 3.4), and

does not have linear tendency with Ca, SiO₂, and SO₄. Mg is characterized by lower concentrations with respect to rivers. The boron and lithium concentrations are one to two orders of magnitude higher than rivers, showing a wide range with mean concentrations of 7,547.8 ppb and 229.7 ppb respectively. For example, B concentrations in Chihuio hot spring (M) is 42.7 ppb, compared to hot spring 69,692 ppb in Malleco (B) hot spring. The Molulco-Balboa (D) hot spring has the lowest Li concentrations (3.42 ppb), whereas the highest Li concentrations reach up to 1,385 ppb in Alpehue (E) Hot spring.
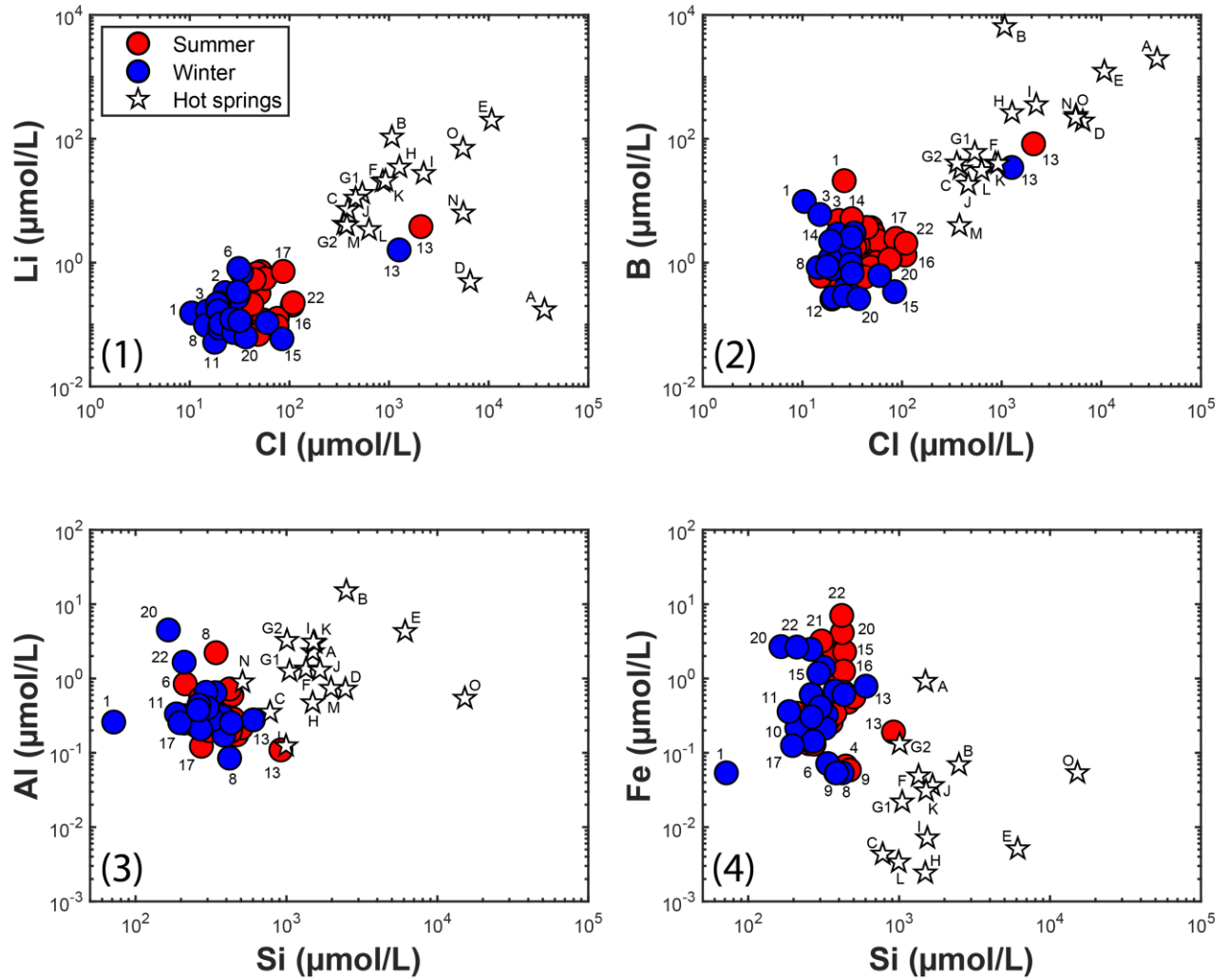
Figure 4: Trace elements in the sampled rivers (circles) and hydrothermal springs (stars). Panels 1-2 show Li and B concentrations against Cl. Panels 1-3 show Al and Fe concentrations against SiO₂.

2.5.3. Boron isotopic composition of river and thermal waters (δ^{11}B)

Boron isotopes are used in geochemistry to understand processes such as water-rock interactions and biogeochemical cycling, due to the high solubility of B and wide range of concentrations and isotopic compositions (δ^{11}B) in Earth systems (Lemarchand et al., 2005, 2007; Palmer & Sturchio, 1990; Rose et al., 2000). At low temperatures, boron is adsorbed and incorporated into clay minerals or adsorbed on clays and ferric oxides/hydroxides (Goldberg & Glaubig, 1985; Harder, 1970), with the light ^{10}B isotope preferentially uptaken into these phases, leaving dissolved boron enriched in ^{11}B (30‰; Marschall & Foster, 2018; Cividini et al., 2010). However, the mixing between weathering reactions, atmospheric input and biological recycling position rivers with δ^{11}B values in a range from -6 to 44‰ (Lemarchand et al. 2002; Spivack et al. 1987; Rose et al. 2000; Chetelat and Gaillardet 2005; Lemarchand and Gaillardet 2006, Chetelat et al. 2009; Marschall & Foster, 2018), therefore the hot springs should show a depletion of the heavy isotope with values of δ^{11}B from -10 to 20‰ (Marschall & Foster, 2018).While boron isotope fractionation due to water-vapor separation and the interaction with secondary altered minerals is not uncommon (Spivack and Edmond, 1987), these mechanisms generally do not lead to significant changes in the boron isotope composition of geothermal waters (Aggarwal et al., 2000). As a result, the boron isotope values found in geothermal waters (-10.5‰ to -54.9‰; see Aggarwal et al., 2000, 2003; Lu et al., 2012; Vengosh et al., 1991, 1994) are primarily influenced by the δ^{11}B signatures of their deeper sources (such as magmatic fluids, MORB and mantle δ^{11}B is uniform at -7±1‰; see Marchall et al., 2017) or the lithology of the reservoir rocks (-17‰ to -2‰ for igneous rocks; Marschall and Jiang, 2011; Pennisi et al., 2006; Vengosh et al., 1994; Xiao et al., 2013). At 25°C, the main B species is B(OH)$_3$ at pH < 9.3, whereas at higher pH values [B(OH)$_4$]$^-$ predominates (Vengosh et al. 1991; Sanchez-Valle et al. 2005). Schmidt et al. (2005) proved that in acidic fluids B(OH)$_3$ is the main species, but its concentration weakly decreases with addition of NaCl, and thus, [B(OH)$_4$]$^-$ concentrations can increase in near-neutral to basic fluids. The δ^{11}B composition of rainfall is ~45‰, slightly heavier than that of seawater (~39‰, Chetelat et al., 2005; Xiao et al. 2007). Rose-Koga et al. (2006) suggested that the vapor formed by the evaporation of seawater is enriched in ^{10}B, and when B condenses in clouds, a reverse isotopic fractionation occurs (~31‰), producing rainwater with heavier compositions. Rainfall can also have lighter δ^{11}B values, even below zero, which are explained by dissolution of atmospheric dust (Rose-Koga et al., 2006), contribution of biomass burning, anthropogenic emissions (Chetelat et al., 2009; Zhao & Liu, 2010), or fertilizer application (Roux et al., 2017). Figure 5.1 displays the CSVZ δ^{11}B data for both dry and

rainy seasons. $\delta^{11}B$ in the river waters during the dry season range from -1.32‰ to 12.22‰; whereas during the wet season $\delta^{11}B$ range between -0.16‰ to 20.31‰ with increasing dilution. Of our 22 rivers, only 11 of them show heavier $\delta^{11}B$ during winter, while all rivers ubicated south of 40.5°S are enriched during summer. Regarding hydrothermal springs, the values reported for $\delta^{11}B$ ranging from -0.71‰ (Malalcahuello, C) to 10.17‰ (Pemehue, A). Only two samples show values < 0‰ (A, E), while the mean of the rest is 3.8‰. Two distinctive groups appear when $\delta^{11}B$ is plotted against the Cl/B ratio for the dry season data: (1) rivers with Cl/B ratios < 40 and $\delta^{11}B$ values from -1.3‰ to 7.5‰, and (2) rivers with Cl/B > 40 and $\delta^{11}B$ from 5.3‰ to 12.2‰ (Figure 5.2).

2.5.4. Germanium concentrations and Ge/Si ratios in rivers and hot springs

We used the concentration of Ge and the Ge/Si ratio as complementary tracer for weathering and hydrothermal processes. (Mortlock and Froelich, 1987; Kurtz et al., 2002; Evans et al., 2002). Ge substitutes for Si in silicate minerals, with varying partitioning behavior based on silicate type (He et al., 2019). Thus, Ge/Si ratios vary between the different types of igneous rocks: felsic rocks, which contain higher proportions of quartz and/or feldspars show Ge/Si ~ 1-1.5 µmol/mol; and those with more mafic compositions can reach up to Ge/Si ~ 3 µmol/mol. (Bernstein, 1985; De Argollo & Schilling, 1978; He et al., 2019; Kurtz et al., 2002; Mortlock & Froelich, 1987). During incongruent weathering, Ge is partitioned between the fluid phase and secondary minerals, and Ge is preferentially incorporated into the solid phase (Kurtz et al., 2002). This results in high Ge/Si ratios (>3 µmol/mol) in soils and regolith, and low Ge/Si ratios in most river catchments fed by baseflow (0.1-3 µmol/mol; see Anders et al., 2003; Baronas et al., 2017, 2018; Froelich et al., 1985, 1992; Kurtz et al., 2002, 2011; Lugolobi et al., 2010; Meek et al., 2016; Mortlock &Froelich, 1987; Murnane & Stallard, 1990). Ge/Si values measured in rivers unpolluted reflect the mixing in both processes during incongruent weathering of primary silicates and the later congruent dissolution of secondary clays (Murnane and Stallard, 1990; Mortlock and Froelich, 1987; Froelich et al., 1992; Kurtz et al., 2002). However, high Ge/Si ratios in stream waters higher than those observed in silicate rocks, indicate either, the influence of solutes from geothermal systems (3-185 µmol/mol, in basalt-andesite terrains; see Arnòrsson, 1983, 1984; Escoube et al., 2015; Siebert et al., 2006; Wheat & McManus, 2008; Gasárd et al., 2021), and/or sulfide weathering (Anders et al., 2003; Evans et al., 2004; Evans & Derry, 2002; Han et al., 2015; Mortlock &

Froelich, 1987; Rosenberg et al., 2009.The combination of these processes and sources results in a large range reported for rivers draining other volcanic regions, mainly with basalt-andesite compositions (Ge/Si = 0.16-20 µmol/mol; e.g., Baronas et al., 2018, 2020; Derry et al., 2005; Scribner et al., 2006). Ge concentrations were measured only during the dry season, showing values ranging from 12.4 ppt (Caunahue, 11) to 248 ppt (Nilahue, 13), and only 8 of 22 rivers displayed Ge values >30 ppt. Note that rivers south of 41°S have Ge concentrations <15 ppt (Figure 5.2). Si abundance in the rivers is variable during the dry season, from 210 µmol/L (Liquiñe, 10) to 918 µmol/L (Nilahue, 13). While the wet season data show a decrease of concentration in 18 of 22 rivers (~30%). Thus, the Ge/Si ratios for the dry season in the CSVZ rivers range from 0.41 µmol/mol (Chirre, 15) to 4.43 µmol/mol (Liquiñe, 10). The lowest ratios are reported south of 41°S, with an average of 0.49 µmol/mol. Ge measured in hydrothermal springs showed values from 75.5 ppt (Lava 2011, N) to 61,091 ppt (Alpehue, E), and only four hot springs displayed values >10,000 ppt. The Si content varies from 15,208 µmol/L (Aguas Calientes, O) to 512 µmol/L (Lava 2011, N). Hot springs displayed a wide range Ge/Si value, ranging from 2.03 µmol/mol (Lava 2011, N) to 137.5 µmol/mol (Alpehue, E), with an average of 62.6 µmol/mol.

2.5.5. Inorganic carbon ($\delta^{13}C_{DIC}$)

Carbon isotopes are used as tracers to determine the origin of carbon consumed by weathering reactions (e.g., Evans et al., 2002; Becker et al., 2008). They can be used to differentiate between biogenic CO_2 and carbonate dissolution in soils (< -25‰, O'Leary, 1988; Cerling, 1984), magmatic (-5‰ to -10‰, Giggenbach, 1983), and atmospheric (-8 to -6‰, Cerling et al., 1991) carbon sources. In an open system -such as the unsaturated zone- there is a constant exchange between atmospheric (CO_{2atm}) and soil (CO_{2soil}) carbon dioxide. Therefore, there is a constant addition of CO_2 and increment of dissolved inorganic carbon (>DIC), but with lighter $\delta^{13}C$ signatures. Partial pressure of CO_2 (PCO_2) in soil is significantly higher than PCO_2 of the atmosphere, and thus CO_2 derived from the oxidation of organic matter and root respiration will readily dissolve in groundwater as it percolates (e.g., Cerling, 1984; Appelo and Postma, 2005). However, the atmosphere and soil are not the only CO_2 sources in volcanic contexts, and carbon isotopes can help to trace deep carbon. Additionally, calcite precipitation will decrease in DIC in fluids, while their $\delta^{13}C$ becomes heavier during the mixing of calcite saturated hydrothermal fluids with meteoric water (e.g., Chiodini et al., 1998,200; 2011; Evans et al., 2004; Frondini et al., 2008; Appelo y Postma, 2005) (see in Figure 5.3).

Here, we report negative values of $\delta^{13}C$ for the river waters in the dry season (Figure 5.2), with values ranging from -12.23‰ to -1.42‰. Only four out of 22 rivers reported values <10‰ (8, 18, 20, 22), while only three of them showed values >5‰ (6, 10, 13). The DIC concentrations range from 432 µmol/L (Malleco, 1) to 1,939 µmol/L (Nilahue, 13). Only three rivers (13,14,20) showed values above µmol/L, while the rest of them showed an average of 700 µmol/L. Hydrothermal springs have varying $\delta^{13}C$ compositions from -14.36‰ (Malalca-huello, C) to -6.17‰ (Apehue, E). Four hot springs showed values >10‰, while the others displayed an average of -14‰.
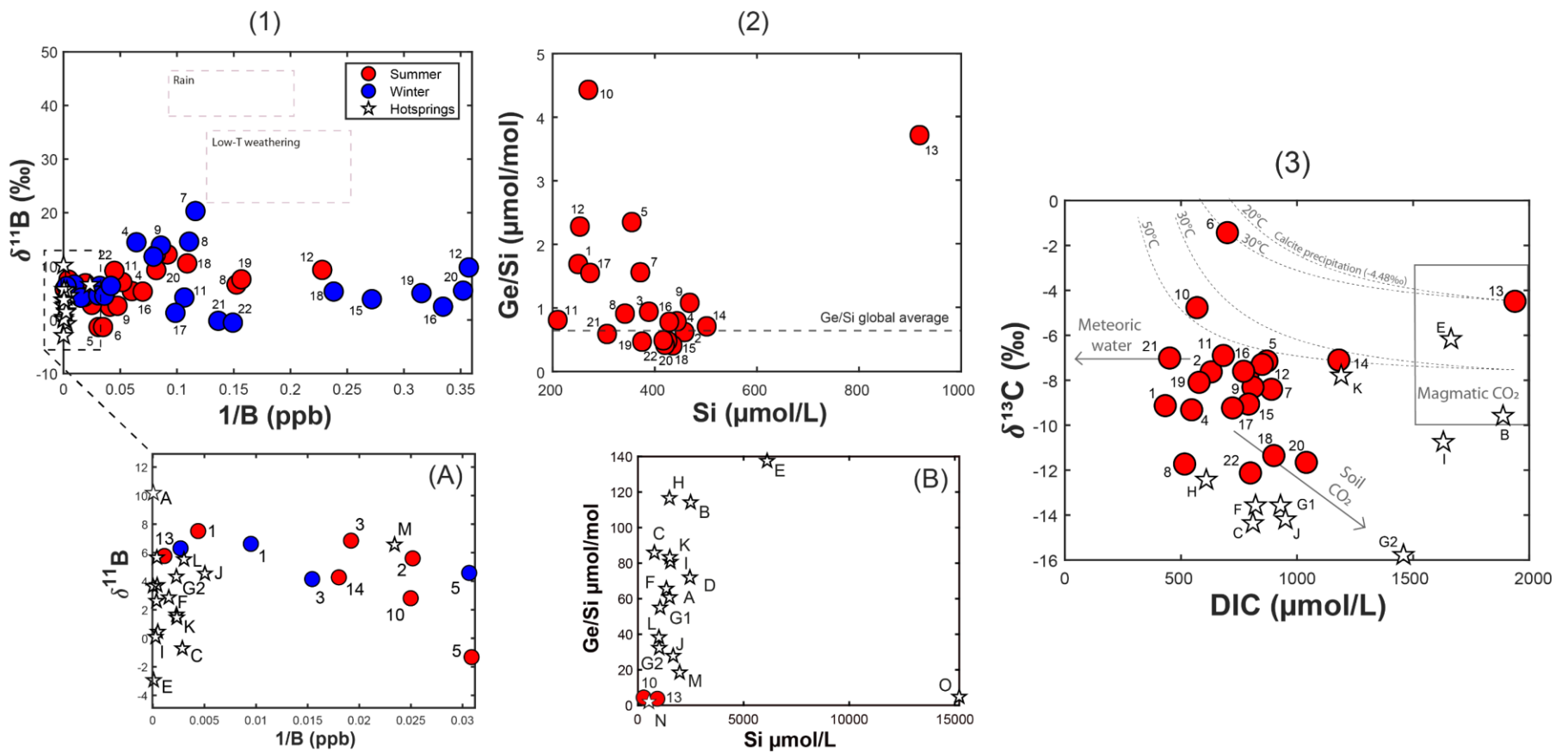
Figure 5: (1) Relationship between $\delta^{11}B$ and B concentrations rivers (circles) and hydrothermal springs (stars). The dashed pink field indicates the range of values reported by Louvat et al. (2014) in Réunion Island for rainfall and rivers unaffected by hydrothermal inputs; panel (A) is a zoom to the region represented by the hydrothermal springs (stars). (2) Ge/Si against Si concentration in rivers. The dashed line marks the Ge/Si global average for rivers unaffected by hydrothermal inputs, fly-ash or sulfide dissolution (0.6 pmol/μmol) (Mortlock and Froelich, 1987; Kurtz et al., 2002, 2011; Chillrud et al., 1994; Lugolobi et al., 2010; Froelich et al., 1985; Anders et al., 2003; Aguirre, 2019; Ameijeiras-Mariño et al.,2018; Baronas et al., 2018); panel (B) shows a zoom for the Ge/Si ratios for hot springs (stars). Note that Ge in Alpehue (6) river was not measured. (3) Relationship between carbon isotope ($\delta^{13}C$) and DIC (dissolved inorganic carbon) in rivers sampled in summer. $\delta^{13}C$ for magmatic CO_2 ranges between -3.5 to -10‰. The dashed lines are trajectories for CO_2 degassing by calcite precipitation at temperatures of 30–50°C from a magmatic source at -7.5‰, and at 20-30°C for a magmatic source with -4.48‰. Degassing was modeled in PHREEQC (Pérez-Moreno et al., 2021). The arrows "Soil CO_2" and "Meteoric water" indicate the expected paths of the catchments dominated by soil respiration, or atmospheric CO_2.

2.6. Discussions

2.6.1. Influence of hydrothermal springs on solute loads of rivers

The catchments present waters of the calcium/magnesium bicarbonate type, and the relationship between the Ca+Mg flux and the cationic Na flux is consistent with silicate weathering of mostly basalt-andesite to andesite rocks (Gaillardet et al., 1999; Viers et al., 2013). The mineral dissolution molar relationships for albite (Na-plagioclase), labradorite (intermediate plagioclase) and anorthite (Ca-plagioclase), show ratios with bicarbonate of 1:1 and 1:3 for Na/HCO_3, and 1:2 for Ca/HCO_3, respectively (Elango & Kannan, 2007; Krasny & Sharp, 2007; Lerman & Wu, 2008), while amphibole show a 1:3.5 ratio for Ca/HCO_3. The rivers show a positive correlation between Na and Ca with respect to bicarbonate (Figure 6). Ca vs HCO_3 and Na vs HCO_3 show that most of the samples fit with 1:3 trend, showing the labradorite dissolution. The case of mafic minerals, amphibole is observed in andesite rocks, and samples fit with 1:3.5 ratio between Ca vs HCO_3. However, the second relation (Na vs HCO_3) evidence a sodium enrichment, and water-rock interaction enhanced by hydrothermal or magmatic CO_2 is not able to explain all the Na content in rivers. Nilahue river shows an excess of sodium and fits with 1:1-trend in Na vs HCO_3. Excess Na over alkalinity is a common feature in the hot springs in SVZ where dissolution of albite is explained by the presence of additional sources of acidity (sulfate, chloride) besides carbonic acid (e.g., Daniele et al., 2020; Negri et al., 2018). After bicarbonate, the second predominant anion in the rivers is Cl, whereas sulfate is a minor component, and only the Nilahue River shows higher concentrations of sulfate (Figure 11). Additional acid sources may enhance water-rock interaction in the region (Giggenbach, 1988). Rivers located close to the Pacific Ocean can explain the excess of Cl (19, 20, 21, 22). However, most rivers are located further than 100 km from the coast, and thus, marine chloride and sulfate contribution is close to zero (less than 5%). In these catchments, the likely sources of Cl and SO_2 are inputs from hydrothermal systems, such as SO_2 and HCl from magmatic degassing. Identification of rivers in the CSVZ that are impacted by hydrothermal inputs is still uncertain. Hauser (1997) identified the hydrothermal springs in the region, with rivers in proximity to these springs, but the lack of hydrogeochemical data prevents drawing a further relationship. For this

purpose, we use four different chemical tracers (Cl, Ge/Si, and isotopes of B and C) to identify rivers impacted by hydrothermal inputs.
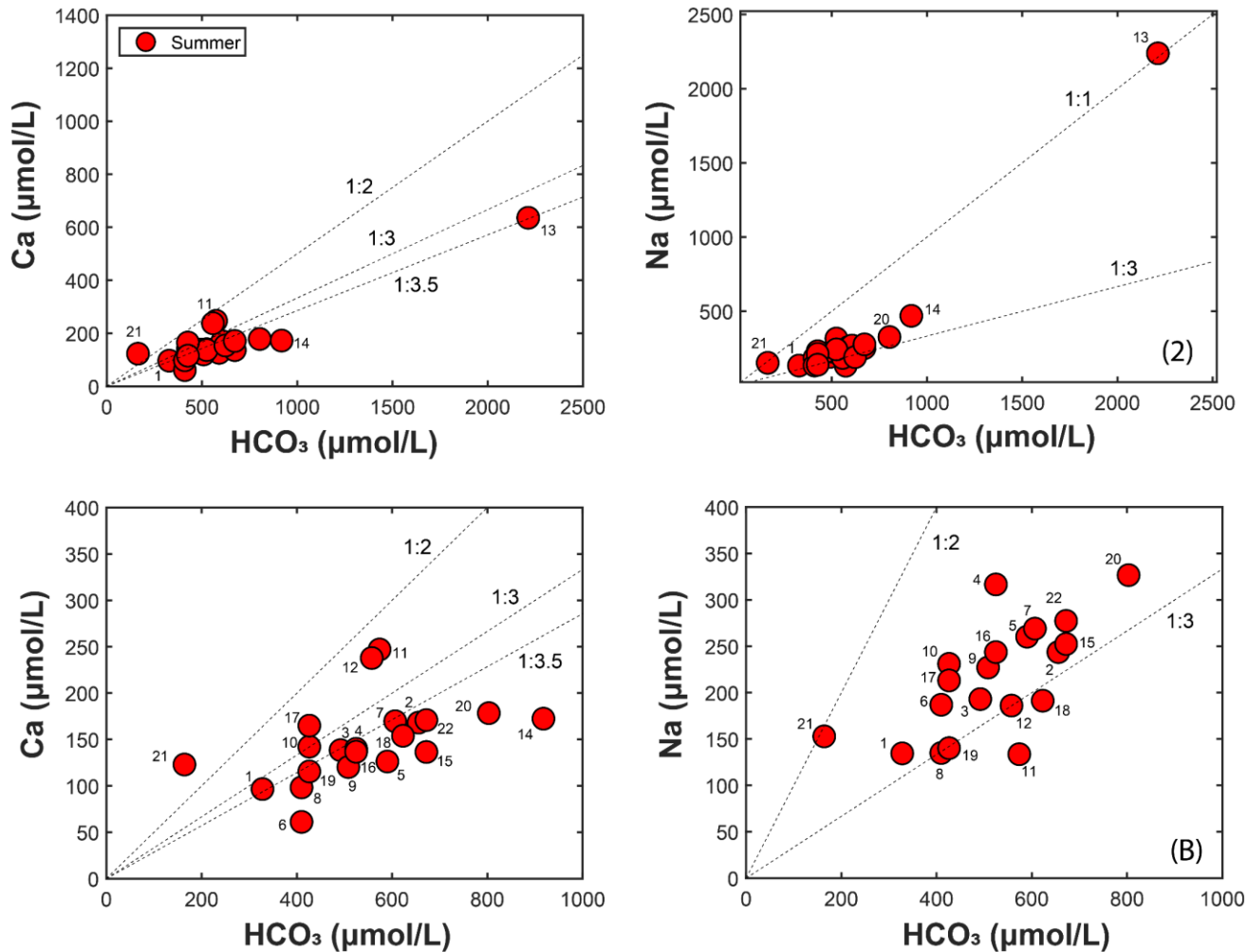
Figure 6: Molar relationships of (1) Ca vs. HCO_3 and (2) Na vs. HCO_3 showing the plagioclase dissolution (stoichiometry ratios): albite (1:1), anorthite (1:2), labradorite (1:3), amphibole (1: 3.5). The river samples show in red circles. (A) y (B) corresponds to a zoom of the lower left cluster of samples in panels (1) and (2).

2.6.1.1. Boron ($\delta^{11}B$, Cl/B) as tracer for hydrothermal inputs

Different authors have used the relationship between boron concentration and $\delta^{11}B$ (‰) to propose range of values for rain, soil/vegetation, hydrothermal and anthropic impact (e.g.: Rose et al., 2000; Chetelat et al., 2009; Xiao et al., 2013; Louvat et al., 2014). For this study, we did not measure the B concentration in rain samples. However, other authors have reported rainfall B concentrations below 3 ug/L (Daniele et al., 2020; Held et al., 2018). We

assume that rainfall in the SVZ has $\delta^{11}B$ >20‰ based on these low values and the minimal anthropic intervention in our catchments (Roux et al., 2017). Louvat et al. (2014) studied boron isotopic fractionation due to weathering in rivers with (high-T) and without (low-T) hydrothermal inputs. Rivers without hydrothermal impact, show low boron concentrations and isotopic fractionation due to clay formation ($\delta^{11}B_{river}$>20‰; see Figure 5). However, in rivers impacted by hydrothermal activity, the high-T water-rock interaction results in higher B concentrations and light $\delta^{11}B_{river}$ which are close to 0‰ ($\delta^{11}B_{river}$< 0‰ due to magmatic fluids and lithology of the reservoir rocks). Hot springs in CSVZ showed values of -2.94‰ to 10.17‰ for $\delta^{11}B$, with an average of ~3‰. The high values of $\delta^{11}B$ (2 of 16 samples reported values <0‰) are probably associated weathering of rocks at high temperature (approximately -2‰ in I-type granites; Marschall & Foster et al., 2018) and light-isotope boron adsorption onto secondary minerals precipitated during the transfer of these fluids to the surface (Louvat et al., 2014). In our study, $\delta^{11}B_{river}$ in rivers without hydrothermal influence only show variations in their boron concentrations between wet and dry seasons, with a limited range of $\delta^{11}B_{river}$ that is similar to rocks and hydrothermal fluids (Figure 5.1). The low $\delta^{11}B_{river}$ can be a result of limited water-rock interaction and minimal biological cycling of boron in these watersheds. The volcanic catchments in the SVZ have high slopes and small areas that results in short water transit times (less than 14 hours; see Annex F: Time of concentration) which could explain the minimal boron isotopic fractionation (Gaillardet & Lemarchand, 2018; Liu et al., 2012, Louvat et al., 2014). In contrast, transport-limited regimes with short water transit times, both active precipitation of soil clay minerals or oxides and active biological recycling are mechanisms for that allow for fractionation of boron isotopes, which result in the heavy $\delta^{11}B_{river}$ values observed in both Guadeloupe and La Reunion Island (Louvat et al., 2011; 2014).

Due to inconclusive results regarding $\delta^{11}B_{river}$, we integrated the $\delta^{11}B_{river}$ data with Cl/B ratios (see Figure 7). Chloride concentrations in thermal fluids have been employed to gather insights into the origin of these waters and to assess the mixing of thermal and non-thermal water sources (e.g., Arnórsson & Andrésdóttir, 1995; Cullen et al., 2021). In active hydrothermal systems, chlorine primarily originates from the degassing of cooling magma, mainly in the form of HCl (Aiuppa et al., 2009). The hot springs selected for this study exhibit an enrichment of Cl (chloride-sodium water type); hence, it is anticipated that this parameter will serve as a reliable indicator of hydrothermal influence. In most of the rivers, we can rule out high concentrations of B and Cl, attributable to the presence of seawater, evaporites, or

sedimentary rocks (Harder, 1970). Ellis & Mahon (1964; 1967) observed that Cl tends to dissolve more readily from volcanic rocks compared to B, especially from basalt. Nevertheless, as temperature increases, the Cl/B solution ratio tends to converge, moving from higher values towards the ratio in the respective rocks (Arnórsson & Andrésdóttir, 1995). The results of $\delta^{11}B_{river}$ vs Cl/B ratios allow to us define two groups associated with and without hydrothermal influence: (1) Cl/B ratios <40 are associated to the lightest $\delta^{11}B_{river}$ compositions (<7.5‰). (2) Cl/B >40 are associated with heavier $\delta^{11}B_{river}$ (>7.5‰) except for Gol-Gol River (16). The first group with Cl/B ratios smaller than 40 is associated with hydrothermal influence due to the similar $\delta^{11}B$ to the hydrothermal fluids and enrichment of boron, yielding low Cl/B ratios (Arnorsson, 1985; Fournier, 1977; White, 1970). The second group shows heavier $\delta^{11}B$ compositions due to enhanced mixing with rainfall and soil clays minerals formation or biological recycling. Additionally, this group also has low B concentrations and high Cl (due to seawater) in those rivers located south of 40.9°S. However, this classification is inconsistent in two rivers. The Curriñe River (12) which was sampled next to the Chihuio hot springs (M) has light $\delta^{11}B$ and high Cl/B. However, we attribute this apparent discrepancy to the low Cl and B in the Chiuio hot spring that discharges into the Curriñe River. The Gol Gol River (16), shows light $\delta^{11}B$ and high Cl/B (Figure 5.2) attributable to Cordón-Caulle eruption in 2011 and the composition of white pumice that possibly affects the chemical of the river (Daga et al., 2014; Pistolesi et al., 2015).

2.6.1.2. Ge/Si ratios as a hydrothermal input tracer

The CSVZ Rivers, display a wide range of Ge/Si ratios (0.41-4.43 µmol/mol) and are consistent with data reported for rivers draining volcanic regions with basalt-andesite compositions (Ge/Si = 0.16-20 µmol/mol) (e.g., Baronas et al., 2018, 2020; Derry et al., 2005; Scribner et al., 2006). Incongruent weathering results in low Ge/Si ratios in the fluids with respect to the parent rocks, whereas congruent weathering does not result in Ge to Si partitioning between the fluid and solid phases (Mortlock & Froelich, 1987: Froelich et al., 1992; Kurtz et al., 2002; Perez-Fodich and Derry, 2020). Thus, rivers with Ge/Si ratios above the average of silicate rock (> 2 µmol/mol), clearly show an additional process from weathering, such as sulfide oxidation or hydrothermal fluid input (Anders et al., 2003; M. J. Evans & Derry, 2002; Scribner et al., 2006). Since, sulfide minerals along with hydrothermal alteration in the surface are not widespread in the volcanic rocks in the SVZ, we can conclude these rivers show hydrothermal fluid inputs (Figure 5.2). All these rivers (5, 10, 12, 13) have active

thermal springs near them, and thus indicating that potentially the highest Ge/Si concentration originate from hydrothermal systems (Evans et al., 2004; Gaspard et al., 2021; Han et al., 2015) Rivers with Ge/Si ratios lower than the host rocks (e.g., <2 μmol/mol) represent a typical low to moderate-intensity weathering processes in continental rocks (Mortlock and Froelich, 1987). However, rivers with Ge/Si values within this range could also reflect mixing of fluids derived from incongruent weathering (closer to zero μmol/mol) and minor hydrothermal inputs (> 2 μmol/mol). The world average of "clean" rivers (those unaffected by sulfides or hydrothermal inputs) is 0.6 μmol/mol. Thus, we subdivided in two groups the rivers with Ge/Si < 2 μmol/mol. Those rivers with > 0.6 μmol/mol reflect both incongruent weathering and limited mixing with hydrothermal fluids (Gaspard et al., 2021; Han et al., 2015) The rivers below the world average of clean rivers, show minimal hydrothermal fluid influence, which correlates with their location far from active volcanic centers and absence of hydrothermal manifestations nearby. These unimpacted rivers are located south of 40.9°S (18-19-20-21-22) and have the lowest Ge concentrations (~13.6 ppt).

Identification of hydrothermal inputs using Ge/Si ratios is consistent with our results using $\delta^{11}B$ and Cl/B and the lack of geothermal systems detected proximate in these sites. Inconsistencies for the Ge/Si hydrothermal input tracer are observed for the Gol-Gol River (16) and Voipir Stream (8). These have Ge/Si > 0.6 μmol/mol and Ge content is 24.3 and 22.6 ppt respectively. The Voipir Stream is a very small catchment that receives mostly acidic snowmelt from the volcano summit, with very short water transit-times (1 to 4 hours), we conclude that these Ge/Si ratios mostly reflect congruent rock dissolution, without clay formation (Aguirre et al., 2017; Fernandez et al., 2021, 2022). The Gol Gol River is also an extreme case of congruent weathering, since it received the ashes -as pumice- of the 1921, 1960 and 2011 explosive eruptions of the Cordón-Caulle Volcano Complex (Lara et al., 2004; Singer et al., 2008; Castro et al., 2013). Finally, Cl/B and Ge/Si ratios allow to identify that 8 out of 22 rivers (8-15-16-18-19-20-21-22) are not influence by hydrothermal springs (Figure 7.1).

2.6.1.3. Carbon stable isotopes ($\delta^{13}C$) to investigate magmatic sources

To discriminate between CO_2 sources for the weathering reactions and the relative contribution of the volcanic degassing, we used carbon stable isotopes ($\delta^{13}C$) and the concentration of inorganic carbon in rivers and hydrothermal springs. Generally, the $\delta^{13}C$ signatures in rivers indicate a mixing between atmospheric CO_2 in equilibrium with rainwater (low

DIC, $\delta^{13}C \sim -7‰$) and soil CO_2 interaction (high DIC and $\delta^{13}C \sim -25‰$; Cerling, 1984; Genereux et al., 2009; Stefánsson et al., 2016). Additionally, it is possible that magmatic-derived CO_2 in hydrothermal springs ($\delta^{13}C > -6‰$, DIC >1000 µmol/L) is an additional component to DIC in some rivers in the SVZ. Degassing through calcite precipitation in high-alkalinity hot springs and rivers is also plausible, where in this case, the fluids will show heavier $\delta^{13}C$ compositions and low DIC depending on the degree of degassing. CO_2 loss by calcite precipitation is common as hydrothermal fluids ascend to the surface because of depressurization (Hilton et al., 1998; Ray et al., 2009). The composition of carbon isotope - and relation with other gases, such as He- in hydrothermal springs in SVZ has been described before in studies of Tardani et al., (2016), Pérez-Moreno et al. (2021) and Ray et al. (2009). They concluded that magmatic signature and calcite precipitation are the processes that control the isotopic signature in these systems. The thermal waters K, E, I, and B exhibit higher concentrations of DIC (>1000 µmol/L) and, at the same time, an enriched isotopic signature in ^{13}C (>-12‰), indicating an influence of magmatic CO2 degassing and subsequent impact from calcite precipitation due to the ascent of these flows. However, the samples H, F, C, G1-2 and J show lower values of $\delta^{13}C$ (< -12‰) where probably the interaction with magmatic gases is not predominant and the values are explained by calcite precipitation and direct interaction with groundwater in equilibrium with CO_2 soil. Most of the studied rivers show $\delta^{13}C$ values between higher than -10‰ and DIC < 1,040 µmol/L (14 of 22), whereas the rest show lighter $\delta^{13}C$ (< -10‰) with varying DIC concentrations (Figure 5.3). Rivers 18-20-22, with lightest $\delta^{13}C$ (-11‰ to -13‰), are characterized by high primary productivity and are located in the transition from the north temperate belt to a south temperate zone (Bannister et al., 2012), changing to a hyper-oceanic temperate system and the replacement of the vegetation to evergreen forests (Lieber & Pliscoff, 2006). The Voipir River (8) exhibits lighter $\delta^{13}C$ associated to snowmelt from the glacier on top of Villarrica volcano (Lacelle et al., 2008). The rivers with heavy $\delta^{13}C$ compositions from -7.01‰ and -1.43‰ and DIC ranging from 569 µmol/L to 1939 µmol/L (rivers 6-10-14-13) might indicate that degassing through calcite precipitation is present. For these rivers, we modeled calcite precipitation curves in PhreeqC assuming a CO_2 magmatic endmember (Ray et al., 2009; Tardani et al., 2016; Pérez-Moreno, 2021) (Figure 5). Our modeling results show that calcite precipitation can explain the $\delta^{13}C$ and DIC composition for only one river (Alpehue, 6) 30°C. However, the $\delta^{13}C$ and DIC in rivers 10 and 14 cannot be explained from calcite precipitation alone, as this will require reservoir temperature of 50°C or a magmatic $\delta^{13}C < -7.5‰$ (Figure

5.2). The Nilahue River (13) shows the highest DIC concentration (1,939 μmol/L) with the heaviest $\delta^{13}C$, both can be explained by the influence of magmatic gases.
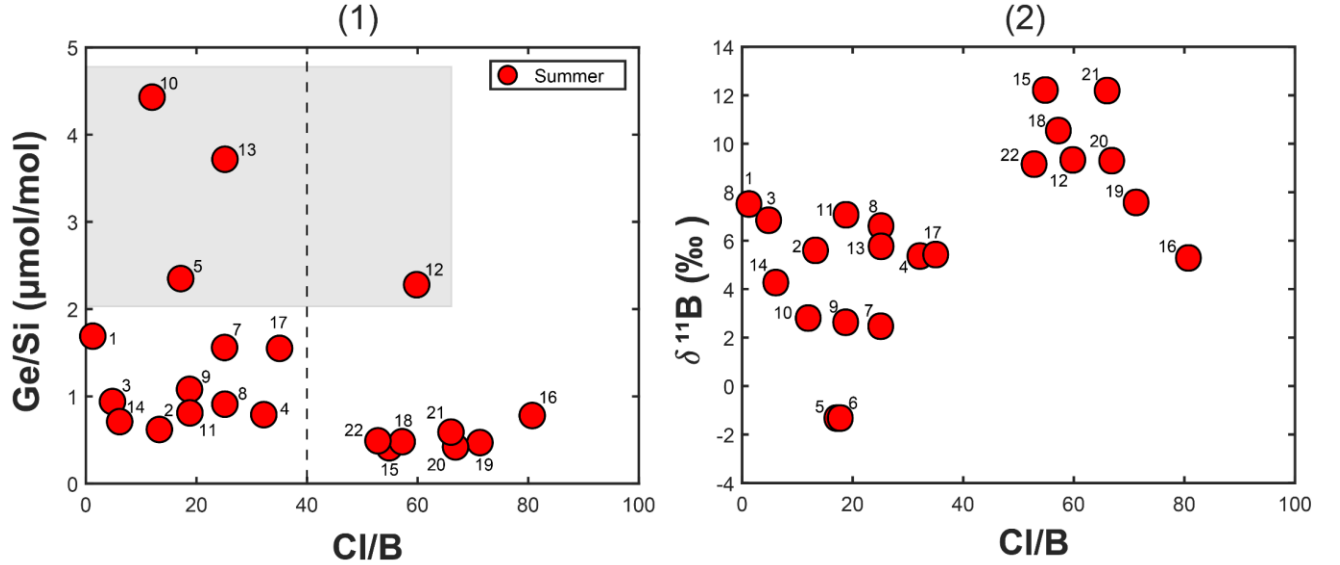
Figure 7: Panel (1) shows Ge/Si versus Cl/B, to discriminate catchments affected by hydrothermal inputs. Grey field includes samples with Ge/Si > 2 μmol/mol, above the mean value for igneous rocks. We associate this cutoff value with significant hydrothermal inputs. The groups rivers with Ge/Si ≤ 1.5 μmol/mol and Cl/B < 40 indicates mixing of low-T weathering sources (with varying degrees of congruency as 0.6 < Ge/Si ≤ 2) with varying thermal inputs. Note that this does not apply to the Voipir stream (8) (see text for explanation). Rivers with Cl/B > 40 are associated with low-T weathering given the limited sources of boron (high Cl/B ratio). Panel (2) shows $\delta^{11}B$ versus the Cl/B ratio for all rivers during baseflow (red).

2.6.2. Quantification of hydrothermal inputs in rivers using Cl budget and Ge/Si ratios

In volcanic regions, stream chemistry is influenced by geothermal sources, which provide additional sources of acidity for silicate weathering from carbonic, hydrochloric, and sulfuric acids, we will refer to this process as high-temperature weathering. Thus, we can write a mass-balance equation for the concentration of an element X in the river water (X=Na^+, K^+, Ca^{2+}, Mg^{2+}, Cl^-, SO_4^{2-}) as a sum of its different sources, including low-T weathering from carbonic acid, high-T weathering from hydrothermal sources, and rainfall inputs (Eq. 3).

$$[X]_{river} = [X]_{high\text{-}T° \ weathering} + [X]_{low\text{-}T° \ weathering} + [X]_{rain} \qquad (3)$$

We do not consider other solute sources, such as sulfide oxidation, carbonate rock weathering, evaporite dissolution, or anthropogenic deposition in our mass-balance equation, as these processes are not relevant in the studied watershed in the SVZ. First, sedimentary rocks rich in carbonate, pyrite, or evaporites are absent in our watersheds (Figure 2). The only sedimentary deposits correspond to glacial and fluvio-glacial deposits Pleistocene to Holocene age. On the other hand, the watersheds have low anthropogenic impact (Alvarez-Garreton et al., 2019), Excluding possible anthropogenic effects on weathering processes. Thus, to estimate the fraction of solutes originating from low-temperature chemical weathering and high-temperature water-rock interactions we decided to use two methods. The first method is based on the hydrothermal chloride budget after atmospheric corrections (Dessert et al., 2009; Shopcka et al., 2011; Hurwitz et al., 2010). The second method uses Ge/Si ratios in river waters and hot springs (Evans et al., 2004). We applied the two methodologies on rivers affected by hydrothermal inputs, which were previously selected using the different geochemical tracers. In both methods, we propagated the uncertainties associated to mean annual discharge for each catchment, and the variance in the hydrochemistry of the hydrothermal springs located upstream from the stream sampling point.

Before determining the hydrothermal inputs, we calculate the solute content of rainfall relative to cyclic chloride concentration using elemental ratios to Cl from local rainwater (Table 3). The atmospheric input of the major elements for each river was calculated using equation (4):

$$[X]_{rain} = [Cl]_{rain} \times \left[\frac{X}{Cl}\right]_{rain} \qquad (4)$$

Table 3: Major ion composition of local rainwater against total chloride. Data was obtained from Risacher et al., 2011. The local oceanic rainwater refers to the average between two samples taken ~0.4 and ~17 km from the coast of the Pacific Ocean at sea level (Hornopiren (41°S) and Puerto Varas (41°S). The mountain rainwater was obtained at ~90 km from the coast at 200 m.a.s.l. (Entre Lagos, 40°S).

Sample	Na/Cl	K/Cl	Ca/Cl	Mg/Cl	SO$_4$/Cl
Local oceanic rainwater[a]	0.8	0.1	0.3	0.1	0.2

Local mountain rainwater[a]	0.3	0.0	0.0	0.0	0.0

Eq. (4) has the (X/Cl) ratios of local rainfall used to calculate the rainfall (or atmospheric) inputs. For the studied watersheds we considered two different rainfall compositions depending on their proximity to the Pacific Ocean. The first composition corresponds to a local mountain area rainwater with minor sea influence, and the second compositions is from a coastal location (Risacher et al., 2011). The oceanic rainwater composition was only used for the rivers located south of 41°S which are less than 40 km from the Pacific Ocean (Figure 2). According to this method, the Cl_{rain} input in the CSVZ Rivers varies between 1% and 100% during the dry season and 2% to 100% during the wet season (Table 4)

Table 4: Percentage of chloride content from rain in rivers during the wet and the dry season. a: "local mountain rainwater" sample used for correction, b: "local oceanic rainwater" sample used for correction. *: river with hydrothermal influence.

ID	Name	Latitude	$[Cl]_{Rain}$ input Dry season	$[Cl]_{Rain}$ input Wet season
			%	%
1[a*]	Malleco	-38.22	88	100
2[a*]	Cautin	-38.43	47	100
3[a*]	Blanco at Curacautin	-38.46	99	100
4[a*]	Truful-Trulf	-38.84	47	77
5[a*]	Allipen	-38.87	45	70
6[a*]	Alpehue	-38.91	49	74
7[a*]	Trancura	-39.33	41	100
8[a]	Voipir	-39.38	100	100
9[a*]	Palguin	-39.42	63	100
10[a*]	Liquiñe	-39.73	52	100
11[a*]	Caunahue	-40.16	68	100
12[a*]	Curriñe	-40.20	95	100
13[a*]	Nilahue	-40.27	1	2
14[a*]	Los Venados	-40.35	73	100
15[a]	Chirre	-40.44	42	27
16[a]	Gol-Gol	-40.66	21	100
17[a*]	Chanleufu	-40.74	27	75
18[a]	Coihueco	-40.94	47	84
19[b]	Blanco at R-225	-41.23	100	100
20[b]	Chico	-41.42	90	100
21[b]	Blanco at Chamiza	-41.43	90	100

ID	Name	Latitude	[Cl]$_{Rain}$ input Dry season	[Cl]$_{Rain}$ input Wet season
			%	%
22[b]	Chamiza	-41.45	62	100

The remaining ([X]*=[X]-[X]$_{rain}$) corresponds to the sum between low and high temperature weathering. After the rainfall correction, we employ the Cl-budget methodology established by Dessert et al. (2009) and Schopka et al. (2011) to determine the fraction of solutes originating from hydrothermal fluxes discharging into each stream. Assuming that chloride is derived either from rainfall and hydrothermal springs (or high-T° weathering), is possible to determine Cl$_{geoth}$ (Eq. (5)). Thus, the solute content from high-temperature weathering follows Eq. (6), where the hydrothermal chloride (Cl$_{geoth}$) is multiplied by the elemental concentrations normalized to chloride in hot springs, where X=SiO$_{2(aq)}$, HCO$_3^-$, Na$^+$, K$^+$, Ca^{2+}, Mg^{2+}, Cl$^-$, SO$_4^{2-}$ (Eq. (6)):

$$[Cl]_{geoth} = [Cl]_{riv} - [Cl]_{rain} \qquad (5)$$

$$[X]_{geoth} = [Cl]_{geoth} \times \left[\frac{X}{Cl}\right]_{hot\ springs} \qquad (6)$$

The selection of hydrothermal ratios ([X/Cl]$_{hot\ springs}$) was based on their proximity to rivers. In cases where multiple springs existed within the basin, the average ratio was calculated and documented in Annex C: Assignation of hot springs in each method to determine the thermal input (Cl-Ge/Si). Consequently, each river possesses its ratio concerning hydrothermal chloride. As a result, each river has its own ratio concerning hydrothermal chloride. The only deviation from this correction sequence is observed for the ion HCO3. Initially, we corrected for hydrothermal input using the HCO$_3$/Cl ratio found in hot springs. Subsequently, we attribute the remaining HCO$_3$ to an atmospheric origin. Considering rainfall and geothermal contributions, the remaining solutes are attributed to low-temperature weathering (Eq (3)). In Table 5 the results are reported for each river and each chemical species.

Table 5: Proportion (in %) of Low-temperature chemical weathering (LT) and High-temperature chemical weathering (HT) in rivers of CSVZ with hydrothermal influence. Percentages were deduced from Ge/Si and X/Cl ratios. Bicarbonate is notified with atmospheric (atm) and hydrothermal sources. a: germanium concentration was not measured. *: Rain correction.

	SO₄*				Na*				K*				Ca*			
	Ge/Si method		Cl method		Ge/Si method		Cl method		Ge/Si method		Cl method		Ge/Si method		Cl method	
ID	LT	HT	LT	HT	LT	HT	LT	HT	LT	HT	LT	HT	LT	HT	LT	HT
1	91%	9%	86%	14%	92%	8%	88%	12%	98%	2%	97%	3%	100%	1%	99%	1%
2	100%	1%	49%	51%	100%	1%	46%	54%	100%	0%	90%	10%	100%	0%	97%	3%
3	98%	3%	100%	0%	98%	2%	100%	0%	100%	0%	100%	0%	100%	0%	100%	0%
4	100%	0%	96%	4%	99%	1%	88%	12%	100%	0%	95%	5%	100%	0%	100%	0%
5	98%	2%	94%	6%	95%	6%	84%	16%	98%	2%	94%	6%	100%	0%	99%	1%
6ᵃ	-	-	88%	12%	-	-	81%	19%	-	-	93%	7%	-	-	99%	1%
7	93%	7%	44%	56%	94%	6%	50%	50%	99%	1%	96%	4%	100%	0%	98%	2%
9	94%	6%	65%	35%	94%	6%	67%	33%	99%	1%	95%	5%	99%	1%	97%	4%
10	85%	15%	75%	25%	72%	28%	56%	44%	95%	5%	91%	9%	99%	1%	98%	2%
11	95%	5%	76%	24%	94%	6%	70%	30%	99%	1%	97%	3%	100%	0%	98%	2%
12	54%	46%	93%	7%	48%	52%	92%	8%	83%	17%	97%	3%	98%	2%	100%	0%
13	0%	100%	0%	100%	0%	100%	0%	100%	0%	100%	5%	95%	0	100%	0%	1005
14	0%	100%	98%	2%	0%	100%	98%	2%	0%	100%	98%	2%	0	100%	98%	2%
17	78%	22%	71%	29%	71%	29%	61%	39%	88%	12%	85%	15%	97%	3%	96%	4%

	Mg*				SiO₂*				HCO₃*			
	Ge/Si method		Cl method		Ge/Si method		Cl method		Ge/Si method		Cl method	
ID	LT	HT	LT	HT	LT	HT	LT	HT	Atm	HT	Atm	HT
1	100%	0%	100%	0%	98%	2%	97%	3%	99%	1%	98%	2%
2	100%	0%	100%	0%	100%	0%	87%	13%	100%	0%	91%	9%
3	100%	0%	100%	0%	100%	1%	100%	0%	100%	0%	100%	0%
4	100%	0%	100%	0%	100%	0%	97%	3%	100%	0%	99%	1%
5	100%	0%	100%	0%	98%	2%	95%	5%	100%	0%	99%	1%
6ᵃ	-	-	100%	0%	-	-	94%	6%	-	-	99%	1%
7	100%	0%	100%	0%	98%	2%	86%	14%	100%	0%	97%	3%
9	100%	0%	99%	2%	99%	1%	93%	7%	99%	1%	93%	7%
10	100%	0%	100%	0%	89%	11%	82%	18%	95%	5%	92%	8%
11	100%	0%	100%	0%	98%	2%	92%	8%	100%	0%	99%	1%
12	100%	0%	100%	0%	83%	17%	97%	3%	98%	2%	100%	0%
13	0%	100%	55%	45%	0%	100%	79%	21%	0%	100%	27%	73%
14	4%	96%	99%	1%	86%	14%	100%	0%	35%	65%	99%	1%
17	99%	1%	99%	1%	52%	48%	36%	64%	100%	0%	100%	0%

Figure 8 provides a visual representation of the different solute sources. Four rivers displayed a Cl_{geoth} above 55% (5, 7, 13, 17), while the rest of them showed values ~30%. The contribution of hydrothermal or magmatic-derived bicarbonate is generally negligible (0.1 - 8%) except for the Nilahue River (13). The Nilahue River has up to 73% of magmatic or hydrothermal-derived alkalinity, which agrees with its strong hydrothermal influence. Overall, in rivers the contributions of Na (~30%), SiO_2 (~12%), and SO_4 (~26%) are noteworthy. However, for Ca (~9%) and Mg (~3%), it becomes apparent that the low-temperature weathering processes is predominant in most of the rivers, except for Nilahue (13). Nevertheless, it is important to consider potential limitations in the interpretation. The Mg/Cl and Ca/Cl ratios are relatively low, suggesting a possibility of overestimating the contribution from low-temperature weathering. The method used by Dessert et al. (2009), using Cl as a tracer of high-temperature weathering, is generally effective and shows consistency with proximity to hot springs and the behavior of hydrothermal tracers (Ge, Cl, B and isotopes $\delta^{11}B$, $\delta^{13}C$). However, it should be noted that in streams influenced by hydrothermal systems dominated by other acids, such as H_2S, it may not yield accurate results (e.g., Curriñe River (12)) and underestimate the hydrothermal input. The case of the Nilahue River is anomalous due to its exceptionally high chloride content (2,089 µmol/L) compared to the average content in other rivers (~52 µmol/L). As a result, there is a possibility that the contribution of low-temperature weathering in this river is underestimated. Due to the high Cl content in the Nilahue River, it is possible that there are other hydrothermal sources besides the Lava 2011 spring across the catchment area that may contribute to the high solute flux. The hydrothermal chemical fluxes show an impact on solutes in rivers of CSVZ. Our high-T silicate weathering estimates using Cl-budget range from 0.2% to 81% with an average of 11% of the total solute-weathering flux (Table 6).

Table 6: Fraction of chemical fluxes in rivers from high-T° weathering. Data shows cation (Na*+Mg*+K*+Ca*) and silicate fluxes (Na*+Mg*+K*+Ca*+SiO₂). b: germanium concentration was not measured, a: hot spring references are not mathematically consistent)

ID	Hydrothermal cation flux with Cl method		Hydrothermal silicate flux with Cl method		Hydrothermal cation flux with Ge/Si method		Hydrothermal silicate flux with Ge/Si method	
	%	±σ (%)	%	±σ (%)	%	±σ (%)	%	±σ (%)
1	6.0	4.0	4.7	2.7	4.1	2.9	3.1	2.0
2	25.0	16.0	19.0	11.0	0.3	0.2	0.2	0.2
3	0.2	0.1	0.2	0.1	1.0	0.7	0.8	0.5
4	7.2	0.0	5.5	0.0	0.4	0.1	0.3	0.1
5	8.6	0.0	6.9	0.0	2.9	0.3	2.4	0.3
6[b]	10.4	0.0	8.9	0.0	-	-	-	-
7	24.3	0.0	20.3	0.0	3.1	0.4	2.6	0.3
9	17.0	4.0	11.9	2.7	3.1	1.0	2.2	0.7
10	23.0	8.0	21.0	7.0	14.0	8.0	13.0	8.0
11	9.8	0.0	9.2	0.0	2.1	0.4	1.9	0.4
12	3.2	0.0	3.0	0.0	21.2	2.5	19.9	2.3
13[a]	97.3	0.0	81.4	0.0	-	-	-	-
14[a]	1.8	0.0	1.2	0.0	-	-	-	-
17	20.0	0.0	36.6	0.0	15.0	1.9	27.4	3.4

Considering the heterogeneity and the difference in chemical composition of hydrothermal systems in the rivers of the southern Andean region, we conducted a comparative analysis of the hydrothermal inputs using Ge/Si ratios. This analysis followed the mass-balance equation proposed by Evans et al. (2004) (Eq. 7). This equation assumes as endmembers the mean Ge/Si ratio of rivers unaffected by hydrothermal input, and Ge/Si ratio of the nearest hot springs (distance criteria). We assume that Ge/Si in each river is the weighted sum of the high-T weathering from hot springs, and from low-T weathering fraction, and that Ge and Si behave conservatively during mixing. The relation is:

$$F_{HS} = \frac{[Si]_{no-HS}}{[Si]_{HS}} \times \frac{\left[\frac{Ge}{Si}\right]_{riv} - \left[\frac{Ge}{Si}\right]_{no-HS}}{\left[\frac{Ge}{Si}\right]_{HS} - \left[\frac{Ge}{Si}\right]_{riv}} \qquad (7)$$

F_{HS} is the fraction of the total solute flux contributed by the hot springs. Subscript *HS* denotes average hot spring values for each basin, *no-HS* denotes all non-spring affected low-T weathering inputs. $(Ge/Si)_{no-HS}$, = 0.48 ± 0.1 µmol/mol and it is the average of 6 representative rivers without hydrothermal impact with $Si]_{no-HS}$ = 396 ± 44 µmol/L (15-18-19-20-21-22). $(Ge/Si)_{riv}$ is the Ge/Si ratio measured in each stream. $(Ge/Si)_{HS}$ and $[Si]_{HS}$ are mean values from the sampled springs in each catchment.

The calculated fractions of solute fluxes derived from hydrothermal fluids (F_{HS}) showed an average of ~9%, ranging from 0.015 ± 0.003% of the total flow for Truful-Truful River (4) to 2.2 ± 0.3% for Curriñe River (12). The uncertainties associated with this method are related to the Ge/Si ratio of endmember: hydrothermal ratios and rivers without hydrothermal influence. Compared to hot springs in central Nepal (Evans et al., 2004), where Ge/Si ratios are in average higher (262 µmol/mol) than those in the CSVZ (63 µmol/mol). At the same time, the mean of Ge/Si rivers reported in central Nepal is 5 µmol/mol, almost 5 time higher than rivers in CSVZ, with an average of 1.2 µmol/mol. This suggests that the Ge/Si mass-balance may not be the most suitable method to estimate the hydrothermal contribution for some rivers. Since the different between the high-T and low-T endmembers is less apparent in the CSVZ, it could lead to an overestimation of solutes fluxes from low-T weathering processes. Both silica and Ge are abundant in the CSVZ hot springs and rivers, which in turn, yield lower Ge/Si ratios compared to those in the Nepali hot springs which are poor in silica. The limitation on the use of Ge/Si mass-balance is evident for the rivers 2, 7, 12, 13 and 14 when compared to the Cl-budget. The hydrothermal input from the Ge/Si mass-balance is up to 1 order of magnitude less compared to the X/Cl method for the Cautin (2) River. In the case of the Nilahue (13) and Los Venados (14) Rivers, both present difficulties given the fact that the selected hot spring has the lowest Ge/Si ratio among the hot springs (~2 µmol/mol), and it is even lower than the Ge/Si ratio measured in the Nilahue River (3.71 µmol/mol). Thus, we cannot apply the Ge/Si mass/balance in this case, as it would yield negative results. Overall, the Cl-budget method is more consistent among the studied catchments for estimating hydrothermal inputs. However, we must note that the Ge/Si mass-balances has advantages when the hot springs do not correspond to Cl-rich waters. This can be exemplified in the Curriñe River (12), where the Cl-budget yielded close to 3% hydrothermal input, despite being directly downstream from a hydrothermal manifestation (Chiuio, M). In this case, the Ge/Si mass-balances yielded a total of 20% of hydrothermal input (Table 5).

In general, both chemical tracers exhibit consistent patterns in most rivers, but they do have certain limitations that can be influenced by various factors such as vegetation, time of transit, presence of young volcanic deposits and hydrothermal water chemistry. In our study area, where the watersheds exhibit different conditions and the chemical composition of the hot springs contained in each catchment is variable. The combination of multiple tracers could yield better results, particularly applying both tracers to an inverse scheme (e.g., Negrel et

al.,1993; Gaillardet et al.,1999; Louvat and Allegre, 1997; Kemeny and Torres, 2021). On the other hand, geothermal fluids change along the flow path from their source to the river (e.g., cooling, re-equilibrium with atmosphere, degassing, precipitation of secondary minerals, mixing with meteoric fluids). Therefore, it is possible that as these processes modify the chemical composition of the geothermal fluids, our ability to estimate the hydrothermal footprint observed in some rivers may be hindered. With that in mind, we conclude that the Cl-budget yields the most consistent results to estimate the hydrothermal input to the rivers in the CSVZ, since most hot springs correspond to chloride-sodium type waters. The Ge/Si mass-balances is useful when non-chloride rich hot springs are present in the catchment area.
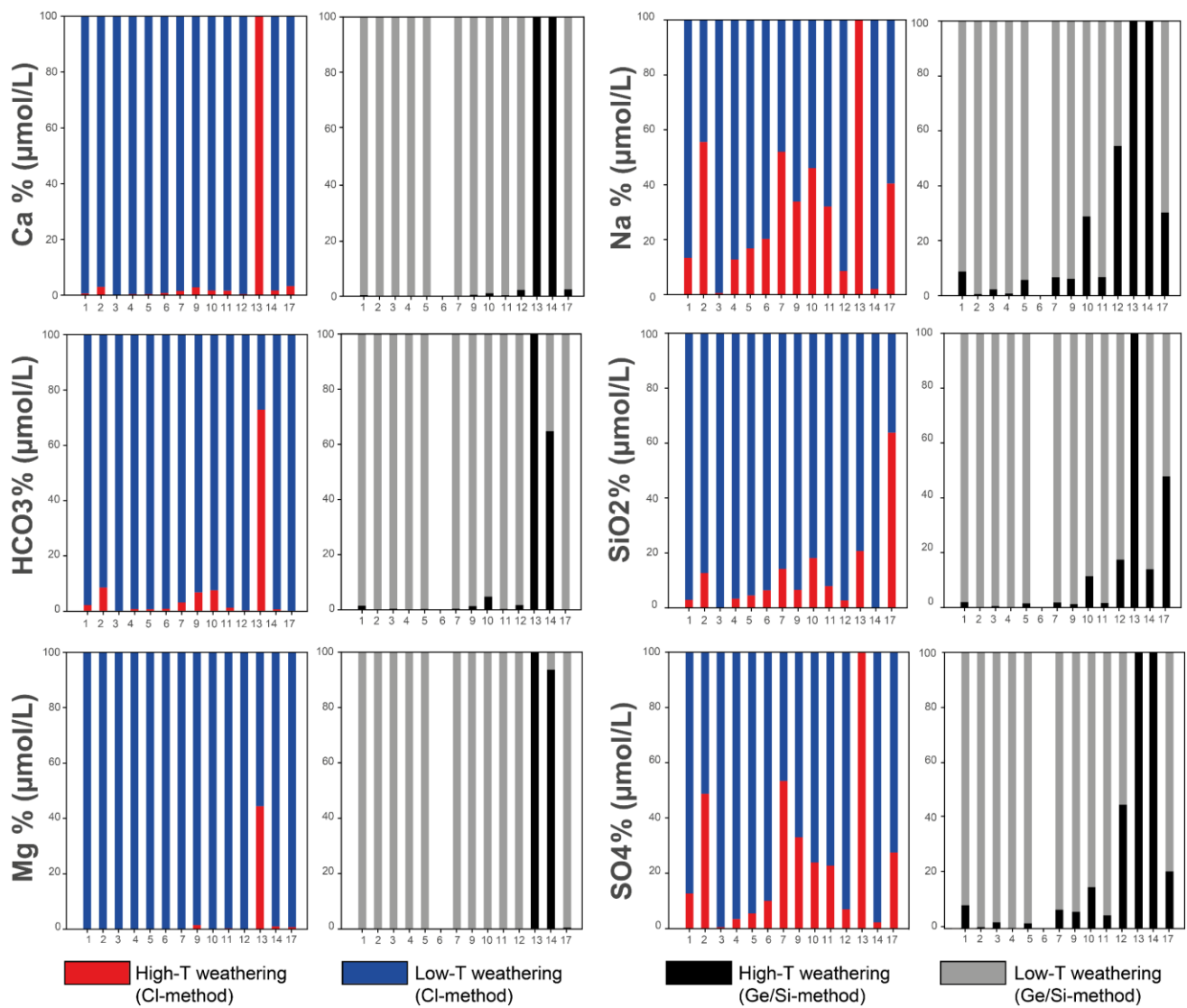
Figure 8: Stack column diagrams showing the proportions of Ca, HCO₃, Mg, Na, SiO₂, and SO₄ arising from both end members (Low-T and High-T weathering), once the atmospheric correction is done, in the chemical composition of 14 rivers with hydrothermal influenced. The figure shows the results for both methods (Cl and Ge/Si) for each ion. In the figures corresponding to Ge/Si method, the rivers 6, 13 and 14 does not show, due to the germanium concentration of Alpehue River (6) not being measured and Nilahue-Los Venados River (13-14) with the Lava 2011 hot springs, showing an inconsistent in the Eq. (5) (see text for explanation).

2.6.3. Solutes fluxes and chemical weathering budget in the Southern Andes

To determine the balance of chemical weathering from the volcanic basins to the Pacific Ocean in the Southern Andes, we used annual discharge data and solute concentrations measured in this study. In the discussion that follows, we treat high- and low-temperature weathering products as a single category: solutes derived from silicate weathering. At the same time, we refer to the speed of cationic weathering, which corresponds to the sum of the substances Ca, Na, Mg and K, from the weathering of silicates. Additionally, we consider the silicate weathering rate, which encompasses the solute flux of cations plus the concentration of SiO_2 derived from silicate weathering. In this context, we evaluate the transport of these solutes from volcanic basins to the Pacific Ocean in the Southern Andes region.

Silicate weathering rates in Central South Volcanic Zone have an average value of 87 ton/km²/yr with a range from 33 to 386 ton/km²/yr (Figure 9). While export cation fluxes range from ~11 to 243 ton/km²/yr in rivers with hydrothermal influence and ~20 to 35 ton/km²/yr in rivers without hydrothermal input. The area normalized export fluxes are higher than some of largest rivers in the world like the Congo (4.2 ton/km²/yr) or the Amazon (13 ton/km²/yr) (Gaillardet et al., 1999). The export fluxes in the Sourthern Andes are comparable to other volcanic regions including Kamchatka (16-34 ton/km²/yr) (Dessert et al., 2009), La Reunion (106 ton/km²/yr) (Louvat and Allegre, 1997), Philipines (35-241 ton/km²/yr) (Schopka et al., 2011)), Lesser Antilles (100-120 ton/km²/yr) (Rad et al., 2013), Yellowstone (93 ton/km²/yr) (Hurwitz et al., 2010), Iceland (39 ton/km²/yr) (Gislason et al., 1996). The highest solute fluxes, and thus, silicate weathering rates (>100 ton/km²/yr) are observed in those rivers with high hydrothermal contribution (>10%, rivers 9-13) and in rivers 16 (Gol-Gol) and 14 (Los Venados) where the high rates are probably related to the recent volcanic deposits of the Cordón-Caulle Volcanic Complex during the 2011 eruption. Respect to solute fluxes from high-T weathering, we concluded that rivers receive 11.3±0.7% on average of hydrothermal input in silicate fluxes, which is in the lower end when compared to other volcanic regions such as Luzon with ~10% (Schopka et al., 2011), 83% of the cation flux in Yellowstone (Hurwitz et al., 2010), or ~25% in Kamchatka (Dessert et al., 2009). Some of the highest (>80 ton/km²/yr) low-temperature weathering rates for the Southern Andes are associated to rivers (13-14) draining the Puyehue-Cordon Caulle Volcanic Complex, which has the highest extruded volume (755.1 km³; Volker et al., 2011) and total erupted mass from 1980 to 2019 in CSVZ (Galetto et al., 2023). This pattern is also observed in other volcanic

regions, such as the Philippines (Schopka et al., 2011), where recent volcanic deposits are easily eroded. In the other hand, the lowest weathering rates are mainly associated with low runoff (Table 7). There is a high difference between cation and silicate fluxes which is associated to the high silica concentration in rivers of CSVZ. The high silica fluxes in the region probably result from the high rates erupted subaerial mass in region (Galetto et al., 2023). Additionally, soil substrates might be only partially silica depleted given the constant resurfacing from volcanic activity. Biological uptake of silica is unknown in the Southern Andean forests. However, the short transit-times across the volcanic watersheds probably contribute to the low silica retention either in soils or biomass (Millot et al., 2002).

To extrapolate the weathering rates to the whole Southern Andean volcanic arc, we express the exports fluxes normalized for total Central South Volcanic Zone area (78,617 km^2), the mean silicate export flux from Southern Andes is 6.8 $\pm$0.4 x 10^6 ton/yr, based on the average chemical weathering rate of 87 $\pm$ 5 ton/km^2/yr.
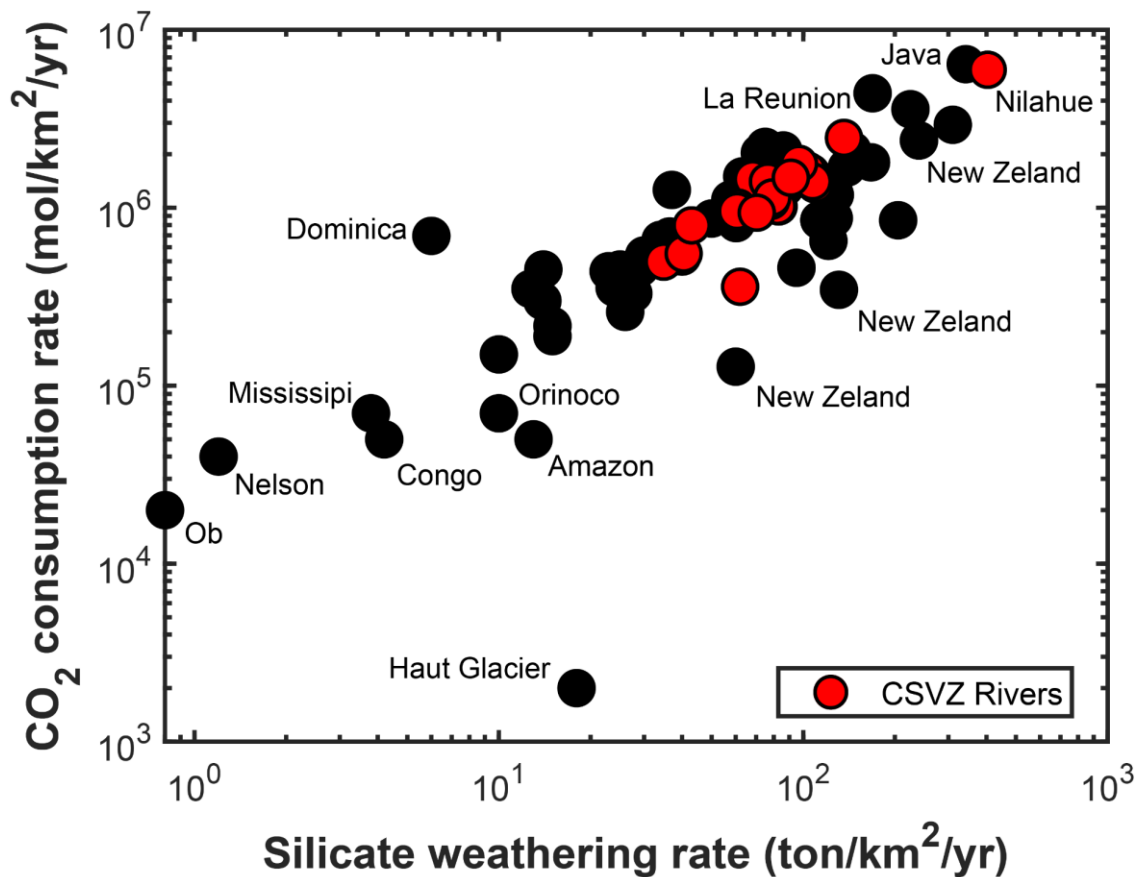
Figure 9: Relationship between the fluxes of derived from chemical weathering of silicates and the flux of CO_2 consumption rate (alkalinity flux). The figure shows the values obtained in this study (CSVZ Rivers, red circles) and other rivers around the world. Global data was obtained from Goldsmith et al. (2008); Schopka et al. (2011); Louvat and Allegre (1997); Louvat and Allegre (1998); Gaillardet et al. (1999); Benedetti et al. (1994); Negrel and Deschamps (1996); Rad et al. (2006); Dessert et al. (2003); Dessert et al. (2009); Gislason et al. (1996); Goldsmith et al. (2010).

Table 7: Runoff (mm/yr) and area (km²) for each basin. Low-temperature rock weathering values reported for rivers in the CSVZ. The fraction of solutes dissolving silicates from hydrothermal sources. Cation weathering rate (Na*+K*+Mg*+Ca*), silicate weathering rate (cations + SiO₂), and CO₂ consumption rate for each basin. a: river where we used Ge/Si ratios for quantify the hydrothermal input, the other data reported correspond to Cl method. b: germanium was not measured. Uncertainties in total chemical fluxes are associated with mean discharge annual (see text for explanation).

ID	Runoff	Area	Low-T silicate weathering rate	%Hydrothermal Input	Cation weathering rate	Silicate weathering rate	CO₂ consumption rate	
	mm/yr	Km^2	ton/km^2/yr	%	ton/km^2/yr	ton/km^2/yr	ton/km^2/yr	10^6 mol/km^2/yr
1	1452	58	31 ± 9	4.7 ± 2.7	11 ± 3	33 ± 9	29 ± 8	0.5 ± 0.1
2	1599	1595	57 ± 15	19 ± 11	24 ± 6	68 ± 16	64 ± 15	1.0 ± 0.2
3	1072	202	38 ± 9	0.2 ± 0.1	13 ± 3	38 ± 10	32 ± 8	0.5 ± 0.1
4	1823	476	73 ± 16	5.5	27 ± 6	76 ± 17	58 ± 13	1.0 ± 0.2
5	1819	593	60 ± 13	7.0	24 ± 6	63 ± 14	65 ± 15	1.1 ± 0.2
6[b]	1817	205	36 ± 8	8.9	16 ± 4	39 ± 9	45 ± 10	0.7 ± 0.2
7	2595	564	82 ± 17	20.3	41 ± 8	99 ± 20	96 ± 20	1.6 ± 0.3
8	2595	39	75 ± 15	0	22 ± 4	75 ± 15	65 ± 13	1.1 ± 0.2
9	2592	131	95 ± 20	11.9 ± 2.7	32 ± 7	105 ± 22	80 ± 17	1.3 ± 0.3
10	2582	449	60 ± 13	21 ± 7	32 ± 7	74 ± 15	67 ± 14	1.1 ±0.2
11	2438	457	60 ± 15	9.2	34 ± 9	65 ± 16	85 ± 22	1.4 ±0.4
12[a]	2435	331	66 ± 17	19.9 ± 2.3	36 ± 9	73 ± 18	83 ± 21	1.4 ± 0.3
13	2586	477	113± 21	81.4	243 ± 45	386 ± 71	349 ± 64	5.7 ± 1.1
14	2584	297	128 ± 24	1.2	51 ± 9	129 ± 24	145 ± 27	2.4 ± 0.4
15	1425	444	58 ± 13	0	20 ± 5	58 ± 13	58 ± 13	1.0 ± 0.2
16	2577	714	102 ± 19	0	35 ± 7	102 ± 19	82 ± 15	1.4 ± 02
17	2574	73	42 ± 8	36.6	32 ± 6	75 ± 14	67 ± 12	1.1 ± 0.2
18	1519	484	59 ± 11	0	20 ± 4	59 ± 11	58 ± 11	0.9 ± 0.2
19	2152	268	68 ± 12	0	15 ± 3	64 ± 11	56 ± 10	0.9 ± 0.2
20	2150	199	94 ± 17	0	35 ± 6	90 ± 16	105 ± 19	1.7 ± 0.3
21	2147	183	60 ± 11	0	16 ± 3	56 ± 10	21 ± 4	0.4 ± 0.1
22	2148	91	88 ± 16	0	30 ± 5	84 ± 15	88 ± 16	1.4 ± 0.3

2.6.1. CO_2 consumption rates in the Southern Andes

The carbon export flux corresponds to the alkalinity flux resulting from silicate weathering (Figure 9). CO_2 consumption in CSVZ ranges from 0.4 to 5.7 x 10^6 mol/km^2/yr among the studied watersheds. After the Nilahue River (13), the rivers with the highest CO_2 consumption rates are Los Venados (14), associated with high runoff (> 2500 mm/yr) and its high volcanic cover (>80%); and Chico (20) with runoff >2000 mm/yr, a 54% of volcanic cover, and no hydrothermal influence. Runoff is the most important factor controlling CO_2 consumption rates in the Southern Andes (Figure 10). Whereas the correlation with other variables, such as lithology, or water transit time, is less apparent (Gaillardet et al., 1999). Considering all the area of CSVZ (78,617 km^2) the average weathering carbon export flux from studied watersheds is 0.11±0.01 x 10^{12} mol/yr. The total carbon export flux is equivalent to 0.0013 PgC/yr, is around 1% of the global export carbon silicate weathering on the continents (0.104-0.155 PgC/yr) (Suchet et al., 2003; Gaillardet et al., 1999; Zhang et al., 2021), being SVZ area the 0.1% of the total silicate rock cover in the world. These calculations are subject to considerable uncertainty including the CSVZ area, the presence of non-volcanic units, or the exclusion of other volcanic areas among the Southern Andes, thus, it should be regarded as first order calculation.
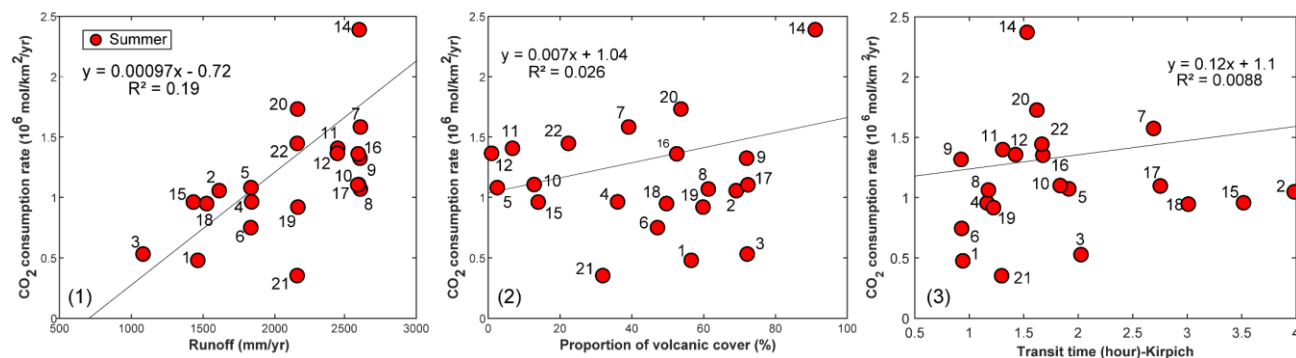
Figure 10: CO_2 consumption rate v/s different variables for each CSVZ River. (12.1) Runoff (mm/yr) with a historical register of 42 years. (12.2) Percentage of volcanic rock cover based on SERNAGEOMIN, 1987. (12.3) Approximate time of transit (hours) using Kirpich equation for each basin. Nilahue River (13) does not show in the figure due to the higher values compared to the other rivers (5.7±1.1 x 10^6 mol/km^2/yr). The black line shows linear regression for each of the data and its respective R^2.

Our initial assumption was that dissolved carbon originates from two sources: atmospheric and magmatic. Several authors emphasize the impact of shallow processes, such as

mixing between meteoric water infiltration and calcite precipitation, on the hydrothermal springs in SVZ (Tardani et al., 2016; Pérez Moreno et al., 2021; Sánchez-Alfaro et al., 2013). All of these studies analyzed the influence of magmatic gases in geothermal systems in the SVZ, concluding that assuming the determining the sources of CO_2 in groundwaters is not straightforward. We use the $\delta^{13}C$ composition of riverine DIC to estimate the magmatic CO_2 fluxes released through gas emanations (fumaroles and diffuse soil CO_2 emissions contributing to the chemical weathering. In different volcanic regions, it has been concluded that magmatic CO_2 fluxes have been underestimated, such as central Italy by Chiodini et al. (1999) and Frondini et al. (2008), the Mammoth Mountain area, USA, by Evans et al. (2002), Yellowstone area by Werner et al. (2000), Lesser Antilles region by Rive et al., (2013) and Aso caldera by Romero-Mujalli et al. (2022). We use a mass-balance equation to calculate the fraction of magmatic carbon (Eq. 11). This equation is sensitive to endmember variations. The error is mainly due to the wide range of magmatic $\delta^{13}C$ for the region, which also overlaps with atmospheric $\delta^{13}C$.

$$f_{mag} = \frac{\delta^{13}C_{riv} - \delta^{13}C_{soil}}{\delta^{13}C_{mag} - \delta^{13}C_{soil}} \qquad (11)$$

The f_{mag} is the fraction of carbon from magmatic reservoirs, the $\delta^{13}C_{riv}$ is the carbon isotopic composition of the river water, and $\delta^{13}C_{mag}$-$\delta^{13}C_{soil}$ correspond to the composition of endmember (Chiodini et al., 2000; Dietzel et al., 2009; Rivé et al., 2013; Romero-Mujalli et al., 2022; Yamada et al., 2011). The end-member compositions were selected from other studies in the zone (see discussion before in Figure 5). Biogenic CO_2, as represented by soil seeps, displays a wide $\delta^{13}C_{soil}$ range between –25 and –15‰, which reflects the more or less active processes that control the DIC in soil. The magmatic endmember, $\delta^{13}C_{mag}$, is defined with $\delta^{13}C$ data from hot springs reported by Pérez-Moreno et al. (2021) and Tardani et al. (2016), ranging from -7.45‰ to -9.75‰ with a mean of -8.6±1.2‰. The fractions are shown in Table 8 with their respective errors associated to the end-member uncertainties.

Table 8: The proportions of magmatic carbon (f_{mag}), isotope carbon data of rivers sampled in summer and magmatic CO2 consumption.

ID	$\delta^{13}C$ River	Magmatic CO$_2$ fraction	Magmatic CO$_2$ consumption
	‰	%	10^6 mol/km^2/yr
1	-9.13	[61-100]	0.4 ± 0.2
2	-7.63	[70-100]	1.0 ± 0.3
3	-7.67	[70-100]	0.5 ± 0.2
4	-9.31	[60-100]	0.8 ± 0.3
5	-7.15	[73-100]	1.0 ± 0.4
6	-1.43	100	1.0 ± 0.4
7	-8.40	[66-100]	1.4 ± 0.4
9	-8.30	[66-100]	1.2 ± 0.4
10	-4.77	[96-100]	1.3 ± 0.4
11	-6.90	[75-100]	1.4 ± 0.5
12	-7.29	[72-100]	1.3 ± 0.5
13	-4.49	[88-100]	6.7 ± 2.1
14	-7.10	[73-100]	2.3 ± 0.7
17	-9.23	[60-100]	0.9 ± 0.3

The discussion of variations in magmatic fractions poses challenges due to the limited data collected in this study. However, it suggests that the weathering rate in the region, driven by atmospheric CO$_2$ in soils, is considerably lower than the CO$_2$ from deep gas emission. The alkalinity fluxes from magmatic source varies between 0.4 ± 0.2 x 10^6 mol/km^2/yr and 6.7 ± 2.1 x 10^6 mol/km^2/yr, normalized by basin area. The magmatic fraction allows determining a mean magmatic CO$_2$ consumption rate of 1.2±0.4 x 10^6 mol/km^2/yr that extrapolated by total watershed area (8,330 km^2) result in 10±3 x 10^9 mol/yr , corresponding to 93±36% of carbon consumption flux in the region. The Critical Zone of active volcanic regions is not only governed by the chemical weathering reactions involving biosphere CO$_2$ in its upper part; it also experiences a substantial input of deep CO$_2$ from magmatic sources. Rivé et al. (2013) suggests that employing geophysical and geochemical methods to study hydrothermal systems would provide insights into other controlling factors affecting this process, such as soil saturation, structural influences, among others.

2.7. Conclusions

The 22 rivers studied in the Central Southern Volcanic Zone (CSVZ) (38°S-42°S) exhibit a calcium-magnesium bicarbonate chemical composition, with a neutral pH and a Ca+Mg vs. Na ratio suggesting drainage from silicate rocks. The excess of other acidic sources, such as H_2S or HCl, distinct from carbonic acid, motivates investigating their potential effect on chemical weathering rates. Hydrothermal systems in the CSVZ display considerable variability in their chemical compositions. In this study, we examined 16 of these systems, with average temperatures of 62°C and pH ranging from 8 to 9.2, characterizing them as chloride-sodium type waters.

To assess the contribution of these hydrothermal springs to the dissolved load in the SVZ catchments, we employed different chemical tracers that allowed us to identify and subsequently quantify this input. By combining Cl/B ratios, Ge/Si ratios, and boron and carbon isotopes ($\delta^{11}B$, $\delta^{13}C$), we consistently concluded that 14 out of the 22 studied rivers showed signs of hydrothermal influence. However, these tracers may have individual limitations due to biogeochemical processes, water transit times, and the age of weathered rocks. Subsequently, we used two different methods to quantify the fraction of solutes from hydrothermal sources. The two methods, the Cl-budget and the Ge/Si mass-balance, we found that the Cl-budget method underestimates the hydrothermal contribution in rivers where other sources of acid -such as sulfate- were important. On the other hand, the use of Ge/Si as a hydrothermal tracer was effective only in hot springs with high temperatures and high Ge concentrations. Thus, in several cases, Ge/Si ratios (<2 µmol/mol) led to underestimation of the hydrothermal contribution. Due to the inconsistent use of Ge/Si mass-balance as a hydrothermal tracer, we decided to report the hydrothermal inputs calculated with the Cl-budget method, except for one river (12) where sulfate is the main anion. We conclude that approximately 11% of the silicate export solutes in the rivers of the CSVZ originate from hydrothermal systems. The river with the least hydrothermal influence is the Blanco River at Curacautin, with a fraction of approximately 0.2%, while the greatest influence is observed in the Nilahue River, with 81%.

This study started with the hypothesis that solute fluxes exported from the basins in the Southern Andes are high and that silicate weathering processes in the region play a significant role in the global CO_2 cycle. The calculated chemical fluxes for the CSVZ are comparable to those of tropical volcanic islands and arcs (108-308 ton/ km²/yr), with an

average silicate export flux weighted area of 87 ton/km²/yr. The highest value is observed in the Nilahue River, with a rate of 386 ton/ km²/yr, possibly related to the volcanic context of the Cordón-Caulle Complex (Delgado, 2021; Galetto et al., 2023; Pistolesi et al., 2015). Extrapolating chemical fluxes from volcanic basins to the total extent of the CSVZ (78,617 km²), the carbon export flux is approximately 0.11×10^{12} mol/yr or 0.0013 PgC/yr. This is equivalent to around 1% of the global carbon consumption from silicate weathering on continents (0.104-0.155 PgC/yr; Gaillardet et al., 1999; Suchet et al., 2003; Zhang et al., 2021). Using $\delta^{13}C$ composition of the riverwaters, it was possible to estimate the primary source (soil or magmatic) of consumed CO_2. The results indicated that the acid source in weathering processes is primarily magmatic, with the atmospheric contribution in soils considerably lower. The magmatic fraction allows determining a mean magmatic CO_2 flux of $1.2\pm0.4 \times 10^6$ mol/km²/yr that normalized by total basin areas (8,330 km²) result in a total of $10\pm3 \times 10^9$ mol/yr, corresponding to $93\pm36\%$ of carbon flux in the region. This preliminary result reinforces the hypothesis that the control of chemical weathering fluxes in volcanic regions may be strongly linked to deep-CO_2 (Rivé et al., 2013; Romero-Mujalli et al., 2022; Zhong et al., 2023).

Acknowledgments

Chapter 3 : CONCLUSIONS

3.1. Scientific contributions of this dissertation

This study provides the first estimation of weathering rates from volcanic catchments in the Southern Andes. We measured during the dry and rainy season 22 rivers and 16 hot springs in Central South Volcanic Zone (CSVZ). Along with the chemistry of major elements, we analyzed boron and carbon isotopes, and we provide new documentation of germanium concentration in rivers and thermal springs. With a discharge register of 42 years, we could determine the continental weathering rates of Southern Andean volcanic arc and a first approximation of hydrothermal solutes input to streams. The chemical tracers used for detecting the thermal contribution (Cl, B, Ge, $\delta^{11}B$, $\delta^{13}C$) may be applicable to other rivers along to SVZ and enhance the comprehension of the biogeochemical cycle of these elements in volcanic provinces.

Using two different methods, we did a first estimation of hydrothermal chemical fluxes that affect the rivers in the region. We concluded that approximately 11% of the silicate solutes exported in the rivers of the CSVZ originate from hydrothermal systems. This work builds upon previous studies conducted in volcanic regions, where the hydrothermal system contributes significantly to the solute budget. Nevertheless, understanding the interaction between high and low-temperature systems remains challenging. This thesis project aims to offer new chemical insights that could contribute to improving our understanding in this area.

The Southern Volcanic Zone of the Andes is a region with high silicate weathering rates, with an average of 87 ton/ km²/yr. Los Venados and Nilahue Rivers stand out, with the highest are-normalized silicate export fluxes with 129 and 386 ton/km²/yr, respectively. These rivers drain the active region of Cordon-Caulle Volcanic Complex. In particular, the Nilahue River consistently exhibits an extreme hydrothermal influence, with a contribution of 81% in silicate solute flux. Although full compression of this hydrothermal system is limited by the data acquired in this work, the Nilahue River certainly emerges as a promising target for exploring the relation between the hydrothermal systems and the active volcanic processes.

Considering the total extension of the Central South Volcanic Zone (38°S-42°S) and extrapolating the atmospheric carbon flux, this is equivalent to 0.11 x 10^{12} mol/yr or 0.0013

PgC/yr. Taking account global carbon consumption from silicate weathering on the continents (0.104-0.155 PgC/yr; Gaillardet et al., 1999; Suchet et al., 2003; Zhang et al., 2021), Southern Andes contribute around 1% of that budget. This CO_2 consumed comes from magmatic source in a 93±36%. This preliminary result from use of ^{13}C isotope emphasizes the role of deep acid sources in volcanic regions and validates their relevance in chemical weathering processes. Certainly, this research emphasizes the importance of exploring interactions between low and high-temperature systems and deepening our understanding of the factors that intensify these (bio)geochemical processes.

3.2. Future work

These preliminary findings mark the initial steps in understanding surface processes and the potential impact of solute sources from volcanic basins on the Pacific Ocean in the Southern Andes. However, there are still unresolved issues that require further investigation. These include the dynamic of hydrothermal fluxes and refining the mixing model to determine better the sources of chemical solute fluxes in rivers and the variables that affect them.

In the context of this study, five fieldwork campaigns were realized. Although only three of them (February and July 2021, and January 2022 in the Cordon Caulle volcanic complex) are reported in this document, the remaining campaigns took place in March (summer) and July (winter) 2022. These additional data will be used to further understand the seasonal variability in dissolved solutes in the rivers, considering that 2021 was characterized as a dry year while 2022 saw an increase (~40%) in mean annual precipitation, as reported by the Chilean Water Directorate (**¡Error! La autoreferencia al marcador no es válida.**). Higher rainfall implied an average of 25% increase in discharge in 2022 for the sampled catchments. These scenarios allow us to assess the annual variability of solute fluxes and weathering rates. Most major ions show dissolution in winter by a factor from 1.1 to 4.6. On the other hand, Al and Fe show chemostatic behavior in some basins. Based on these data, we can assess the interannual variability of solute fluxes for the 2021–2022 volcanic basins. Silicate export rates during 2021 are 23-221 ton/km²/yr, and 24-157 ton/km²/yr during the wetter 2022 year. Preliminary results highlight the implications for the seasonal variability of solute fluxes in active volcanic zones and the potential change associated with decreased rainfall. On the other hand, it is possible, with strontium isotopic data ($^{87}Sr/^{86}Sr$) measured in samples from the year 2021, to determine the lithological origin of the solutes (intrusive or volcanic). Complementary to this, in the fieldwork in March, samples of river

sediments were taken, and that allowed us to understand erosion processes in these volcanic catchments. Finally, this research shows the anomalous chemical behavior of the Nilahue River compared to other rivers. The results suggest promoting the chemical analyses in that river system and the interaction with groundwater or magma reservoir of the Cordón-Caulle volcano complex.

Table 9: Examples of annual accumulated precipitation reported by the Chilean Water Directorate in four meteorological stations throughout the study area (38°–42°S) during the years 2021 and 2022.

Meteorological station	Location	Annual accumulated precipitation (2021)	Annual accumulated precipitation (2022)
		(mm)	(mm)
"Río Cautín en Rari-Ruca" (09123001)	38.4°S-72°O	1056.3	1287.5
"Río Truful en camino internacional" (09400000)	38.8°S-71.65°O	936.4	1316.5
"Río Tolten en Villarrica" (09420001)	39.3°S-72.3°O	1239.3	1757.9
"Lago Chapo" (10430005)	41.4°S-72.6°O	851.8	1669.6
"Malalcahuello" (091200039)	38.47°S-71.58°O	1369.6	1747.3
"Pucon" (09420002)	39.28°S-71.95°O	1401.1	1658.4

Bibliography

Adriasola, A. C., Thomson, S. N., Brix, M. R., Hervé, F., & Stöckhert, B. (2006). Postmagmatic cooling and late Cenozoic denudation of the North Patagonian Batholith in the Los Lagos region of Chile, 41°-42°15′S. *International Journal of Earth Sciences*, *95*(3), 504–528. https://doi.org/10.1007/s00531-005-0027-9

Aggarwal, J., Palmer, M., Bullen, T. D., Arnorsson, S., & Ragnarsdottir, K. (2000). The boron isotope systematics of Icelandic geothermal waters: 1. Meteoric water charged systems. *Geochimica et Cosmochimica Acta*, *64*(4), 579–585. https://www.sciencedirect.com/science/article/pii/S0016703799003002

Aguilar, G., Riquelme, R., Martinod, J., Darrozes, J., & Maire, E. (2011). Variability in erosion rates related to the state of landscape transience in the semi-arid Chilean Andes. *Earth Surface Processes and Landforms*, *36*(13), 1736–1748. https://doi.org/10.1002/esp.2194

Aguirre, A. A., Derry, L. A., Mills, T. J., & Anderson, S. P. (2017). Colloidal transport in the Gordon Gulch catchment of the Boulder Creek CZO and its effect on C-Q relationships for silicon. *Water Resources Research*, *53*(3), 2368–2383. https://doi.org/10.1002/2016WR019730

Aiuppa, A., Baker, D. R., & Webster, J. D. (2009). Halogens in volcanic systems. *Chemical Geology*, *263*(1–4), 1–18. https://doi.org/10.1016/j.chemgeo.2008.10.005

Alvarez-Garreton, C., Lara, A., Boisier, J. P., & Galleguillos, M. (2019). The impacts of native forests and forest plantations on water supply in Chile. *Forests*, *10*(6). https://doi.org/10.3390/f10060473

Alvarez-Garreton, C., Mendoza, P. A., Pablo Boisier, J., Addor, N., Galleguillos, M., Zambrano-Bigiarini, M., Lara, A., Puelma, C., Cortes, G., Garreaud, R., McPhee, J., & Ayala, A. (2018). The CAMELS-CL dataset: Catchment attributes and meteorology for large sample studies-Chile dataset. *Hydrology and Earth System Sciences*, *22*(11), 5817–5846. https://doi.org/10.5194/hess-22-5817-2018

Amiotte Suchet, P., Probst, J.-L., & Ludwig, W. (2003). Worldwide distribution of continental rock lithology: Implications for the atmospheric/soil CO_2 uptake by continental weathering and alkalinity river transport to the oceans . *Global Biogeochemical Cycles*, *17*(2), n/a-n/a. https://doi.org/10.1029/2002gb001891

Anders, A. M., Sletten, R. S., Derry, L. A., & Hallet, B. (2003). Germanium/silicon ratios in the Copper River Basin, Alaska: Weathering and partitioning in periglacial versus glacial

environments. *Journal of Geophysical Research: Earth Surface, 108*(F1), n/a-n/a. https://doi.org/10.1029/2003jf000026

Arancibia, G., Cembrano, J., & Lavenu, A. (1999). Transpresión dextral y partición de la deformación en la zona de falla liquiñe-ofqui, aisén, chile (44-45°S). *Revista Geologica de Chile, 26*(1), 3–22. https://doi.org/10.4067/S0716-02081999000100001

Arnórsson, S. (1984). Germanium in Icelandic geothermal systems. *Geochimica et Cosmochimica, 48,* 2489–2502.

Arnórsson, S. (1985). The Use of Mixing Models And Chemical Geothermometers For Estimating Underground Temperatures In Geothermal Systems. *Journal of Volcanology and Geothermal Research, 23,* 299–335.

Arnórsson, S., & Andrésdóttir, A. (1995). Processes controlling the distribution of boron and chlorine in natural waters in Iceland. *Geochimica et Cosmochimica Acta, 59*(20), 4125–4146.

Assayag, N., Rivé, K., Ader, M., Jézéquel, D., & Agrinier, P. (2006). Improved method for isotopic and quantitative analysis of dissolved inorganic carbon in natural water samples. *Rapid Communications in Mass Spectrometry, 20*(15), 2243–2251. https://doi.org/10.1002/RCM.2585

Balagizi, C. M., Darchambeau, F., Bouillon, S., Yalire, M. M., Lambert, T., & Borges, A. V. (2015). River geochemistry, chemical weathering, and atmospheric CO2 consumption rates in the Virunga Volcanic Province (East Africa). *Geohemistry, Geophysics, Geosystems, 16*(8), 2637–2660. https://doi.org/10.1002/2015GC005999

Bannister, J. R., Vidal, O. J., Teneb, E., & Sandoval, V. (2012). Latitudinal patterns and regionalization of plant diversity along a 4270-km gradient in continental Chile. *Austral Ecology, 37*(4), 500–509. https://doi.org/10.1111/j.1442-9993.2011.02312.x

Baronas, J. (2017). Germanium And Silicon Isotope Geochemistry In Terrestrial And Marine Low-Temperature Environments.

Baronas, J. J., Torres, M. A., West, A. J., Rouxel, O., Georg, B., Bouchez, J., Gaillardet, J., & Hammond, D. E. (2018). Ge and Si isotope signatures in rivers: A quantitative multi-proxy approach. *Earth and Planetary Science Letters, 503,* 194–215. https://doi.org/10.1016/j.epsl.2018.09.022

Baronas, J. J., West, A. J., Burton, K. W., Hammond, D. E., Opfergelt, S., Pogge von Strandmann, P. A. E., James, R. H., & Rouxel, O. J. (2020). Ge and Si Isotope Behavior During

Intense Tropical Weathering and Ecosystem Cycling. *Global Biogeochemical Cycles, 34*(8). https://doi.org/10.1029/2019GB006522

Benedetti, M. F., Menard, O., Noack, Y., Carvalho, A., & Nahon, D. (1994). Water-rock interactions in tropical catchments: field rates of weathering and biomass impact. *Chemical Geology, 118*(1–4). https://doi.org/10.1016/0009-2541(94)90177-5

Berner, R. A. (1992). Weathering, plants, and the long-term carbon cycle. In *Geochimi~ d Cosmochimica Acllr* (Vol. 56).

Berner, R. A., Lasaga, A. C., & Garrels, R. M. (1983). The carbonate-silicate geochemical cycle and its effect on atmospheric carbon dioxide over the past 100 million years. *American Journal of Science, 283*, 641–683.

Bernstein, L. R. (1985). *Germanium geochemistry and mineralogy* (Vol. 49).

Bluth, G. J. S., & Kump, L. R. (1994). Lithologic and climatologic controls of river chemistry. In *Geochimica et Cosmochimica Acta* (Vol. 58, Issue 10).

Boisier, J. P., Alvarez-Garreton, C., Cordero, R. R., Damiani, A., Gallardo, L., Garreaud, R. D., Lambert, F., Ramallo, C., Rojas, M., & Rondanelli, R. (2018). Anthropogenic drying in central-southern Chile evidenced by long-term observations and climate model simulations. *Elementa, 6.* https://doi.org/10.1525/elementa.328

Boisier, J. P., Rondanelli, R., Garreaud, R. D., & Muñoz, F. (2016). Anthropogenic and natural contributions to the Southeast Pacific precipitation decline and recent megadrought in central Chile. *Geophysical Research Letters, 43*(1), 413–421. https://doi.org/10.1002/2015GL067265

Brady, P. V. (1991). The effect of silicate weathering on global temperature and atmospheric CO2. *Journal of Geophysical Research, 96*(B11). https://doi.org/10.1029/91JB01898

Brady, P. V, Dorn, R. I., Brazel, A. J., Clark, J., Moore, R. B., & Glidewell, T. (1999). The effect of silicate weathering on global temperature and atmospheric CO2. *Geochimica et Cosmochimica, 63*, 19–20. https://agupubs.onlinelibrary.wiley.com/doi/abs/10.1029/91JB01898

Bravo-Linares, C., Schuller, P., Castillo, A., Salinas-Curinao, A., Ovando-Fuentealba, L., Muñoz-Arcos, E., Swales, A., Gibbs, M., & Dercon, G. (2020). Combining Isotopic Techniques to Assess Historical Sediment Delivery in a Forest Catchment in Central Chile. *Journal of Soil Science and Plant Nutrition, 20*(1), 83–94. https://doi.org/10.1007/s42729-019-00103-1

Burke, A., Present, T., Paris, G., Rae, E., Sandilands, B., Gaillardet, J., Peucker-Ehrenbrink, B., Fischer, W., McClelland, J., Spencer, R., Voss, B., & Adkins, J. (2018). Sulfur isotopes in rivers: Insights into global weathering budgets, pyrite oxidation, and the modern sulfur cycle. *Earth and Planetary Science*, *496*, 168–177. https://www.sciencedirect.com/science/article/pii/S0012821X18302991

Carey, A. E., Mendoza, J. A., Welch, K. A., Gardner, C. B., Goldsmith, S. T., & Lyons, W. B. (2015). Assessment of stream geochemistry in west central Nicaragua during baseflow conditions. *Applied Geochemistry*, *63*, 519–526. https://doi.org/10.1016/j.apgeochem.2015.03.013

Carretier, S., Tolorza, V., Regard, V., Aguilar, G., Bermúdez, M. A., Martinod, J., Guyot, J. L., Hérail, G., & Riquelme, R. (2018). Review of erosion dynamics along the major N-S climatic gradient in Chile and perspectives. *Geomorphology*, *300*, 45–68. https://doi.org/10.1016/J.GEOMORPH.2017.10.016

Carretier, S., Tolorza, V., Rodríguez, M. P., Pepin, E., Aguilar, G., Regard, V., Martinod, J., Riquelme, R., Bonnet, S., Brichau, S., Hérail, G., Pinto, L., Farías, M., Charrier, R., & Guyot, J. L. (2015). Erosion in the Chilean Andes between 27°S and 39°S: Tectonic, climatic and geomorphic control. *Geological Society Special Publication*, *399*, 401–418. https://doi.org/10.1144/SP399.16

Cembrano, J., Hervé, F., & Lavenu, A. (1996). The Liquifie Ofqui fault zone: a long-lived intra-arc fault system in southern Chile. *Tectonophysics*, *259*, 55–66.

Cembrano, J., & Lara, L. (2009). The link between volcanism and tectonics in the southern volcanic zone of the Chilean Andes: A review. *Tectonophysics*, *471*(1–2), 96–113. https://doi.org/10.1016/j.tecto.2009.02.038

Cembrano, J., Scherher, E., Lavenu, A., Herve, F., McClelland, B., Sergio, B., & Arancibia, G. (1996). NATURE AND TIMING OF CENOZOIC INTRA-ARC DEFORMATION, SOUTHERN CHILE. *Third ISAG, St Malo (France)*.

Cembrano, J., Schermer, E., Lavenu, A., & Sanhueza, A. (2000). Contrasting nature of deformation along an intra-arc shear zone, the Liquiñ e-Ofqui fault zone, southern Chilean Andes. In *Tectonophysics* (Vol. 319). www.elsevier.com/locate/tecto

Cerling, T. E. (1984). The stable isotopic composition of modern soil carbonate and its relationship to climate. In *Earth and Planetary Science Letters* (Vol. 71).

Cerling, T. E., Solomon, D. K., Quade, J., & Bowman, J. R. (1991). On the isotopic composition of carbon in soil carbon dioxide. *Geochrmrca Cr Cosmochimrca Acla*, *55*, 3403–3405.

Charrier, R., Pinto, L., & Rodríguez, M. P. (2007). Tectonostratigraphic evolution of the Andean Orogen in Chile. *Geological Society Special Publication*, 21–114. https://doi.org/10.1144/GOCH.3

Chetelat, B., & Gaillardet, J. (2005). Boron isotopes in the Seine River, France: a probe of anthropogenic contamination. *Enviromental Science Technology*, *39*(8), 2486–2493. https://doi.org/10.1021/es048387j

Chetelat, B., Gaillardet, J., Freydier, R., & Négrel, P. (2005). Boron isotopes in precipitation: Experimental constraints and field evidence from French Guiana. *Earth and Planetary Science Letters*, *235*(1–2), 16–30. https://doi.org/10.1016/j.epsl.2005.02.014

Chetelat, B., Liu, C., Gaillardet, J., Wang, Q., Zhao, Z., Lian, C., & Xiao, Y. (2009). Boron isotopes geochemistry of the Changjiang basin rivers. *Geochimica et Cosmochimica Acta*, *73*(20), 6084–6097. https://www.sciencedirect.com/science/article/pii/S0016703709004815

Chiodini, G., Caliro, S., Aiuppa, A., Avino, R., Granieri, D., Moretti, R., & Parello, F. (2011). First 13C/12C isotopic characterisation of volcanic plume CO2. *Bulletin of Volcanology*, *73*(5), 531–542. https://doi.org/10.1007/s00445-010-0423-2

Chiodini, G., Frondini, F., Cardellini, C., Parello, F., & Peruzzi, L. (2000). Rate of diffuse carbon dioxide Earth degassing estimated from carbon balance of regional aquifers: The case of central Apennine, Italy. *Journal of Geophysical Research: Solid Earth*, *105*(B4). https://doi.org/10.1029/1999jb900355

Cividini, D., Lemarchand, D., Chabaux, F., Boutin, R., & Pierret, M. C. (2010). From biological to lithological control of the B geochemical cycle in a forest watershed (Strengbach, Vosges). *Geochimica et Cosmochimica Acta*, *74*(11), 3143–3163. https://doi.org/10.1016/j.gca.2010.03.002

Clair, T., & Ehrman, J. (1998). Using neural networks to assess the influence of changing seasonal climates in modifying discharge, dissolved organic carbon, and nitrogen export in eastern Canadian rivers. *Water Resources Research*, *34*(3), 447–455. https://doi.org/10.1029/97WR03472

Clair, T., Ehrman, J., & Higuchi, K. (1999). Changes in freshwater carbon exports from Canadian terrestrial basins to lakes and estuaries under a 2×CO2 atmospheric scenario. *Global Biogeochemical Cycles*, *13*(4), 1091–1097. https://doi.org/10.1029/1999GB900055

Cullen, J. T., Hurwitz, S., Barnes, J. D., Lassiter, J. C., Penniston-Dorland, S., Meixner, A., Wilckens, F., Kasemann, S. A., & McCleskey, R. B. (2021). The Systematics of Chlorine,

Lithium, and Boron and δ37Cl, δ7Li, and δ11B in the Hydrothermal System of the Yellowstone Plateau Volcanic Field. *Geochemistry, Geophysics, Geosystems, 22*(4). https://doi.org/10.1029/2020GC009589

Daga, R., Ribeiro Guevara, S., Poire, D. G., & Arribére, M. (2014). Characterization of tephras dispersed by the recent eruptions of volcanoes Calbuco (1961), Chaitén (2008) and Cordón Caulle Complex (1960 and 2011), in Northern Patagonia. *Journal of South American Earth Sciences, 49*, 1–14. https://doi.org/10.1016/j.jsames.2013.10.006

Daniele, L., Taucare, M., Viguier, B., Arancibia, G., Aravena, D., Roquer, T., Sepúlveda, J., Molina, E., Delgado, A., Muñoz, M., & Morata, D. (2020). Exploring the shallow geothermal resources in the Chilean Southern Volcanic Zone: Insight from the Liquiñe thermal springs. *Journal of Geochemical Exploration, 218*. https://doi.org/10.1016/j.gexplo.2020.106611

De Argollo, R., & Schilling, J. G. (1978). GeSi and GaAl fractionation in Hawaiian volcanic rocks. *Geochimica et Cosmochimica Acta, 42*(6 PART A). https://doi.org/10.1016/0016-7037(78)90007-8

Delgado, F. (2021). Rhyolitic volcano dynamics in the Southern Andes: Contributions from 17 years of InSAR observations at Cordón Caulle volcano from 2003 to 2020. *Journal of South American Earth Sciences, 106*. https://doi.org/10.1016/j.jsames.2020.102841

Dellinger, M., Gaillardet, J., Bouchez, J., Calmels, D., Galy, V., Hilton, R., Louvat, P., & France-Lanord, C. (2014). Lithium isotopes in large rivers reveal the cannibalistic nature of modern continental weathering and erosion. *Earth and Planetary Science Letters, 401*, 359–372. https://www.sciencedirect.com/science/article/pii/S0012821X14003793

Derry, L. A., Kurtz, A. C., Ziegler, K., & Chadwick, O. A. (2005). Biological control of terrestrial silica cycling and export fluxes to watersheds. *Nature, 433*(7027), 728–731. https://doi.org/10.1038/nature03299

Dessert, C., Dupré, B., François, L., Schott, J., Gaillardet, J., Chakrapani, G., & Bajpai, S. (2001). Erosion of Deccan Traps determined by river geochemistry: impact on the global climate and the 87Sr/86Sr ratio of seawater. *Earth and Planetary Science Letters, 188*, 459–474. https://www.sciencedirect.com/science/article/pii/S0012821X0100317X

Dessert, C., Dupré, B., Gaillardet, J., François, L. M., & Allègre, C. J. (2003). Basalt weathering laws and the impact of basalt weathering on the global carbon cycle. *Chemical Geology, 202*(3–4), 257–273. https://doi.org/10.1016/j.chemgeo.2002.10.001

Dessert, C., Gaillardet, J., Dupre, B., Schott, J., & Pokrovsky, O. S. (2009). Fluxes of high-versus low-temperature water-rock interactions in aerial volcanic areas: Example from the Kamchatka Peninsula, Russia. *Geochimica et Cosmochimica Acta*, *73*(1), 148–169. https://doi.org/10.1016/j.gca.2008.09.012

Dessert, C., Lajeunesse, E., Lloret, E., Clergue, C., Crispi, O., Gorge, C., & Quidelleur, X. (2015). Controls on chemical weathering on a mountainous volcanic tropical island: Guadeloupe (French West Indies). *Geochimica et Cosmochimica Acta*, *171*, 216–237. https://doi.org/10.1016/j.gca.2015.09.009

Dietzel, M., Tang, J., Leis, A., & Köhler, S. J. (2009). Oxygen isotopic fractionation during inorganic calcite precipitation - Effects of temperature, precipitation rate and pH. *Chemical Geology*, *268*(1–2). https://doi.org/10.1016/j.chemgeo.2009.07.015

Dupré, B., Dessert, C., Oliva, P., Goddéris, Y., Viers, J., François, L., Millot, R., & Gaillardet, J. (2003). Rivers, chemical weathering and Earth's climate. In *Comptes Rendus - Geoscience* (Vol. 335, Issue 16, pp. 1141–1160). Elsevier Masson SAS. https://doi.org/10.1016/j.crte.2003.09.015

Eiriksdottir, E., Gislason, S., & Oelkers, E. (2015). Direct evidence of the feedback between climate and nutrient, major, and trace element transport to the oceans. *Geochimica et Cosmochimica Acta*, *166*, 249–266. https://www.sciencedirect.com/science/article/pii/S0016703715003889

Eiriksdottir, E. S., Gislason, S. R., & Oelkers, E. H. (2013). Does temperature or runoff control the feedback between chemical denudation and climate? Insights from NE Iceland. *Geochimica et Cosmochimica Acta*, *107*, 65–81. https://www.sciencedirect.com/science/article/pii/S0016703712007533

Eiriksdottir, E. S., Louvat, P., Gislason, S. R., Óskarsson, N., & Hardardóttir, J. (2008). Temporal variation of chemical and mechanical weathering in NE Iceland: Evaluation of a steady-state model of erosion. *Earth and Planetary Science Letters*, *272*(1–2), 78–88. https://doi.org/10.1016/j.epsl.2008.04.005

Elango, L., & Kannan, R. (2007). Chapter 11 Rock-water interaction and its control on chemical composition of groundwater. In *Developments in Environmental Science* (Vol. 5). https://doi.org/10.1016/S1474-8177(07)05011-5

Ellis, A. J., & Mahon, W. A. J. (1964). *Natural hydrothermal systems and experimental hot-water/rock interactions* (Vol. 28). Pergamon Press Ltd.

Ellis, A., & Mahon, W. (1967). Natural hydrothermal systems and experimental hot water/rock interactions (Part II)*. *Geochimica et Cosmochimica, 31*, 519–538.

Escoube, R., Rouxel, O. J., Edwards, K., Glazer, B., & Donard, O. F. X. (2015). Coupled Ge/Si and Ge isotope ratios as geochemical tracers of seafloor hydrothermal systems: Case studies at Loihi Seamount and East Pacific Rise 9°50′N. *Geochimica et Cosmochimica Acta, 167*, 93–112. https://doi.org/10.1016/J.GCA.2015.06.025

Evans, M. J., Deny, L. A., & France-Lanord, C. (2004). Geothermal fluxes of alkalinity in the Narayani river system of central Nepal. *Geochemistry, Geophysics, Geosystems, 5*(8). https://doi.org/10.1029/2004GC000719

Evans, M. J., & Derry, L. A. (2002). Quartz control of high germanium/silicon ratios in geothermal waters. In *Geology* (Issue 11). www.geosociety.org/pubs/

Evans, W. C., Sorey, M. L., Cook, A. C., Kennedy, B. M., Shuster, D. L., Colvard, E. M., White, L. D., & Huebner, M. A. (2002). Tracing and quantifying magmatic carbon discharge in cold groundwaters: lessons learned from Mammoth Mountain, USA. In *Journal of Volcanology and Geothermal Research* (Vol. 114). www.elsevier.com/locate/jvolgeores

Ewart, A. (1976). Mineralogy and chemistry of modern orogenic lavas — some statistics and implications. *Earth and Planetary Science Letters, 31*(3), 417–432. https://doi.org/10.1016/0012-821X(76)90124-2

Fernandez, N. M., Bouchez, J., Derry, L. A., Chorover, J., Gaillardet, J., Giesbrecht, I., Fries, D., & Druhan, J. L. (2022). Resiliency of Silica Export Signatures When Low Order Streams Are Subject to Storm Events. *Journal of Geophysical Research: Biogeosciences, 127*(5). https://doi.org/10.1029/2021JG006660

Fernandez, N. M., Perez-Fodich, A., Derry, L. A., & Druhan, J. L. (2021). A first look at Ge/Si partitioning during amorphous silica precipitation: Implications for Ge/Si as a tracer of fluid-silicate interactions. *Geochimica et Cosmochimica Acta, 297*, 158–178. https://doi.org/10.1016/j.gca.2021.01.007

Fournier, R. O. (1977). *CHEMICAL GEOTHERMOMETERS AND MIXING MODELS FOR GEOTHERMAL SYSTEMS* (Vol. 5). Pergamon Press.

France-Lanord, C., & Derry, L. A. (1997). Organic carbon burial forcing of the carbon cycle from Himalayan erosion. *Nature, 390*, 65–67. https://www.nature.com/articles/36324

Francois, L. M., & Walker, J. C. G. (1992). Modelling the phanerozic carbon cycle and climate: constraints from the 87Sr/86Sr isotopic ratio of seawater. *America Journal of Science*, *292*, 81–135.

Froelich, P. N., Blanc, V., Mortlock, R. A., Chillrud, S. N., Dunstan, W., Udomkit, A., & Peng, T. H. (1992). River Fluxes of Dissolved Silica to the Ocean Were Higher during Glacials: Ge/Si In Diatoms, Rivers, and Oceans. *Paleoceanography*, *7*(6), 739–767. https://doi.org/10.1029/92PA02090

Froelich, P. N., Hambrick, G. A., Andreae, M. O., Mortlock, R. A., & Edmond, J. M. (1985). GEOCHEMISTRY OF INORGANIC GERMANIUM IN NATURAL WATERS. *Journal of Geophysical Research*, *90*(C1), 1133–1141. https://doi.org/10.1029/JC090iC01p01133

Frondini, F., Caliro, S., Cardellini, C., Chiodini, G., Morgantini, N., & Parello, F. (2008). Carbon dioxide degassing from Tuscany and Northern Latium (Italy). *Global and Planetary Change*, *61*(1–2), 89–102. https://doi.org/10.1016/j.gloplacha.2007.08.009

Gaillardet, J., Dupre, B., Louvat, P., & Allegre, C. J. (1999). Global silicate weathering and CO consumption rates deduced 2 from the chemistry of large rivers. In *Chemical Geology* (Vol. 159).

Gaillardet, J., & Lemarchand, D. (2018). Boron in the weathering environment. In *Advances in Isotope Geochemistry* (pp. 163–188). Springer. https://doi.org/10.1007/978-3-319-64666-4_7

Gaillardet, J., Louvat, P., & Lajeunesse, E. (2011a). Rivers from Volcanic Island Arcs: The subduction weathering factory. *Applied Geochemistry*, *26*(SUPPL.). https://doi.org/10.1016/j.apgeochem.2011.03.057

Gaillardet, J., Rad, S., Rivé, K., Louvat, P., Gorge, C., Allègre, C. J., & Lajeunesse, E. (2011b). Orography-driven chemical denudation in the lesser antilles: Evidence for a new feed-back mechanism stabilizing atmospheric CO 2. *American Journal of Science*, *311*(10), 851–894. https://doi.org/10.2475/10.2011.02

Galetto, F., Pritchard, M. E., Hornby, A. J., Gazel, E., & Mahowald, N. M. (2023). Spatial and Temporal Quantification of Subaerial Volcanism From 1980 to 2019: Solid Products, Masses, and Average Eruptive Rates. *Reviews of Geophysics*, *61*(1). https://doi.org/10.1029/2022RG000783

Garreaud, R. D., Alvarez-Garreton, C., Barichivich, J., Pablo Boisier, J., Christie, D., Galleguillos, M., LeQuesne, C., McPhee, J., & Zambrano-Bigiarini, M. (2017). The 2010-2015 megadrought in central Chile: Impacts on regional hydroclimate and vegetation. *Hydrology*

and *Earth System Sciences*, *21*(12), 6307–6327. https://doi.org/10.5194/HESS-21-6307-2017

Garrels, R., & Mackenzie, F. (1971). Gregor's denudation of the continents. *Nature, 231*, 382–383. https://www.nature.com/articles/231382a0

Gaspard, F., Opfergelt, S., Dessert, C., Robert, V., Ameijeiras-Mariño, Y., & Delmelle, P. (2021a). Imprint of chemical weathering and hydrothermalism on the Ge/Si ratio and Si isotope composition of rivers in a volcanic tropical island, Basse-Terre, Guadeloupe (French West Indies). *Chemical Geology, 577*. https://doi.org/10.1016/j.chemgeo.2021.120283

Gaspard, F., Opfergelt, S., Hirst, C., Hurwitz, S., McCleskey, R. B., Zahajská, P., Conley, D. J., & Delmelle, P. (2021b). Quantifying Non-Thermal Silicate Weathering Using Ge/Si and Si Isotopes in Rivers Draining the Yellowstone Plateau Volcanic Field, USA. *Geochemistry, Geophysics, Geosystems, 22*(11). https://doi.org/10.1029/2021GC009904

Genereux, D. P., Webb, M., & Kip Solomon, D. (2009). Chemical and isotopic signature of old groundwater and magmatic solutes in a Costa Rican rain forest: Evidence from carbon, helium, and chlorine. *Water Resources Research, 45*(8). https://doi.org/10.1029/2008WR007630

Gerlach, D. C., Frey, F. A., Moreno-roa, H., & Lopez-escobar, L. (1988). Recent Volcanism in the Puyehue—Cordon Caulle Region, Southern Andes, Chile (40·5°S): Petrogenesis of Evolved Lavas. *Journal of Petrology, 29*(2), 333–382. https://doi.org/10.1093/PETROLOGY/29.2.333

Giggenbach, W. F. (1988). *Geothermal solute equilibria. Derivation of Na-K-Mg-Ca geoindicators* (Vol. 52).

Giggenbach, W. F., Gonfiantini, R., Jangi, B. L., & Truesdell, A. H. (1983). Isotopic and chemical composition of parbati valley geothermal discharges, North-West Himalaya, India. *Geothermics, 12*(2–3), 199–222. https://doi.org/10.1016/0375-6505(83)90030-5

Gíslason, S. R., Arnórsson, S., & Ármannsson, H. (1996). Chemical weathering of basalt in Southwest Iceland; effects of runoff, age of rocks and vegetative/glacial cover. *American Journal of Science, 296*(8), 837–907. https://doi.org/10.2475/AJS.296.8.837

Gislason, S. R., Oelkers, E. H., Eiriksdottir, E. S., Kardjilov, M. I., Gisladottir, G., Sigfusson, B., Snorrason, A., Elefsen, S., Hardardottir, J., Torssander, P., & Oskarsson, N. (2009). Direct evidence of the feedback between climate and weathering. *Earth and Planetary Science Letters, 277*(1–2), 213–222. https://doi.org/10.1016/j.epsl.2008.10.018

Glodny, J., Echtler, H., Collao, S., Ardiles, M., Burón, P., & Figueroa, O. (2008). Differential Late Paleozoic active margin evolution in South-Central Chile (37°S–40°S) – the Lanalhue Fault Zone. *Journal of South American Earth Sciences*, *26*(4), 397–411. https://doi.org/10.1016/J.JSAMES.2008.06.001

Goddéris, Y., Donnadieu, Y., Carretier, S., Aretz, M., Dera, G., MacOuin, M., & Regard, V. (2017). Onset and ending of the late Palaeozoic ice age triggered by tectonically paced rock weathering. *Nature Geoscience*, *10*(5), 382–386. https://doi.org/10.1038/ngeo2931

Godsey, S. E., Kirchner, J. W., & Clow, D. W. (2009). Concentration-discharge relationships reflect chemostatic characteristics of US catchments. *Hydrological Processes*, *23*(13), 1844–1864. https://doi.org/10.1002/hyp.7315

Goldberg, S., & Glaubig, R. A. (1985). Boron Adsorption on Aluminum and Iron Oxide Minerals. *Soil Science Society of America Journal*, *49*(6), 1374–1379. https://doi.org/10.2136/SSSAJ1985.03615995004900060009X

Goldsmith, S. T., Carey, A. E., Johnson, B. M., Welch, S. A., Lyons, W. B., McDowell, W. H., & Pigott, J. S. (2010). Stream geochemistry, chemical weathering and CO2 consumption potential of andesitic terrains, Dominica, Lesser Antilles. *Geochimica et Cosmochimica Acta*, *74*(1), 85–103. https://doi.org/10.1016/j.gca.2009.10.009

Goldsmith, S. T., Carey, A. E., Lyons, W. B., & Hicks, D. M. (2008). Geochemical fluxes and weathering of volcanic terrains on high standing islands: Taranaki and Manawatu-Wanganui regions of New Zealand. *Geochimica et Cosmochimica Acta*, *72*(9), 2248–2267. https://doi.org/10.1016/j.gca.2007.12.024

González, M. E., Gómez-González, S., Lara, A., Garreaud, R., & Díaz-Hormazábal, I. (2018). The 2010–2015 Megadrought and its influence on the fire regime in central and south-central Chile. *Ecosphere*, *9*(8), e02300. https://doi.org/10.1002/ECS2.2300

Grard, A., Francois, L., Dessert, C., Dupré, B., & Godderis, Y. (2005). Basaltic volcanism and mass extinction at the Permo-Triassic boundary: environmental impact and modeling of the global carbon cycle. *Earth and Planetary Science Letters*, *234*, 107–221. https://www.sciencedirect.com/science/article/pii/S0012821X05001433

Han, Y., Huh, Y., & Derry, L. (2015). Ge/Si ratios indicating hydrothermal and sulfide weathering input to rivers of the Eastern Tibetan Plateau and Mt. Baekdu. *Chemical Geology*, *410*, 40–52. https://doi.org/10.1016/j.chemgeo.2015.06.001

Harder, H. (1970). *BORON CONTENT OF SEDIMENTS AS A TOOL IN FACIES ANALYSIS*.

Harmon, R. S., Wörner, G., Goldsmith, S. T., Harmon, B. A., Gardner, C. B., Berry Lyons, W., Ogden, F. L., Pribil, M. J., Long, D. T., Kern, Z., & Fórizs, I. (2016). Linking silicate weathering to riverine geochemistry-A case study from a mountainous tropical setting in west-central Panama. *Bulletin of the Geological Society of America*, *128*(11–12), 1780–1812. https://doi.org/10.1130/B31388.1

Harrison, J. A., Caraco, N., & Seitzinger, S. P. (2005). Global patterns and sources of dissolved organic matter export to the coastal zone: Results from a spatially explicit, global model. *Global Biogeochemical Cycles*, *19*(4). https://doi.org/10.1029/2005GB002480

Hartmann, J. (2009). Bicarbonate-fluxes and CO2-consumption by chemical weathering on the Japanese Archipelago - Application of a multi-lithological model framework. *Chemical Geology*, *265*(3–4), 237–271. https://doi.org/10.1016/j.chemgeo.2009.03.024

Hartmann, J., Jansen, N., Dürr, H. H., Harashima, A., Okubo, K., & Kempe, S. (2010). Predicting riverine dissolved silica fluxes to coastal zones from a hyperactive region and analysis of their first-order controls. *International Journal of Earth Sciences*, *99*(1), 207–230. https://doi.org/10.1007/s00531-008-0381-5

Hartmann, J., & Moosdorf, N. (2012). The new global lithological map database GLiM: A representation of rock properties at the Earth surface. *Geochemistry, Geophysics, Geosystems*, *13*(12). https://doi.org/10.1029/2012GC004370

Hauser, A. Y. (1997). Catrastro y caracterización de las fuentes de aguas minerales y termales de Chile. *Servicio Nacional de Geología y Minería-Chile*, *50*, 89.

He, D., Lee, C. T. A., Yu, X., & Farner, M. (2019). Ge/Si Partitioning in Igneous Systems: Constraints From Laser Ablation ICP-MS Measurements on Natural Samples. *Geochemistry, Geophysics, Geosystems*, *20*(10), 4472–4486. https://doi.org/10.1029/2019GC008514

Held, S., Schill, E., Schneider, J., Nitschke, F., Morata, D., Neumann, T., & Kohl, T. (2018a). Geochemical characterization of the geothermal system at Villarrica volcano, Southern Chile; Part 1: Impacts of lithology on the geothermal reservoir. *Geothermics*, *74*, 226–239. https://doi.org/10.1016/j.geothermics.2018.03.004

Held, S., Schill, E., Schneider, J., Nitschke, F., Morata, D., Neumann, T., & Kohl, T. (2018b). Geochemical characterization of the geothermal system at Villarrica volcano, Southern Chile; Part 1: Impacts of lithology on the geothermal reservoir. *Geothermics*, *74*, 226–239. https://doi.org/10.1016/j.geothermics.2018.03.004

Hem, J. (1948). Fluctuations in concentration of dissolved solids of some southwestern streams. *Eos, Transactions American Geophysical Union*, *29*(1), 80–84. https://doi.org/10.1029/TR029I001P00080

Hem, J. (1985). *Study and interpretation of the chemical characteristics of natural water.*

Henchiri, S., Clergue, C., Dellinger, M., Gaillardet, J., Louvat, P., & Bouchez, J. (2014). The Influence of Hydrothermal Activity on the Li Isotopic Signature of Rivers Draining Volcanic Areas. *Procedia Earth and Planetary Science*, *10*, 223–230. https://doi.org/10.1016/j.proeps.2014.08.026

Hervé, F., Pankhurst, R. J., Drake, R., Beck, M. E., & Mpodozis, C. (1993). Granite generation and rapid unroofing related to strike-slip faulting, Aysén, Chile. *Earth and Planetary Science Letters*, *120*(3–4), 375–386. https://doi.org/10.1016/0012-821X(93)90251-4

Hickey, R. L., Gerlach, D. C., & Frey, F. A. (1984). Geochemical Variations in Volcanic Rocks from Central-south Chile (33-42°S). *Andean Magmatism: Chemical and Isotopic Constraints*, 72–95.

Hickey-Vargas, R., Holbik, S., Tormey, D., Frey, F. A., & Moreno Roa, H. (2016). Basaltic rocks from the Andean Southern Volcanic Zone: Insights from the comparison of along-strike and small-scale geochemical variations and their sources. In *Lithos* (Vols. 258–259, pp. 115–132). Elsevier B.V. https://doi.org/10.1016/j.lithos.2016.04.014

Hilton, D., McMurty, G., & Goff, F. (1998). Largevariations in vent fluid CO2/3He ratios signal rapid changes in magma chemistry at Loihi seamount,Hawaii. *Nature, 396*.

Horton, T. W., Chamberlain, C. P., Fantle, M., & Blum, J. D. (1999). Chemical weathering and lithologic controls of water chemistry in a high-elevation river system: Clark's Fork of the Yellowstone river, Wyoming and Montana. *Water Resources Research*, *35*(5), 1643–1655. https://doi.org/10.1029/1998WR900103

Hrachowitz, M., Savenije, H. H. G., Blöschl, G., McDonnell, J. J., Sivapalan, M., Pomeroy, J. W., Arheimer, B., Blume, T., Clark, M. P., Ehret, U., Fenicia, F., Freer, J. E., Gelfan, A., Gupta, H. V., Hughes, D. A., Hut, R. W., Montanari, A., Pande, S., Tetzlaff, D., … Cudennec, C. (2013). A decade of Predictions in Ungauged Basins (PUB)—a review. *Https://Doi.Org/10.1080/02626667.2013.803183*, *58*(6), 1198–1255. https://doi.org/10.1080/02626667.2013.803183

Hurwitz, S., Evans, W. C., & Lowenstern, J. B. (2010). River solute fluxes reflecting active hydrothermal chemical weathering of the Yellowstone Plateau Volcanic Field, USA. *Chemical Geology*, *276*(3–4), 331–343. https://doi.org/10.1016/j.chemgeo.2010.07.001

Ibarra, D. E., Caves, J. K., Moon, S., Thomas, D. L., Hartmann, J., Chamberlain, C. P., & Maher, K. (2016). Differential weathering of basaltic and granitic catchments from concentration–discharge relationships. *Geochimica et Cosmochimica Acta*, *190*, 265–293. https://doi.org/10.1016/j.gca.2016.07.006

Ide, K., Hosono, T., Hossain, S., & Shimada, J. (2018). Estimating silicate weathering timescales from geochemical modeling and spring water residence time in the Kirishima volcanic area, southern Japan. *Chemical Geology*, *488*, 44–55. https://doi.org/10.1016/j.chemgeo.2018.04.009

Jacques, G., Hoernle, K., Gill, J., Wehrmann, H., Bindeman, I., & Lara, L. E. (2014). Geochemical variations in the Central Southern Volcanic Zone, Chile (38-43°S): The role of fluids in generating arc magmas. *Chemical Geology*, *371*, 27–45. https://doi.org/10.1016/j.chemgeo.2014.01.015

Jiang, P., Yu, G., Zhang, Q., Zou, Y., Tang, Q., Kang, Z., Sytharith, P., & Xiao, H. (2020). Chemical weathering and CO2 consumption rates of rocks in the Bishuiyan subterranean basin of Guangxi, China. *Scientific Reports*, *10*(1). https://doi.org/10.1038/s41598-020-68572-4

Johnson, N. M., Likens, G. E., Bormann, F. H., Fisher, D. W., & Pierce, R. S. (1969). A Working Model for the Variation in Stream Water Chemistry at the Hubbard Brook Experimental Forest, New Hampshire. *Water Resources Research*, *5*(6), 1353–1363. https://doi.org/10.1029/WR005I006P01353

Jones, M. T., Hembury, D. J., Palmer, M. R., Tonge, B., Darling, W. G., & Loughlin, S. C. (2011). The weathering and element fluxes from active volcanoes to the oceans: A Montserrat case study. *Bulletin of Volcanology*, *73*(3), 207–222. https://doi.org/10.1007/s00445-010-0397-0

Kardjilov, M., Gíslason, S., Geochemical, G. G.-J. of, & 2006, undefined. (2006). The effect of gross primary production, net primary production and net ecosystem exchange on the carbon fixation by chemical weathering of basalt in. *Journal of Geochemical Exploration*, *88*, 292–295. https://www.sciencedirect.com/science/article/pii/S0375674205001548?casa_token=kRR6aMivnnAAAAAA:JLKqVLW02Z0gusgGYVSKrBDAuGHZFNzF-ScnTOak-NeuSu2bQ6Ex_VwzLWOLOC9g5_H2ochB9jg

Kemeny, P. C., & Torres, M. A. (2021). Presentation and applications of mixing elements and dissolved isotopes in rivers (MEANDIR), a customizable MATLAB model for Monte Carlo inversion of dissolved river chemistry. *American Journal of Science*, *321*(5), 579–642. https://doi.org/10.2475/05.2021.03

Klaes, B., Wörner, G., Thiele-Bruhn, S., Arz, H. W., Struck, J., Dellwig, O., Groschopf, N., Lorenz, M., Wagner, J. F., Urrea, O. B., Lamy, F., & Kilian, R. (2022). Element mobility related to rock weathering and soil formation at the westward side of the southernmost Patagonian Andes. *Science of The Total Environment*, *817*, 152977. https://doi.org/10.1016/J.SCITOTENV.2022.152977

Krásný, J. rí, & Sharp, J. M. (2007). Groundwater in fractured rocks : selected papers from the Groundwater in Fractured Rocks International Conference, Prague, 2003. In *International Association of Hydrogeologists selected papers* (Issue 9).

Krone, L. V., Hampl, F. J., Schwerdhelm, C., Bryce, C., Ganzert, L., Kitte, A., Übernickel, K., Dielforder, A., Aldaz, S., Oses-Pedraza, R., Perez, J. P. H., Sanchez-Alfaro, P., Wagner, D., Weckmann, U., & von Blanckenburg, F. (2021). Deep weathering in the semi-arid Coastal Cordillera, Chile. *Scientific Reports*, *11*(1). https://doi.org/10.1038/s41598-021-90267-7

Kump, L. R., Brantley, S. L., & Arthur, M. A. (2000). CHEMICAL WEATHERING, ATMOS-PHERIC CO 2 , AND CLIMATE. In *Annu. Rev. Earth Planet. Sci* (Vol. 28). www.annualreviews.org

Kurtz, A. C., Derry, L. A., & Chadwick, O. A. (2002). *Germanium-silicon fractionation in the weathering environment.*

Kurtz, A. C., Lugolobi, F., & Salvucci, G. (2011). Germanium-silicon as a flow path tracer: Application to the Rio Icacos watershed. *Water Resources Research*, *47*(6). https://doi.org/10.1029/2010WR009853

Lange, D., Cembrano, J., Rietbrock, A., Haberland, C., Dahm, T., & Bataille, K. (2008). First seismic record for intra-arc strike-slip tectonics along the Liquiñe-Ofqui fault zone at the obliquely convergent plate margin of the southern Andes. *Tectonophysics*, *455*(1–4), 14–24. https://doi.org/10.1016/J.TECTO.2008.04.014

Lara, L. E., Lavenu, A., Cembrano, J., & Rodríguez, C. (2006). Structural controls of volcanism in transversal chains: Resheared faults and neotectonics in the Cordón Caulle-Puyehue area (40.5°S), Southern Andes. *Journal of Volcanology and Geothermal Research*, *158*(1–2), 70–86. https://doi.org/10.1016/j.jvolgeores.2006.04.017

Lara, L. E., Naranjo, J. A., & Moreno, H. (2004). Lanín volcano (39.5 S), Southern Andes: geology and morphostructural evolution. *Revista Geológica de Chile*, *31*, 241–257. https://www.scielo.cl/scielo.php?pid=S0716-02082004000200004&script=sci_arttext&tlng=en

Lee, B., Han, Y., Huh, Y., Lundstrom, C., Siame, L. L., Lee, J. I., & Park, B. K. (2013). Chemical and physical weathering in south Patagonian rivers: A combined Sr-U-Be isotope approach. *Geochimica et Cosmochimica Acta*, *101*, 173–190. https://doi.org/10.1016/j.gca.2012.09.054

Lemarchand, D., & Gaillardet, J. (2006). Transient features of the erosion of shales in the Mackenzie basin (Canada), evidences from boron isotopes. *Earth and Planetary Science Letters*, *245*(1–2), 174–189. https://doi.org/10.1016/j.epsl.2006.01.056

Lemarchand, D., Gaillardet, J., Lewin, E., & Allegre, C. (2002). Boron isotope systematics in large rivers: implications for the marine boron budget and paleo-pH reconstruction over the Cenozoic. *Chemical Geology*, *190*, 123–140. https://www.sciencedirect.com/science/article/pii/S0009254102001146

Lemarchand, E., Schott, J., & Gaillardet, J. (2005). Boron isotopic fractionation related to boron sorption on humic acid and the structure of surface complexes formed. *Geochimica et Cosmochimica Acta*, *69*(14), 3519–3533. https://doi.org/10.1016/J.GCA.2005.02.024

Lemarchand, E., Schott, J., & Gaillardet, J. (2007). How surface complexes impact boron isotope fractionation: Evidence from Fe and Mn oxides sorption experiments. *Earth and Planetary Science Letters*, *260*(1–2), 277–296. https://doi.org/10.1016/J.EPSL.2007.05.039

Lerman, A., & Wu, L. (2008). Kinetics of global geochemical cycles. In *Kinetics of Water-Rock Interaction*. https://doi.org/10.1007/978-0-387-73563-4_13

Lieber, & Pliscoff. (2006). *Sinopsis bioclimática y vegetacional de Chile*. https://books.google.cl/books?hl=es&lr=&id=Q6TQdlb6bEwC&oi=fnd&pg=PA167&ots=i5Fpn-YEo10&sig=Z75jUj--NQScQ0-f6mIbdRrJna0&redir_esc=y#v=onepage&q&f=false

Lodes, E., Scherler, D., Van Dongen, R., & Wittmann, H. (2023). The story of a summit nucleus: hillslope boulders and their effect on erosional patterns and landscape morphology in the Chilean Coastal Cordillera. *Earth Surface Dynamics*, *11*(2), 305–324. https://doi.org/10.5194/esurf-11-305-2023

López-Escobar, L. (1984). Petrology and chemistry of volcanic rocks of the southern Andes. *Andean Magmatism: Chemical and Isotopic Constraints*, 47–71. https://doi.org/10.1007/978-1-4684-7335-3_5/COVER

López-Escobar, L. (1985). Petrology and Chemistry of Volcanic Rocks of the Southern Andes. *Andean Magmatism: Chemical and Isotopic Constraints* , 47–71.

López-Escobar, L., Frey, F. A., & Vergara, M. (1977). Andesites and High-Alumina Basalts from the Central-South Chile High Andes: Geochemical Evidence Bearing on Their Petrogenesis. In *Contrib. Mineral. Petrol* (Vol. 63).

Louvat, P., & Allegre, C. J. (1997). Present denudation rates on the island of Réunion determined by river geochemistry: Basalt weathering and mass budget between chemical and mechanical erosions. *Geochimica et Cosmochimica Acta, 61*(17), 3645–3669.

Louvat, P., & Allegre, C. J. (1998). Riverine erosion rates on Sao Miguel volcanic island, Azores archipelago. *Chemical Geology, 148*, 177–200.

Louvat, P., Gaillardet, J., Paris, G., & Dessert, C. (2011). Boron isotope ratios of surface waters in Guadeloupe, Lesser Antilles. *Applied Geochemistry, 26*(SUPPL.). https://doi.org/10.1016/j.apgeochem.2011.03.035

Louvat, P., Gayer, E., & Gaillardet, J. (2014). Boron Behavior in the Rivers of Réunion Island, Inferred from Boron Isotope Ratios and Concentrations of Major and Trace Elements. *Procedia Earth and Planetary Science, 10*, 231–237. https://doi.org/10.1016/j.proeps.2014.08.029

Louvat, P., Gislason, S. R., & Allègre, C. J. (2008). Chemical and mechanical erosion rates in Iceland as deduced from river dissolved and solid material. *American Journal of Science, 308*(5), 679–726. https://doi.org/10.2475/05.2008.02

Lugolobi, F., Kurtz, A. C., & Derry, L. A. (2010). Germanium-silicon fractionation in a tropical, granitic weathering environment. *Geochimica et Cosmochimica Acta, 74*(4), 1294–1308. https://doi.org/10.1016/j.gca.2009.11.027

Marschall, H., & Foster, G. (2018). *Boron Isotope, the Fifth Element.* http://www.springer.com/series/8152

Marschall, H. R., & Jiang, S. Y. (2011). Tourmaline Isotopes: No Element Left Behind. *Elements, 7*(5), 313–319. https://doi.org/10.2113/GSELEMENTS.7.5.313

Marschall, H. R., Wanless, V. D., Shimizu, N., Pogge von Strandmann, P. A. E., Elliott, T., & Monteleone, B. D. (2017). The boron and lithium isotopic composition of mid-ocean ridge basalts and the mantle. *Geochimica et Cosmochimica Acta, 207*, 102–138. https://doi.org/10.1016/J.GCA.2017.03.028

Mattsson, T., Kortelainen, P., & Raike, A. (2005). Export of DOM from boreal catchments: impacts of land use cover and climate. *Biogeochemistry, 76*(2), 373–394. https://doi.org/10.1007/s10533-005-6897-x

Meek, K., Derry, L., Sparks, J., & Cathles, L. (2016). 87Sr/86Sr, Ca/Sr, and Ge/Si ratios as tracers of solute sources and biogeochemical cycling at a temperate forested shale catchment, central Pennsylvania, USA. *Chemical Geology*, *445*, 84–102. https://doi.org/10.1016/J.CHEMGEO.2016.04.026

Melnick, D., Folguera, A., & Ramos, V. A. (2006). Structural control on arc volcanism: The Caviahue–Copahue complex, Central to Patagonian Andes transition (38°S). *Journal of South American Earth Sciences*, *22*(1–2), 66–88. https://doi.org/10.1016/J.JSAMES.2006.08.008

Mendoza, P., Muñoz-Castro, E., Vásquez, N., Lagos, M. A., & Vargas, X. (2021). PRINCIPIOS DARWINIANOS APLICADOS AL BALANCE HÍDRICO DE CHILE. In *Rutas Hidrológicas: Recordando a un colega por los senderos de la Hidrología* (pp. 7–18).

Meybeck, M. (1987). Global chemical weathering of surficial rocks estimated from river dissolved loads. *American Journal of Science*, *287*, 401–428.

Millot, R., Gaillardet, J., Dupré, B., & Allegre, C. J. (2002). The global control of silicate weathering rates and the coupling with physical erosion: new insights from rivers of the Canadian Shield. *Earth and Planetary Science Letters*, *196*, 83–98. www.elsevier.com/locate/epsl

Ministerio de Obras Públicas - Dirección de General de Aguas. (n.d.). Retrieved September 7, 2023, from https://dga.mop.gob.cl/servicioshidrometeorologicos/Paginas/default.aspx

Moon, S., Chamberlain, C. P., & Hilley, G. E. (2014). New estimates of silicate weathering rates and their uncertainties in global rivers. *Geochimica et Cosmochimica Acta*, *134*, 257–274. https://doi.org/10.1016/j.gca.2014.02.033

Moquet, J. S., Crave, A., Viers, J., Seyler, P., Armijos, E., Bourrel, L., Chavarri, E., Lagane, C., Laraque, A., Casimiro, W. S. L., Pombosa, R., Noriega, L., Vera, A., & Guyot, J. L. (2011). Chemical weathering and atmospheric/soil CO2 uptake in the Andean and Foreland Amazon basins. *Chemical Geology*, *287*(1–2), 1–26. https://doi.org/10.1016/j.chemgeo.2011.01.005

Mortlock, R. A., & Froelich, P. N. (1987). Continental weathering of germanium: Ge/Si in the global river discharge. *Geochimica et Cosmochimica*, *51*, 2075–2082.

Mortlock, R. A., & Froelich, P. N. (1996). Determination of germanium by isotope dilution-hydride generation inductively coupled plasma mass spectrometry. *Analytica Chimica Acta*, *332*(2–3), 277–284. https://doi.org/10.1016/0003-2670(96)00230-9

Munizaga, F., Herve, F., Drake, R., Pankhurst, R. J., Brook, M., & Snelling, N. (1988). Geochronology of the Lake Region of south-central Chile (39°–42°S): Preliminary results. *Journal of South American Earth Sciences*, *1*(3), 309–316. https://doi.org/10.1016/0895-9811(88)90009-0

Murnane, R. J., & Stallard, R. F. (1990). Germanium and silicon in rivers of the Orinoco drainage basin. *Nature 1990 344:6268*, *344*(6268), 749–752. https://doi.org/10.1038/344749a0

Negrel, P., Allegre, C. J., Dupre, B., & Lewin, E. (1993). Erosion sources determined by inversion of major and trace element ratios and strontium isotopic ratios in river water: The Congo Basin case. In *Earth and Planetary Science Letters* (Vol. 120).

Négrel, P., & Deschamps, P. (1996). Natural and anthropogenic budgets of a small watershed in the Massif Central (France): chemical and strontium isotopic characterization of water and sediments. *Aquatic Geochemistry*, *2*(1), 1–27. https://doi.org/10.1007/BF00240851

Negri, A., Daniele, L., Aravena, D., Muñoz, M., Delgado, A., & Morata, D. (2018). Decoding fjord water contribution and geochemical processes in the Aysen thermal springs (Southern Patagonia, Chile). *Journal of Geochemical Exploration*, *185*, 1–13. https://doi.org/10.1016/j.gexplo.2017.10.026

Oeser, R. A., Stroncik, N., Moskwa, L. M., Bernhard, N., Schaller, M., Canessa, R., van den Brink, L., Köster, M., Brucker, E., Stock, S., Fuentes, J. P., Godoy, R., Matus, F. J., Oses Pedraza, R., Osses McIntyre, P., Paulino, L., Seguel, O., Bader, M. Y., Boy, J., … von Blanckenburg, F. (2018). Chemistry and microbiology of the Critical Zone along a steep climate and vegetation gradient in the Chilean Coastal Cordillera. *Catena*, *170*, 183–203. https://doi.org/10.1016/j.catena.2018.06.002

Oeser, R. A., & von Blanckenburg, F. (2020). Strontium isotopes trace biological activity in the Critical Zone along a climate and vegetation gradient. *Chemical Geology*, *558*. https://doi.org/10.1016/j.chemgeo.2020.119861

O'leary, M. H. (1988). Carbon Isotopes in Photosyn Fractionation techniques may reveal new aspects of carbon dynamics in plants. *BioScience*, *38*, 328–336.

Oudin, L., Andréassian, V., Perrin, C., Michel, C., & Le Moine, N. (2008). Spatial proximity, physical similarity, regression and ungaged catchments: A comparison of regionalization approaches based on 913 French catchments. *Water Resources Research*, *44*(3). https://doi.org/10.1029/2007WR006240

Oudin, L., Kay, A., Andráassian, V., & Perrin, C. (2010). Are seemingly physically similar catchments truly hydrologically similar? *Water Resources Research*, *46*(11). https://doi.org/10.1029/2009WR008887

Palmer, M. R., Spivack, A. J., & Edmond, J. M. (1987). Temperature and pH controls over isotopic fractionation during adsorption of boron on marine clay. In *Gwchrrmca n Cosmorhrmrca Acta* (Vol. 5).

Palmer, M. R., & Sturchio, N. C. (1990). The boron isotope systematics of the Yellowstone National Park (Wyoming) hydrothermal system: A reconnaissance. *Geochimica et Cosmochimica Acta*, *54*(10), 2811–2815. https://doi.org/10.1016/0016-7037(90)90015-D

Pankhurst, R. J., Weaver, S. D., Hervé, F., & Larrondo, P. (1999). Mesozoic-Cenozoic evolution of the North Patagonian Batholith in Aysen, southern Chile. *Journal of the Geological Society*, *156*(4), 673–694. https://doi.org/10.1144/GSJGS.156.4.0673

Parada, M. A., Lahsen, A., & Palacios, C. (2001). Ages and geochemistry of Mesozoic-Eocene back-arc volcanic rocks in the Aysén region of the Patagonian Andes, Chile. *Revista Geológica de Chile*, *28*(1), 25–46. https://doi.org/10.4067/S0716-02082001000100002

Parajka, J., Viglione, A., Rogger, M., Salinas, J. L., Sivapalan, M., & Blöschl, G. (2013). Comparative assessment of predictions in ungauged basins-Part 1: Runoff-hydrograph studies. *Hydrology and Earth System Sciences*, *17*(5), 1783–1795. https://doi.org/10.5194/HESS-17-1783-2013

Pedroza, V., Le Roux, J. P., Gutiérrez, N. M., & Vicencio, V. E. (2017). Stratigraphy, sedimentology, and geothermal reservoir potential of the volcaniclastic Cura-Mallín succession at Lonquimay, Chile. *Journal of South American Earth Sciences*, *77*, 1–20. https://doi.org/10.1016/J.JSAMES.2017.04.011

Pennisi, M., Bianchini, G., Muti, A., Kloppmann, W., & Gonfiantini, R. (2006). Behaviour of boron and strontium isotopes in groundwater–aquifer interactions in the Cornia Plain (Tuscany, Italy). *Applied Geochemistry*, *21*(7), 1169–1183. https://doi.org/10.1016/J.APGEOCHEM.2006.03.001

Pepin, E., Carretier, S., Guyot, J. L., & Escobar, F. (2010). Specific suspended sediment yields ofthe Andean rivers ofChile and their relationship to climate, slope and vegetation. *Hydrological Sciences Journal*, *55*(7), 1190–1205. https://doi.org/10.1080/02626667.2010.512868

Pérez-Estay, N., Molina-Piernas, E., Roquer, T., Aravena, D., Araya Vargas, J., Morata, D., Arancibia, G., Valdenegro, P., García, K., & Elizalde, D. (2022). Shallow anatomy of hy-

drothermal systems controlled by the Liquiñe-Ofqui Fault System and the Andean Transverse Faults: Geophysical imaging of fluid pathways and practical implications for geothermal exploration. *Geothermics, 104*. https://doi.org/10.1016/j.geothermics.2022.102435

Pérez-Flores, P., Cembrano, J., Sánchez-Alfaro, P., Veloso, E., Arancibia, G., & Roquer, T. (2016). Tectonics, magmatism and paleo-fluid distribution in a strike-slip setting: Insights from the northern termination of the Liquiñe-Ofqui fault System, Chile. *Tectonophysics, 680*, 192–210. https://doi.org/10.1016/j.tecto.2016.05.016

Pérez-Flores, P., Wang, G., Mitchell, T. M., Meredith, P. G., Nara, Y., Sarkar, V., & Cembrano, J. (2017). The effect of offset on fracture permeability of rocks from the Southern Andes Volcanic Zone, Chile. *Journal of Structural Geology, 104*, 142–158. https://doi.org/10.1016/j.jsg.2017.09.015

Pérez-Moreno, R., Reich, M., Daniele, L., Morata, D., Held, S., & Kleinsasser, J. (2021). Stable isotope and anthropogenic tracer signature of waters in an Andean geothermal system. *Applied Geochemistry, 128*. https://doi.org/10.1016/j.apgeochem.2021.104953

Pistolesi, M., Cioni, R., Bonadonna, C., Elissondo, M., Baumann, V., Bertagnini, A., Chiari, L., Gonzales, R., Rosi, M., & Francalanci, L. (2015). Complex dynamics of small-moderate volcanic events: the example of the 2011 rhyolitic Cordón Caulle eruption, Chile. *Bulletin of Volcanology, 77*(1). https://doi.org/10.1007/s00445-014-0898-3

Pokrovsky, O., Schott, J., Kudryavtzev, D., & Dupré, B. (2005). Basalt weathering in Central Siberia under permafrost conditions. *Geochimica et Cosmochimica Acta, 69*, 5659–5680. https://www.sciencedirect.com/science/article/pii/S001670370500668X

Quevedo, M. A. (2021). *METODOLOGÍA PARA EL RELLENO DE REGISTROS FLUVIOMÉTRICOS DIARIOS EN CUENCAS CHILENAS CERCANAS AL RÉGIMEN NATURAL.*

Rad, S., Allegre, C., & Louvat, P. (2007). Hidden erosion on volcanic islands. *Earth and Planetary Science Letters, 262*(1–2), 109–124. https://doi.org/10.1016/j.epsl.2007.07.019

Rad, S., Louvat, P., Gorge, C., Gaillardet, J., & Allégre, C. J. (2006). River dissolved and solid loads in the Lesser Antilles: New insight into basalt weathering processes. *Journal of Geochemical Exploration, 88*(1-3 SPEC. ISS.), 308–312. https://doi.org/10.1016/j.gexplo.2005.08.063

Rad, S., Rivé, K., Vittecoq, B., Cerdan, O., & Allègre, C. J. (2013). Chemical weathering and erosion rates in the lesser antilles: An overview in guadeloupe, martinique and dominica. In

Journal of South American Earth Sciences (Vol. 45, pp. 331–344). https://doi.org/10.1016/j.jsames.2013.03.004

Radic, J. P. (2010). Las cuencas cenozoicas y su control en el volcanismo de los Complejos Nevados de Chillan y Copahue-Callaqui (Andes del Sur, 36-39°S). *Andean Geology*, *37*(1), 220–246. https://doi.org/10.4067/S0718-71062010000100009

Rasmussen, C., Dahlgren, R. A., & Southard, R. J. (2010). Basalt weathering and pedogenesis across an environmental gradient in the southern Cascade Range, California, USA. *Geoderma*, *154*(3–4), 473–485. https://doi.org/10.1016/j.geoderma.2009.05.019

Ray, M. C., Hilton, D. R., Muñoz, J., Fischer, T. P., & Shaw, A. M. (2009). The effects of volatile recycling, degassing and crustal contamination on the helium and carbon geochemistry of hydrothermal fluids from the Southern Volcanic Zone of Chile. *Chemical Geology*, *266*(1–2), 38–49. https://doi.org/10.1016/j.chemgeo.2008.12.026

Risacher, F., Fritz, B., & Hauser, A. (2011). Origin of components in Chilean thermal waters. *Journal of South American Earth Sciences*, *31*(1), 153–170. https://doi.org/10.1016/j.jsames.2010.07.002

Rivé, K., Gaillardet, J., Agrinier, P., & Rad, S. (2013). Carbon isotopes in the rivers from the Lesser Antilles: Origin of the carbonic acid consumed by weathering reactions in the Lesser Antilles. *Earth Surface Processes and Landforms*, *38*(9), 1020–1035. https://doi.org/10.1002/esp.3385

Romero-Mujalli, G., Hartmann, J., Hosono, T., Louvat, P., Okamura, K., Delmelle, P., Amann, T., & Böttcher, M. E. (2022). Hydrothermal and magmatic contributions to surface waters in the Aso caldera, southern Japan: Implications for weathering processes in volcanic areas. *Chemical Geology*, *588*. https://doi.org/10.1016/j.chemgeo.2021.120612

Roquer, T., Arancibia, G., Rowland, J., Iturrieta, P., Morata, D., & Cembrano, J. (2017). Fault-controlled development of shallow hydrothermal systems: Structural and mineralogical insights from the Southern Andes. *Geothermics*, *66*, 156–173. https://doi.org/10.1016/j.geothermics.2016.12.003

Rose, E. F., Chaussidon, M., & France-Lanord, C. (2000). *Fractionation of Boron isotopes during erosion processes: The example of Himalayan rivers.*

Rose-Koga, E. F., Sheppard, S. M. F., Chaussidon, M., & Carignan, J. (2006). Boron isotopic composition of atmospheric precipitations and liquid–vapour fractionations. *Geochimica et Cosmochimica Acta*, *70*(7), 1603–1615. https://doi.org/10.1016/J.GCA.2006.01.003

Rosenau, M., Melnick, D., Tectonics, H. E.-, & 2006, undefined. (2006). Kinematic constraints on intra-arc shear and strain partitioning in the southern Andes between 38 S and 42 S latitude. *Wiley Online Library*, *25*(4). https://doi.org/10.1029/2005TC001943

Roux, P., Turpault, M. P., Kirchen, G., Redon, P. O., & Lemarchand, D. (2017). Boron Dissolved and Particulate Atmospheric Inputs to a Forest Ecosystem (Northeastern France). *Environmental Science and Technology*, *51*(24), 14038–14046. https://doi.org/10.1021/acs.est.7b03226

Roy, S., Gaillardet, J., Allegre, C., & 1999, undefined. (1999). Geochemistry of dissolved and suspended loads of the Seine river, France: anthropogenic impact, carbonate and silicate weathering. *Geochimica et Cosmochimica Acta*, *63*(9), 1277–1292. https://www.sciencedirect.com/science/article/pii/S001670379900099X

Royer, D. L., Berner, R. A., & Park, J. (2007). Climate sensitivity constrained by CO2 concentrations over the past 420 million years. *Nature*, *446*(7135), 530–532. https://doi.org/10.1038/nature05699

Sabine, C., Bala, G., Bopp, L., Brovkin, V., Canadell, J., Chhabra, A., DeFries, R., Galloway, J., Heimann, M., Jones, C., Le Quéré, C., Myneni, R., Piao, S., Thornton, P., Qin, D., Plattner, G., Tignor, M., Allen, S., Boschung, J., … Brovkin Germany, V. (2013). *Carbon and Other Biogeochemical Cycles*. Peter.

Sánchez, P., Pérez-Flores, P., Arancibia, G., Cembrano, J., & Reich, M. (2013). Crustal deformation effects on the chemical evolution of geothermal systems: The intra-arc Liquiñe-Ofqui fault system, Southern Andes. *International Geology Review*, *55*(11), 1384–1400. https://doi.org/10.1080/00206814.2013.775731

Schaller, M., & Ehlers, T. A. (2022). Comparison of soil production, chemical weathering, and physical erosion rates along a climate and ecological gradient (Chile) to global observations. *Earth Surface Dynamics*, *10*(1), 131–150. https://doi.org/10.5194/ESURF-10-131-2022

Schaller, M., Ehlers, T. A., Lang, K. A. H., Schmid, M., & Fuentes-Espoz, J. P. (2018). Addressing the contribution of climate and vegetation cover on hillslope denudation, Chilean Coastal Cordillera (26°–38°S). *Earth and Planetary Science Letters*, *489*, 111–122. https://doi.org/10.1016/J.EPSL.2018.02.026

Schmitt, A. D., Vigier, N., Lemarchand, D., Millot, R., Stille, P., & Chabaux, F. (2012). Processes controlling the stable isotope compositions of Li, B, Mg and Ca in plants, soils and waters: A review. In *Comptes Rendus - Geoscience* (Vol. 344, Issues 11–12, pp. 704–722). https://doi.org/10.1016/j.crte.2012.10.002

Schopka, H. H., & Derry, L. A. (2012). Chemical weathering fluxes from volcanic islands and the importance of groundwater: The Hawaiian example. *Earth and Planetary Science Letters*, *339–340*, 67–78. https://doi.org/10.1016/j.epsl.2012.05.028

Schopka, H. H., Derry, L. A., & Arcilla, C. A. (2011). Chemical weathering, river geochemistry and atmospheric carbon fluxes from volcanic and ultramafic regions on Luzon Island, the Philippines. *Geochimica et Cosmochimica Acta*, *75*(4), 978–1002. https://doi.org/10.1016/j.gca.2010.11.014

Schuller, P., Walling, D. E., Iroumé, A., Quilodrán, C., Castillo, A., & Navas, A. (2013). Using 137Cs and 210Pbex and other sediment source fingerprints to document suspended sediment sources in small forested catchments in south-central Chile. *Journal of Environmental Radioactivity*, *124*, 147–159. https://doi.org/10.1016/j.jenvrad.2013.05.002

Scribner, A. M., Kurtz, A. C., & Chadwick, O. A. (2006). Germanium sequestration by soil: Targeting the roles of secondary clays and Fe-oxyhydroxides. *Earth and Planetary Science Letters*, *243*(3–4), 760–770. https://doi.org/10.1016/J.EPSL.2006.01.051

Siebert, C., Ross, A., & McManus, J. (2006). Germanium isotope measurements of high-temperature geothermal fluids using double-spike hydride generation MC-ICP-MS. *Geochimica et Cosmochimica Acta*, *70*(15), 3986–3995. https://doi.org/10.1016/J.GCA.2006.06.007

Singer, B. S., Jicha, B. R., Harper, M. A., Naranjo, J. A., Lara, L. E., & Moreno-Roa, H. (2008). Eruptive history, geochronology, and magmatic evolution of the Puyehue-Cordón Caulle volcanic complex, Chile. *GSA Bulletin*, *120*(5–6), 599–618. https://doi.org/10.1130/B26276.1

Spivack, A. J., Palmer, M. R., & Edmond, J. M. (1987). *The sedimentary cycle of the boron isotopes.*

Stefánsson, A., Sveinbjörnsdóttir, Á. E., Heinemeier, J., Arnórsson, S., Kjartansdóttir, R., & Kristmannsdóttir, H. (2016). Mantle CO2 degassing through the Icelandic crust: Evidence from carbon isotopes in groundwater. *Geochimica et Cosmochimica Acta*, *191*. https://doi.org/10.1016/j.gca.2016.06.038

Stern, C. R. (2004). Active Andean volcanism: its geologic and tectonic setting. *Revista Geológica de Chile*, *31*(2), 161–206. https://doi.org/10.4067/S0716-02082004000200001

Suárez, M., & De la Cruz, R. (2001). Jurassic to Miocene K–Ar dates from eastern central Patagonian Cordillera plutons, Chile (45°–48° S). *Geological Magazine*, *138*(1), 53–66. https://doi.org/10.1017/S0016756801004903

Tardani, D., Reich, M., Roulleau, E., Takahata, N., Sano, Y., Pérez-Flores, P., Sánchez-Alfaro, P., Cembrano, J., & Arancibia, G. (2016). Exploring the structural controls on helium, nitrogen and carbon isotope signatures in hydrothermal fluids along an intra-arc fault system. *Geochimica et Cosmochimica Acta, 184*, 193–211. https://doi.org/10.1016/j.gca.2016.04.031

Tassara, A., & Yañez, G. (2003). Relación entre el espesor elástico de la listosfera y la segmentación tectónica del margen andino (15-47°S). *Revista Geológica de Chile, 30*(2), 159–186.

Tolorza, V., Carretier, S., Andermann, C., Ortega-Culaciati, F., Pinto, L., & Mardones, M. (2014). Contrasting mountain and piedmont dynamics of sediment discharge associated with groundwater storage variation in the Biobío River. *Journal of Geophysical Research: Earth Surface, 119*(12), 2730–2753. https://doi.org/10.1002/2014JF003105

Vasyukova, E., Oliva, P., Viers, J., Martin, F., Dupré, B., & Pokrovsky, O. (2019). Chemical weathering of mafic rocks in boreal subarctic environment (northwest Russia) under influence of glacial moraine deposits. *Elsevier Geology, 509*, 115–133. https://www.sciencedirect.com/science/article/pii/S0009254118306259

Vázquez, M., Ramírez, S., Morata, D., Reich, M., Braun, J. J., & Carretier, S. (2016). Regolith production and chemical weathering of granitic rocks in central Chile. *Chemical Geology, 446*, 87–98. https://doi.org/10.1016/J.CHEMGEO.2016.09.023

Velbel, M. (1993). Temperature dependence of silicate weathering in nature: How strong a negative feedback on long-term accumulation of atmospheric CO2 and global greenhouse warming? *Geology, 21*, 1059–1062. https://pubs.geoscienceworld.org/gsa/geology/article-abstract/21/12/1059/197709

Vengosh, A., Heumann, K. G., Juraske, S., & Kasher, R. (1994). Boron Isotope Application for Tracing Sources of Contamination in Groundwater. *Environ. Sci. Technol, 28*, 1968–1974. https://pubs.acs.org/sharingguidelines

Viers, J., Carretier, S., Auda, Y., Pokrovsky, O. S., Seyler, P., Chabaux, F., Regard, V., Tolorza, V., & Herail, G. (2019). Geochemistry of Chilean Rivers Within the Central Zone: Distinguishing the Impact of Mining, Lithology and Physical Weathering. *Aquatic Geochemistry, 25*(1–2), 27–48. https://doi.org/10.1007/s10498-019-09350-1

Viers, J., Oliva, P., Dandurand, J. L., Dupré, B., & Gaillardet, J. (2013). Chemical Weathering Rates, CO2 Consumption, and Control Parameters Deduced from the Chemical Composition of Rivers. In *Treatise on Geochemistry: Second Edition* (Vol. 7). https://doi.org/10.1016/B978-0-08-095975-7.00506-4

Völker, D., Kutterolf, S., & Wehrmann, H. (2011). Comparative mass balance of volcanic edifices at the southern volcanic zone of the Andes between 33°S and 46°S. *Journal of Volcanology and Geothermal Research*, *205*(3–4), 114–129. https://doi.org/10.1016/j.jvolgeores.2011.03.011

Walker, J. C. G., Hays, P. B., & Kasting, J. F. (1981). A negative feedback mechanism for the long-term stabilization of Earth's surface temperature. *Journal of Geophysical Research*, *86*(C10), 9776–9782. https://doi.org/10.1029/JC086iC10p09776

Werner, C., Brantley, S. L., & Boomer, K. (2000). CO2 emissions related to the Yellowstone volcanic system 2. Statistical sampling, total degassing, and transport mechanisms. *Journal of Geophysical Research: Solid Earth*, *105*(B5), 10831–10846. https://doi.org/10.1029/1999jb900331

Wheat, C. G., Mcmanus, J., Wheat, C. G., & Mcmanus, J. (2008). Germanium in mid-ocean ridge flank hydrothermal fluids. *Geochemistry, Geophysics, Geosystems*, *9*(3), 3025. https://doi.org/10.1029/2007GC001892

White, D. E. (1970). *Geochemistry applied to the discovery, evaluation, and exploitation of geothermal energy resources.* 58–80.

Wrage, J., Tardani, D., Reich, M., Daniele, L., Arancibia, G., Cembrano, J., Sánchez-Alfaro, P., Morata, D., & Pérez-Moreno, R. (2017). Geochemistry of thermal waters in the Southern Volcanic Zone, Chile – Implications for structural controls on geothermal fluid composition. *Chemical Geology*, *466*, 545–561. https://doi.org/10.1016/j.chemgeo.2017.07.004

Wymore, A. S., Brereton, R. L., Ibarra, D. E., Maher, K., & McDowell, W. H. (2017). Critical zone structure controls concentration-discharge relationships and solute generation in forested tropical montane watersheds. *Water Resources Research*, *53*(7), 6279–6295. https://doi.org/10.1002/2016WR020016

Xiao, J., Xiao, Y. K., Jin, Z. D., He, M. Y., & Liu, C. Q. (2013). Boron isotope variations and its geochemical application in nature. *Australian Journal of Earth Sciences*, *60*(4), 431–447. https://doi.org/10.1080/08120099.2013.813585

Yamada, M., Ohsawa, S., Kazahaya, K., Yasuhara, M., Takahashi, H., Amita, K., Mawatari, H., & Yoshikawa, S. (2011). Mixing of magmatic CO2 into volcano groundwater flow at Aso volcano assessed combining carbon and water stable isotopes. *Journal of Geochemical Exploration*, *108*(1). https://doi.org/10.1016/j.gexplo.2010.10.007

Zhang, S., Bai, X., Zhao, C., Tan, Q., Luo, G., Wang, J., Li, Q., Wu, L., Chen, F., Li, C., Deng, Y., Yang, Y., & Xi, H. (2021). Global CO2 Consumption by Silicate Rock Chemical Weathering: Its Past and Future. *Earth's Future*, *9*(5). https://doi.org/10.1029/2020EF001938

Zhao, Z. Q., & Liu, C. Q. (2010). Anthropogenic inputs of boron into urban atmosphere: Evidence from boron isotopes of precipitations in Guiyang City, China. *Atmospheric Environment*, *44*(34), 4165–4171. https://doi.org/10.1016/J.ATMOSENV.2010.07.035

Zhong, J., Wang, L., Caracausi, A., Galy, A., Li, S. L., Wang, W., Zhang, M., Liu, C. Q., Liu, G. M., & Xu, S. (2023). Assessing the Deep Carbon Release in an Active Volcanic Field Using Hydrochemistry, δ13CDIC and Δ14CDIC. *Journal of Geophysical Research: Biogeosciences*, *128*(4). https://doi.org/10.1029/2023JG007435

Annexes

Annex A: Trace Elements

Table 10: Concentrations of trace elements in rivers and hot springs during year 2021 and summer of 2022. Rb, Sr, Zr, Ag, Cd, Sb, Ba, Pb, Th, U (ppb)

SampleID	ID	Location	Type	Seasson	Year	Rb ppb	Sr ppb	Zr ppb	Mo ppb	Ag ppb	Cd ppb	Sb ppb	Ba ppb	Pb ppb	Th ppb	U ppb
SVZ030	1	Malleco	River	Summer	2021	1.00	12.95	0.14	0.26	-	-	0.21	1.28	0.01	0.10	-
SVZ029	2	Cautin	River	Summer	2021	2.38	25.99	0.14	0.25	0.00	-	0.18	1.56	0.01	0.10	-
SVZ031	3	Blanco at Cura-cautin	River	Summer	2021	2.57	20.84	0.18	0.35	0.00	-	0.32	0.19	<LOQ	0.09	-
SVZ000	4	Truful-Trufl	River	Summer	2021	1.75	17.06	0.17	0.54	-	-	0.18	0.64	0.01	0.11	0.01
SVZ033	5	Allipen	River	Summer	2021	1.57	17.11	0.15	0.45	0.01	-	0.14	1.07	0.01	0.10	0.01
SVZ034	6	Alpehue	River	Summer	2021	1.29	8.72	0.15	0.16	-	-	0.06	0.85	0.01	0.09	-
SVZ028	7	Trancura	River	Summer	2021	3.36	24.44	0.15	0.74	-	-	0.10	2.74	0.01	0.10	-
SVZ026	8	Voipir	River	Summer	2021	1.43	15.31	0.16	0.16	0.02	-	0.12	0.49	0.01	0.09	-
SVZ027	9	Palguin	River	Winter	2022	2.78	17.26	0.14	0.30	-	-	0.12	1.06	0.01	0.10	-
SVZ019	10	Liquiñe	River	Summer	2021	2.35	18.74	0.15	0.91	0.01	-	0.10	2.32	0.02	0.10	0.03
SVZ017	11	Caunahue	River	Summer	2021	0.98	21.85	0.14	1.21	-	0.00	0.17	2.40	0.01	0.09	0.02
SVZ018	12	Curriñe	River	Summer	2021	0.91	32.93	0.14	3.24	-	0.01	0.07	3.67	0.01	0.10	0.02
SVZ015	13	Nilahue	River	Summer	2021	18.87	82.29	0.65	1.76	-	-	0.30	9.52	0.01	0.46	0.13
SVZ016	14	Los Venados	River	Summer	2021	1.91	16.63	0.14	0.46	0.00	-	0.17	1.46	0.01	0.09	-
SVZ006	15	Chirre	River	Summer	2021	2.64	26.95	0.18	0.28	-	-	0.10	2.23	0.02	0.12	-
SVZ010	16	Gol-Gol	River	Summer	2021	2.42	20.55	0.16	0.37	-	-	0.10	2.05	0.02	0.11	-
SVZ008	17	Chanleufu	River	Summer	2021	1.59	22.17	0.14	0.23	-	-	0.16	1.68	0.01	0.10	-
SVZ005	18	Coihueco	River	Summer	2021	1.76	25.57	0.15	0.18	-	-	0.09	2.33	0.03	0.10	-
SVZ004	19	Blanco at R-225	River	Summer	2021	2.44	13.43	0.15	0.19	-	-	0.18	0.83	0.01	0.11	-
SVZ003	20	Chico	River	Summer	2021	1.46	28.47	0.19	0.29	-	-	0.10	1.64	0.02	0.14	-

Table 12: Continued

SampleID	ID	Location	Type	Seasson	Year	Rb ppb	Sr ppb	Zr ppb	Mo ppb	Ag ppb	Cd ppb	Sb ppb	Ba ppb	Pb ppb	Th ppb	U ppb
SVZ001	21	Blanco before Chamiza	River	Summer	2021	1.74	19.96	0.15	0.17	-	-	0.14	1.53	0.01	0.11	-
SVZ002	22	Chamiza	River	Summer	2021	1.70	24.24	0.17	0.27	0.00	-	0.11	1.69	0.02	0.14	-
SVZ115	A	Pemehue	Hot Springs	Winter	2022	283.85	2325.31	< 0.2	20.58	< 0.06	< 0.08	13.67	10.63	< 0.2	-	< 0.02
SVZ024	B	Malleco	Hot Springs	Summer	2021	37.67	89.32	1.33	0.33	-	-	12.55	2.82	<LOQ	0.94	-
SVZ023	C	Malalcahuello	Hot Springs	Summer	2021	2.90	31.44	0.54	4.78	-	-	1.92	0.95	0.01	0.38	-
SVZ117	D	Molulco-Balboa	Hot Springs	Winter	2022	89.42	141.91	< 0.05	11.57	< 0.015	< 0.02	6.67	3.93	0.01	-	0.01
SVZ045	E	Alpehue	Hot Springs	Summer	2021	154.09	23.30	2.42	2.10	-	-	1.49	5.01	<LOQ	1.75	-
SVZ021	F	Menetue	Hot Springs	Summer	2021	11.27	36.08	1.28	22.92	-	-	0.61	0.60	0.01	0.62	-
SVZ014	G1	Palguin at El Litio	Hot Springs	Summer	2021	7.02	27.02	0.86	13.60	0.11	-	1.27	1.46	0.02	0.54	-
SVZ020	G2	Palguin at El Mote	Hot Springs	Summer	2021	5.95	13.40	0.71	5.95	-	-	0.12	1.04	0.01	0.43	-
SVZ022	H	Geometricas	Hot Springs	Summer	2021	33.60	392.87	2.60	8.22	-	-	2.44	2.24	0.04	1.84	-
SVZ013	I	Coñaripe	Hot Springs	Summer	2021	19.33	54.84	1.39	21.47	0.14	-	30.30	5.21	<LOQ	0.98	-
SVZ012	J	Punulaf	Hot Springs	Summer	2021	21.28	63.93	0.76	12.21	0.00	-	0.42	0.61	0.05	0.52	-
SVZ011	K	Hipolito Muñoz	Hot Springs	Summer	2021	21.11	65.23	1.16	2.50	-	-	0.18	0.14	0.01	0.61	-
SVZ009	L	Cerrillos	Hot Springs	Summer	2021	4.02	43.10	0.55	12.29	0.07	0.01	0.37	0.06	0.02	0.39	-
SVZ133	M	Chihuio	Hot Springs	Winter	2022	15.41	301.94	< 0.01	20.92	< 0.003	< 0.004	< 0.01	6.29	0.00	-	< 0.001
SVZ083	N	Lava 2011	Hot Springs	Summer	2022	39.50	147.45	< 0.05	2.64	< 0.015	< 0.02	< 0.05	14.93	< 0.05	-	0.66
SVZ068	O	Aguas Calientes	Hot Springs	Winter	2021	77.90	250.96	1.54	1.54	10.73	0.08	<0.01	104.95	21.38	-	0.03
SVZ047	1	Malleco	River	Winter	2021	0.62	10.75	<0.01	<0.01	<0.01	<0.003	<0.01	0.11	<0.01	-	<0.001
SVZ048	2	Cautin	River	Winter	2021	1.97	25.51	<0.01	<0.01	<0.01	<0.003	<0.01	0.15	<0.01	-	0.01
SVZ046	3	Blanco at Cura-cautin	River	Winter	2021	1.82	19.55	<0.01	<0.01	<0.01	<0.003	<0.01	0.09	<0.01	-	<0.001
SVZ050	4	Truful-Trulf	River	Winter	2021	1.83	18.92	<0.01	<0.01	<0.01	<0.003	<0.01	0.14	<0.01	-	0.07
SVZ049	5	Allipen	River	Winter	2021	1.99	24.98	<0.01	<0.01	<0.01	<0.003	<0.01	0.19	<0.01	-	0.08
SVZ052	6	Alpehue	River	Winter	2021	2.08	18.55	<0.01	<0.01	<0.01	<0.003	<0.01	0.07	<0.01	-	0.01
SVZ057	7	Trancura	River	Winter	2021	2.39	26.92	<0.01	<0.01	<0.01	<0.003	<0.01	0.17	<0.01	-	0.02
SVZ051	8	Voipir	River	Winter	2021	2.60	23.23	<0.01	<0.01	<0.01	<0.003	<0.01	0.10	<0.01	-	0.02

Table 12: Continued

SampleID	ID	Location	Type	Seasson	Year	Rb ppb	Sr ppb	Zr ppb	Mo ppb	Ag ppb	Cd ppb	Sb ppb	Ba ppb	Pb ppb	Th ppb	U ppb
SVZ056	9	Palguin	River	Winter	2021	2.56	19.71	<0.01	<0.01	<0.01	<0.003	<0.01	0.16	<0.01	-	0.01
SVZ053	10	Liquiñe	River	Winter	2021	1.58	18.08	<0.01	<0.01	<0.01	<0.003	<0.01	0.28	<0.01	-	0.05
SVZ063	11	Caunahue	River	Winter	2021	0.86	19.47	<0.01	<0.01	<0.01	<0.003	<0.01	0.04	<0.01	-	0.04
SVZ060	12	Curriñe	River	Winter	2021	1.14	29.77	<0.01	<0.01	1.76	<0.003	<0.01	0.07	<0.01	-	0.05
SVZ061	13	Nilahue	River	Winter	2021	12.53	62.34	<0.01	<0.01	0.85	<0.003	<0.01	1.67	<0.01	-	0.16
SVZ055	14	Los Venados	River	Winter	2021	1.99	20.23	<0.01	<0.01	<0.01	<0.003	<0.01	0.06	<0.01	-	0.03
SVZ064	15	Chirre	River	Winter	2021	2.06	21.08	0.05	0.05	<0.01	<0.003	<0.01	0.05	<0.01	-	<0.001
SVZ058	16	Gol-Gol	River	Winter	2021	1.47	16.67	<0.01	<0.01	<0.01	<0.003	<0.01	0.15	<0.01	-	0.01
SVZ062	17	Chanleufu	River	Winter	2021	1.36	19.59	<0.01	<0.01	<0.01	<0.003	<0.01	0.22	<0.01	-	0.01
SVZ065	18	Coihueco	River	Winter	2021	1.52	19.46	<0.01	<0.01	<0.01	<0.003	<0.01	0.05	<0.01	-	<0.001
SVZ066	19	Blanco at R-225	River	Winter	2021	1.70	14.24	<0.01	<0.01	<0.01	<0.003	<0.01	0.11	<0.01	-	0.00
SVZ067	20	Chico	River	Winter	2021	0.64	12.53	0.26	0.26	<0.01	<0.003	<0.01	<0.001	<0.01	-	<0.001
SVZ069	21	Blanco	River	Winter	2021	1.32	18.97	<0.01	<0.01	<0.01	<0.01	<0.01	0.09	<0.01	-	<0.001
SVZ070	22	Chamiza	River	Winter	2021	0.88	15.22	0.07	0.07	<0.01	<0.01	<0.01	<0.001	<0.01	-	0.01

Table 11: Concentrations of trace elements in rivers and hot springs during year 2021 and summer of 2022. Ti, V, Cr, Mn, Co, Ni, Cu, Zn, As, Se, Y, La, Ce, Nd, Eu (ppb).

SampleID	ID	Location	Type	Seasson	Year	Ti ppb	V ppb	Cr ppb	Mn ppb	Co ppb	Ni ppb	Cu ppb	Zn ppb	As ppb	Se ppb	Y ppb	La ppb	Ce ppb	Nd ppb	Eu ppb
SVZ030	1	Malleco	River	Summer	2021	0.05	0.86	0.01	1.06	0.01	-	0.07	6.74	2.96	0.03	0.00	0.01	-	0.01	0.00
SVZ029	2	Cautin	River	Summer	2021	0.29	7.39	0.04	1.61	0.01	-	0.24	8.34	1.72	0.08	0.00	0.01	-	0.00	0.00
SVZ031	3	Blanco at Curacautin	River	Summer	2021	0.18	1.89	0.02	3.90	0.01	-	0.14	0.72	2.21	0.04	-	0.00	-	0.00	0.00
SVZ000	4	Truful-Trulf	River	Summer	2021	0.30	21.69	0.09	0.11	0.00	-	0.20	9.03	1.36	0.19	-	0.01	-	0.00	0.00
SVZ033	5	Allipen	River	Summer	2021	0.56	11.73	0.06	1.96	0.01	-	0.18	4.44	1.38	0.10	0.00	0.01	0.01	0.01	0.00
SVZ034	6	Alpehue	River	Summer	2021	0.59	1.95	0.06	1.34	0.01	-	0.09	8.85	0.35	0.06	0.00	0.01	0.01	0.01	0.00
SVZ028	7	Trancura	River	Summer	2021	0.23	4.46	0.07	6.73	0.03	-	0.18	4.91	0.69	0.05	0.00	0.01	0.00	0.00	0.00
SVZ026	8	Voipir	River	Summer	2021	1.40	8.14	0.08	4.09	0.04	0.06	0.41	10.75	0.52	0.05	0.00	0.01	0.00	0.00	0.00
SVZ027	9	Palguin	River	Winter	2022	0.11	6.79	0.07	0.28	0.00	-	0.14	7.23	0.98	0.08	0.01	0.01	-	0.01	0.00
SVZ019	10	Liquiñe	River	Summer	2021	0.57	3.32	0.04	0.59	0.01	-	0.14	8.43	1.09	0.12	-	0.01	0.00	0.00	0.00
SVZ017	11	Caunahue	River	Summer	2021	0.06	1.03	0.02	1.12	0.01	-	0.20	6.79	1.53	0.07	-	0.01	-	0.00	0.00
SVZ018	12	Curriñe	River	Summer	2021	0.02	0.51	0.02	0.47	0.01	-	0.16	8.03	0.35	0.05	-	0.00	-	-	0.00
SVZ015	13	Nilahue	River	Summer	2021	-	12.17	0.03	3.63	0.02	-	0.33	13.31	5.40	0.21	0.02	0.02	-	-	0.02
SVZ016	14	Los Venados	River	Summer	2021	0.13	12.38	0.04	2.08	0.01	-	0.10	6.42	1.85	0.08	-	0.00	-	-	0.00
SVZ006	15	Chirre	River	Summer	2021	0.44	3.10	0.02	5.34	0.03	0.11	0.29	8.69	0.96	0.05	0.02	0.01	0.01	0.01	0.00
SVZ010	16	Gol-Gol	River	Summer	2021	0.10	7.06	0.00	4.94	0.03	0.11	0.24	13.00	0.80	0.15	0.01	0.01	0.00	0.01	0.00
SVZ008	17	Chanleufu	River	Summer	2021	0.03	3.82	0.04	0.58	0.01	0.12	0.08	7.63	2.36	0.04	-	0.01	-	-	0.00
SVZ005	18	Coihueco	River	Summer	2021	0.07	4.78	0.06	3.66	0.02	0.14	0.18	9.08	0.40	0.05	0.00	0.00	-	0.00	0.00
SVZ004	19	Blanco at R-225	River	Summer	2021	0.05	4.65	0.07	1.04	0.01	0.07	0.11	15.26	1.28	0.05	-	0.00	-	0.00	0.00
SVZ003	20	Chico	River	Summer	2021	0.20	2.06	0.03	5.78	0.03	-	0.16	6.58	0.75	0.04	0.01	0.01	0.00	0.00	0.00
SVZ001	21	Blanco before Chamiza	River	Summer	2021	0.03	0.57	0.02	12.09	0.06	-	0.17	6.35	0.20	0.05	0.01	0.01	-	0.00	0.00
SVZ002	22	Chamiza	River	Summer	2021	0.14	1.75	0.02	12.87	0.04	-	0.66	8.64	0.50	0.03	0.01	0.01	0.00	0.00	0.00
SVZ115	A	Pemehue	Hot Springs	Winter	2022	-	15.70	< 1.4	39.54	< 0.4	12.50	4.30	< 14	3808.85	< 6	-	-	-	-	-

114

Table 13: Continued

SampleID	ID	Location	Type	Seasson	Year	Ti ppb	V ppb	Cr ppb	Mn ppb	Co ppb	Ni ppb	Cu ppb	Zn ppb	As ppb	Se ppb	Y ppb	La ppb	Ce ppb	Nd ppb	Eu ppb
SVZ024	B	Malleco	Hot Springs	Summer	2021	-	0.74	-	8.79	-	-	-	3.84	1.91	0.29	-	0.03	-	-	0.03
SVZ023	C	Malalcahuello	Hot Springs	Summer	2021	-	12.42	-	0.08	-	-	-	4.96	35.07	0.36	-	0.01	-	-	0.01
SVZ117	D	Molulco-Balboa	Hot Springs	Winter	2022	-	12.10	< 0.07	1.09	< 0.02	< 0.5	< 1	14.00	264.13	4.90	-	-	-	-	-
SVZ045	E	Alpehue	Hot Springs	Summer	2021	-	5.61	-	0.51	-	-	-	4.37	252.55	0.90	-	0.04	0.00	-	0.05
SVZ021	F	Menetue	Hot Springs	Summer	2021	0.65	1.52	0.03	0.74	-	-	0.15	3.05	26.73	0.11	-	0.01	-	-	0.02
SVZ014	G1	Palguin at El Litio	Hot Springs	Summer	2021	1.02	11.80	0.12	0.09	-	-	0.05	5.53	49.09	0.20	-	0.01	-	-	0.02
SVZ020	G2	Palguin at El Mote	Hot Springs	Summer	2021	7.42	1.86	0.05	13.38	0.01	-	-	2.11	21.29	0.23	0.03	0.02	0.02	0.02	0.01
SVZ022	H	Geometricas	Hot Springs	Summer	2021	-	1.27	-	3.06	-	-	-	5.66	135.65	0.87	-	0.05	-	-	0.06
SVZ013	I	Coñaripe	Hot Springs	Summer	2021	0.41	4.30	-	5.15	-	-	-	7.97	881.36	-	-	0.03	-	-	0.03
SVZ012	J	Punulaf	Hot Springs	Summer	2021	0.73	0.10	-	0.84	-	-	-	6.31	9.06	-	-	0.02	-	-	0.02
SVZ011	K	Hipolito Muñoz	Hot Springs	Summer	2021	1.28	0.15	0.18	0.44	-	-	-	11.23	1.47	0.12	-	0.01	-	-	0.02
SVZ009	L	Cerrillos	Hot Springs	Summer	2021	-	<LOQ	-	0.73	-	-	-	6.81	15.09	0.37	-	0.01	-	-	0.01
SVZ133	M	Chihuio	Hot Springs	Winter	2022	-	< 0.6	< 0.07	< 0.01	< 0.02	0.40	0.50	2.20	10.15	< 0.3	-	-	-	-	-
SVZ083	N	Lava 2011	Hot Springs	Summer	2022	-	45.10	< 0.35	10.73	0.36	5.80	< 1	0.00	12.58	< 1.5	-	-	-	-	-
SVZ068	O	Aguas Calientes	Hot Springs	Winter	2021	-	5.50	<0.07	0.98	0.06	0.88	1.44	8.80	442.82	4.38	-	-	-	-	-
SVZ047	1	Malleco	River	Winter	2021	-	<0.60	<0.07	0.49	0.02	<0.10	<0.20	7.30	1.14	<0.30	-	-	-	-	-
SVZ048	2	Cautin	River	Winter	2021	-	3.86	<0.07	2.81	0.04	0.38	<0.20	5.60	1.43	<0.30	-	-	-	-	-
SVZ046	3	Blanco at Cura-cautin	River	Winter	2021	-	0.96	<0.07	5.94	0.05	0.30	<0.20	6.00	1.29	<0.30	-	-	-	-	-
SVZ050	4	Truful-Trulf	River	Winter	2021	-	17.88	<0.07	0.26	0.03	0.38	<0.20	5.30	1.38	<0.30	-	-	-	-	-
SVZ049	5	Allipen	River	Winter	2021	-	9.98	<0.07	4.57	0.06	0.48	<0.20	7.20	1.69	<0.30	-	-	-	-	-
SVZ052	6	Alpehue	River	Winter	2021	-	2.40	<0.07	1.00	0.04	0.38	<0.20	14.80	0.72	<0.30	-	-	-	-	-

Table 13: Continued

| SampleID	ID	Location	Type	Seasson	Year	Ti ppb	V ppb	Cr ppb	Mn ppb	Co ppb	Ni ppb	Cu ppb	Zn ppb	As ppb	Se ppb	Y ppb	La ppb	Ce ppb	Nd ppb	Eu ppb
SVZ057	7	Trancura	River	Winter	2021	-	2.08	<0.07	6.18	0.06	0.41	<0.20	4.60	0.38	<0.30	-	-	-	-	-
SVZ051	8	Voipir	River	Winter	2021	-	11.71	<0.07	0.48	0.03	0.35	<0.20	5.20	0.79	<0.30	-	-	-	-	-
SVZ056	9	Palguin	River	Winter	2021	-	5.89	<0.07	0.26	0.03	0.33	<0.20	4.60	0.91	<0.30	-	-	-	-	-
SVZ053	10	Liquiñe	River	Winter	2021	-	1.33	<0.07	1.55	0.03	0.38	<0.20	9.20	0.60	<0.30	-	-	-	-	-
SVZ063	11	Caunahue	River	Winter	2021	-	<0.60	<0.07	2.86	0.05	0.53	<0.20	12.20	1.23	<0.30	-	-	-	-	-
SVZ060	12	Curriñe	River	Winter	2021	-	<0.60	<0.07	0.76	0.05	0.62	0.44	13.50	0.26	<0.30	-	-	-	-	-
SVZ061	13	Nilahue	River	Winter	2021	-	7.53	<0.07	7.42	0.09	1.13	0.57	7.00	3.21	0.91	-	-	-	-	-
SVZ055	14	Los Venados	River	Winter	2021	-	6.89	<0.07	6.30	0.06	0.43	<0.20	22.00	1.29	<0.30	-	-	-	-	-
SVZ064	15	Chirre	River	Winter	2021	-	1.16	<0.07	3.45	0.04	<0.10	0.37	10.00	0.31	<0.30	-	-	-	-	-
SVZ058	16	Gol-Gol	River	Winter	2021	-	3.16	<0.07	1.13	0.03	0.38	<0.20	4.40	1.03	<0.30	-	-	-	-	-
SVZ062	17	Chanleufu	River	Winter	2021	-	2.41	<0.07	0.70	0.03	0.39	<0.20	8.10	1.38	<0.30	-	-	-	-	-
SVZ065	18	Coihueco	River	Winter	2021	-	2.33	<0.07	2.11	0.04	0.38	<0.20	10.50	0.30	<0.30	-	-	-	-	-
SVZ066	19	Blanco at R-225	River	Winter	2021	-	2.17	<0.07	1.17	0.03	<0.10	<0.20	3.50	0.61	<0.30	-	-	-	-	-
SVZ067	20	Chico	River	Winter	2021	-	<0.60	<0.07	6.00	0.05	<0.10	0.48	4.60	0.16	<0.30	-	-	-	-	-
SVZ069	21	Blanco	River	Winter	2021	-	<0.60	<0.07	16.97	0.12	0.33	<0.20	14.00	0.17	<0.30	-	-	-	-	-
SVZ070	22	Chamiza	River	Winter	2021	-	<0.60	<0.07	10.73	0.06	<0.10	1.79	9.50	0.20	<0.30	-	-	-	-	-

Annex B: Figures
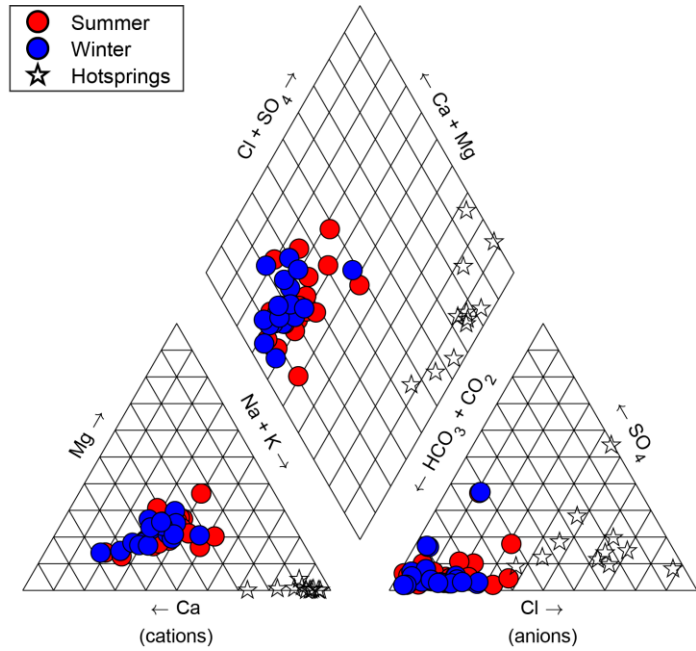
Figure 11: Piper diagram with hot springs and rivers samples taken during summer and winter 2021. The diagram shows that volcanic basins present waters of the calcium/magnesium bicarbonate type, while hot springs are chloride water types. Only Chiuio hot spring show a SO_4 enrichment higher than the others (lower right triangle)
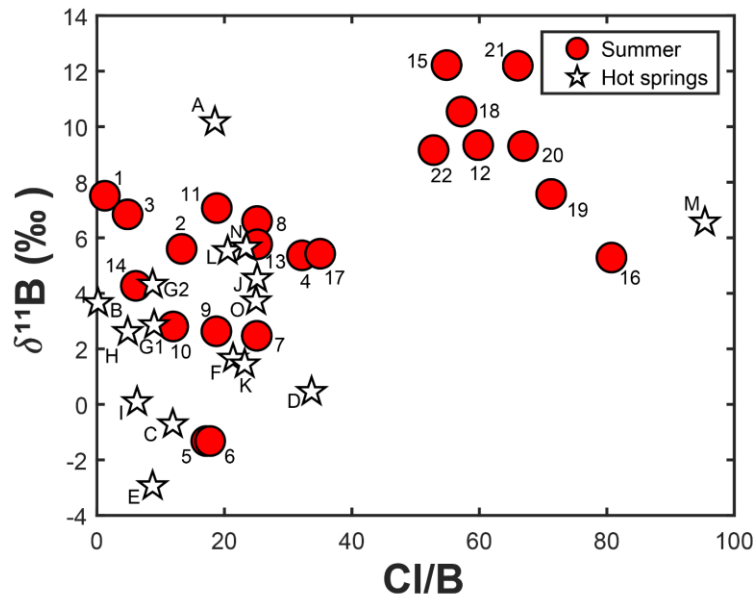

Figure 12: The isotope of B vs Cl/B ratio for CSVZ Rivers sampled in summer and hot springs. Most of the hot springs are located in Cl/B ratio below 40, only Chihuio (M) sample shows higher Cl/N value.

117
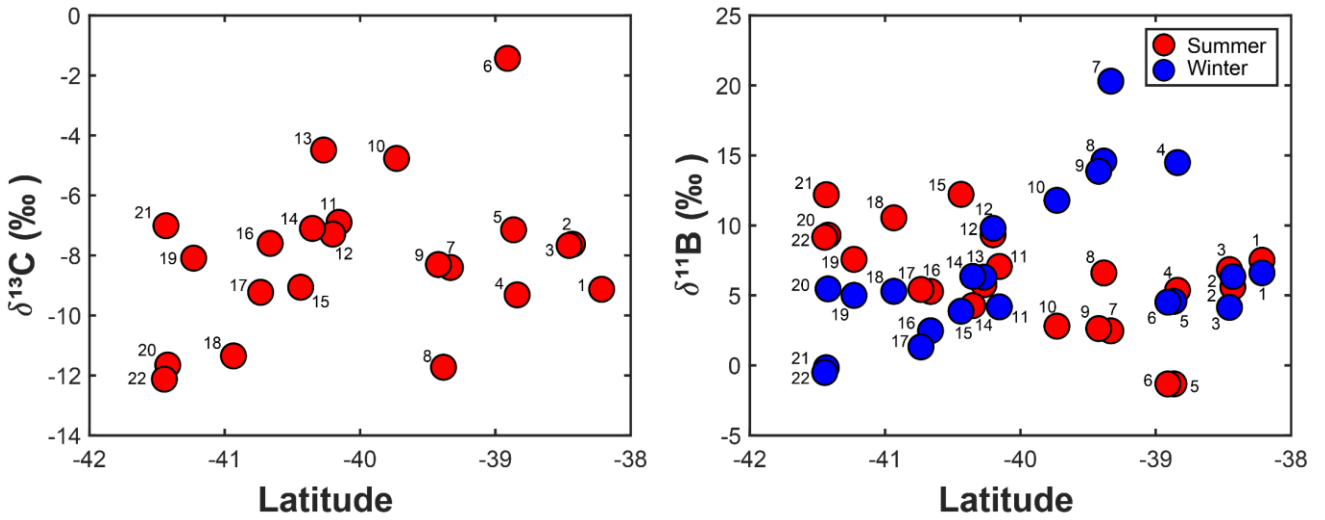
Figure 13: Latitudinal variation of carbon and boron isotopes in the rivers of the Southern Volcanic Zone. In particular, the boron isotope was measured in winter and summer.
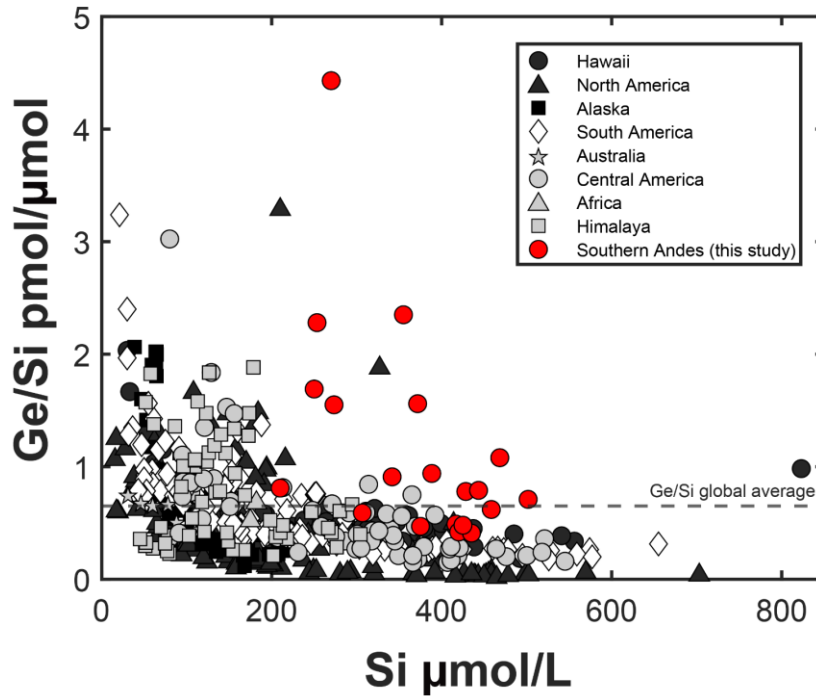
Figure 14: The relation between Ge/Si and Si in CSVZ Rivers (red circles) and rivers around the world. The dashed line marks the Ge/Si global average (0.6 pmol/µmol) (Mortlock and Froelich, 1987; Kurtz et al., 2002, 2011; Chillrud et al., 1994; Lugolobi et al., 2010; Froelich et al., 1985; Anders et al., 2003; Aguirre, 2019; Ameijeiras-Mariño et al., 2018; Baronas et al., 2018). Germanium concentration of Alpehue River (6) was not measured.

Annex C: Assignation of hot springs in each method to determine the thermal input (Cl-Ge/Si)

Given the lack of information regarding the interaction between hydrothermal system and streams in South Volcanic Zone, we decided to use for chloride and germanium/silica methods the hot spring ratios located near to river. In the case that one river has more than one hot spring in the basin; we used the average between thermal springs. Table 12 shows the respective hot spring to each river.
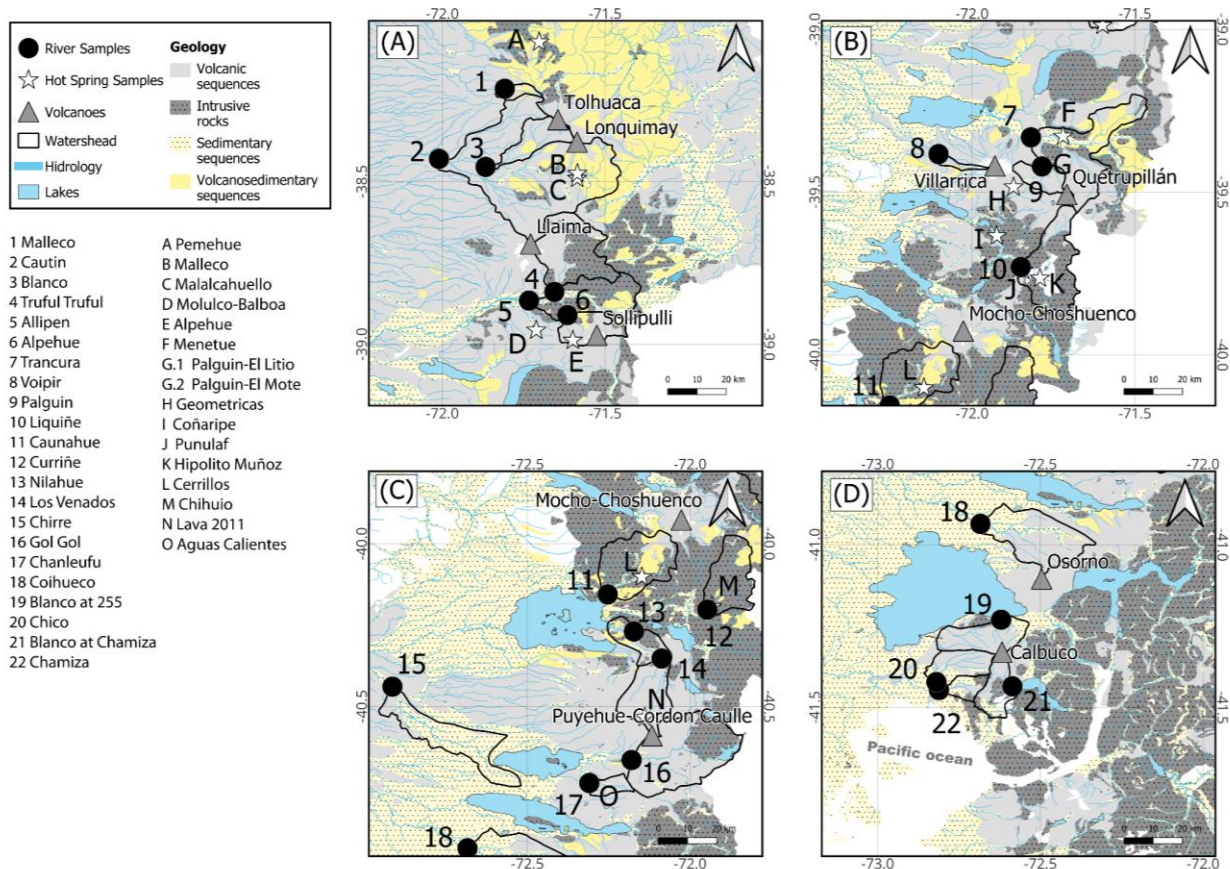

Figure 15: Map with hot springs and river sample's location.

Table 12: Hot spring(s) selected for each river in determination of solutes hydrothermal influence in Cl and Ge/Si method. Hot springs A and D were not considered because of the location out of basins in rivers selected.

ID	River	Latitude	ID Hot spring(s)	Hot spring(s) selected
1	Malleco	-38.2	B,C	Malleco and malalcahuello springs
2	Cautin	-38.4	B,C	Malleco and malalcahuello springs
3	Blanco at Curacautin	-38.5	B,C	Malleco and malalcahuello springs
4	Truful-Trulf	-38.8	E	Alpehue spring
5	Allipen	-38.9	E	Alpehue spring
6	Alpehue	-38.9	E	Alpehue spring
7	Trancura	-39.3	F	Menetue spring
9	Palguin	-39.4	G.1,G.2	Palguin spring
10	Liquiñe	-39.7	J	Punulaf and Hipolito Muños springs
11	Caunahue	-40.2	L	Cerrillo spring
12	Curringue	-40.2	M	Chihuio spring
13	Nilahue	-40.3	N	Lava 2011 spring
14	Los Venados	-40.4	N	Lava 2011 spring
17	Chanleufu	-40.7	O	Aguas Calientes spring

Annex D: Calcite precipitation curves

The PHREEQC code employed for precipitation curves in Figure 5 is based in Pérez-Moreno thesis project and after published in 2021. The code is:

```
#Initial composition of solution.
#Parameters can be adjusted to match different reservoir fluids.
SOLUTION 1
    temp      50
    pH        5 charge
    pe        4
    redox     pe
    units     mol/kgw
    density   1
    C         0.001939
    Ca        0.001 Calcite    0
    [13C]     -7.5 permil      0
    -water    1 # kg

SELECTED_OUTPUT 1
    -file               E:\Magíster\Memoria\PHREEQC\Precipitación-calcita\DEGASS20.sel
    -step               true
    -pH                 true
```

```
        -totals              C
        -calculate_values    R(13C)
        -active              true
        -user_punch          true
END
#Define a fixed volume gas phase and a CaCO3 phase.
#Volume can be adjusted to modify degassing rate.
GAS_PHASE 1
-fixed_volume
-vol 0.1
CO2(g) 0
[13C]O2(g) 0
SOLID_SOLUTION  1
Calcite
-comp Calcite 0
-comp Ca[13C]O3(s) 0
END
#Generate graph
USER_GRAPH 1
-headings TC 13C(aq) 13C(CO2(g)) pH
-axis_titles "TDIC, mmoles" "PERMIL" "pH"
-initial_solutions false
-connect_simulations true
-plot_concentration_vs x
-start
10 GRAPH_X TOT("C")*1e3
20 GRAPH_Y ISO("[13C]"), ISO("R(13C)_CO2(g)")
30 GRAPH_SY -LA("H3O+")
-end
-active true
END
```

In the code was changed the parameter "[13C]" = -7.5‰ and -4.48‰ and T° conditions, while the inorganic carbon concentration was "[C]" = 0.001939 mol/kg. The resulting graphs showed calcite precipitation curve observed at 30°C with -4.48‰ $\delta^{13}C$ conditions, and between 50°C and 30°C, with a variation in $\delta^{13}C$ (-7.5‰).
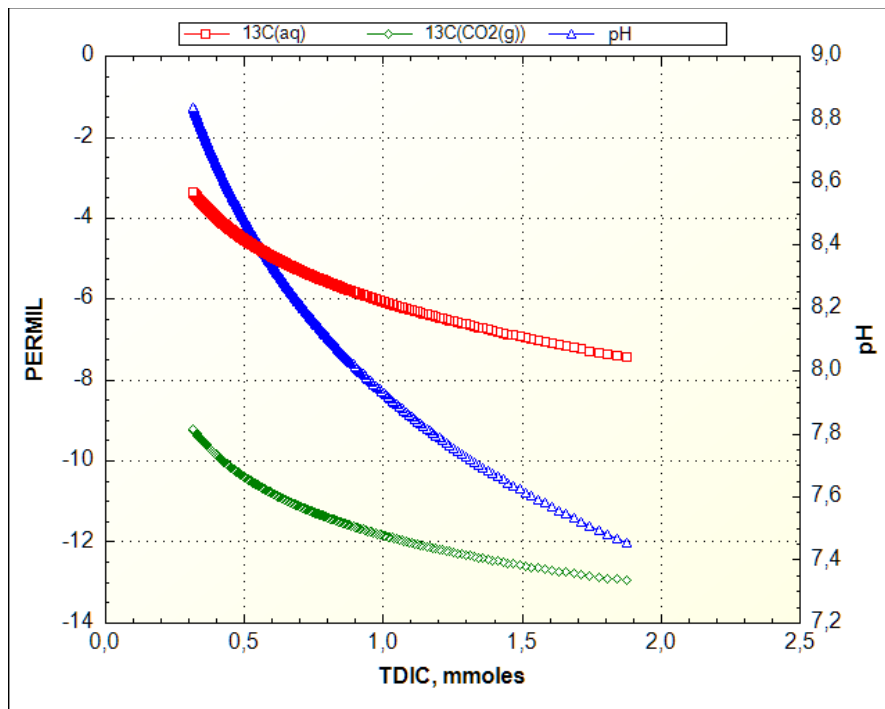
Figure 16: Example of graph obtained from PHREEQC code with respective curves (pH, ^{13}C(aq) and ^{13}C(CO$_2$(g)).

Annex E: Monthly and annual discharge in gaged and ungagged streams

In order to analyze the model used to determine the flow rates of each watershed, a comparison is conducted at those river gauge stations with data available from 1980 to 2022 and the values obtained from the applied linear regression model. Subsequently, the same comparison was carried out within the restricted time frame of 2010 to 2022.

Table 13: Data obtained in 7 gagged streams between 1980-2022 and 2010-2022 compared with model data in the same range of years.

ID	River	Lat.	Lon.	Station Code	Mean annual discharge	N° years with data	Mean annual discharge model
					(2010-2022)		
					(m³/s)		(m³/s)
3	Cautin River	-38.4	-71.0	9123001	71.9	12	66.0
2	Blanco River at Curacautin	-38.5	-71.9	9122002	6.8	12	5.8
10	Liquiñe River	-39.7	71.9	10102001	35.1	12	32.9
11	Caunahue River	-40.2	-72.3	10305001	31.4	12	30.3
15	Chirre River	-40.4	-72.9	10327001	43.2	12	18.1
16	Gol-Gol River	-40.7	-72.2	10322003	49.2	12	52.4
20	Chico River	-41.4	-72.8	10432003	11.0	12	12.6

Tabla 15: Continued.

| ID	River	Lat.	Lon.	Station Code	Mean annual discharge	N° years with data	Mean annual discharge model
					(1980-2022)		
					(m³/s)		(m³/s)
3	Cautin River	-38.4	-71.0	9123001	83.6	42	80.8
2	Blanco River at Curacautin	-38.5	-71.9	9122002	7.6	21	6.9
10	Liquiñe River	-39.7	71.9	10102001	38.9	35	36.8
11	Caunahue River	-40.2	-72.3	10305001	34.9	14	35.3
15	Chirre River	-40.4	-72.9	10327001	44.2	20	20.1
16	Gol-Gol River	-40.7	-72.2	10322003	45.7	13	58.4
20	Chico River	-41.4	-72.8	10432003	11.7	19	13.6
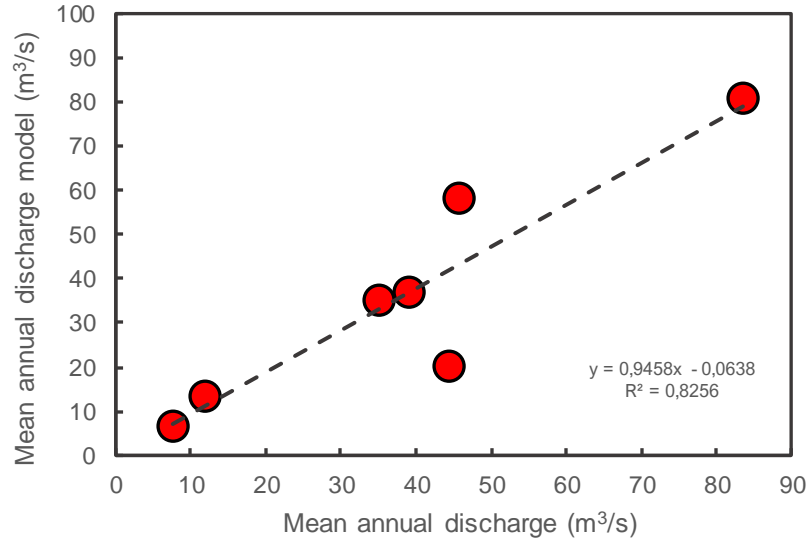
Figure 17: Mean annual discharge row data vs modeled between 1980-2022 in 7 of 22 watersheds selected for this study

Annex F: Time of concentration

Using the Branby Williams (1922) and Kirpich (1940) equations to determine the time of concentration in each basin, we obtained values less than 14 hours, with an average of 6 hours and only 2 rivers showed more than 10 hours (Table 14).

Kirpich (1940)

$$t_c = 3.98 \cdot \left(\frac{L}{S^{0.5}}\right)^{0.77}$$

t_c = time of concentration (min)

L = length stream (km)

S = mean slope (m/m)

Branby Williams (1922)

$$t_c = 14.6 \cdot L \cdot A^{-0.1} \cdot S^{-0.2}$$

t_c = time of concentration (min)

124

L = length stream (km)

S = mean slope (m/m)

A= area (km²)

Table 14: Time of concentration obtained of Kirpich (1940) and Bransby Williams (1922) equation for 22 basins in SVZ.

ID	Name	Area	Slope (S)	Lenght	t_c (hora)	t_c (hora)
		(km^2)	km/km	km	Kirpich	Bransby Williams
1	Malleco River	57.9	0.24	15.3	0.9	3.3
2	Cautin River	1594.7	0.16	82.0	4.0	13.7
3	Blanco River at Curacautin	201.8	0.17	34.7	2.0	7.1
4	Truful-Trulf River	476.0	0.21	19.0	1.2	3.4
5	Allipen River	592.5	0.25	39.7	1.9	6.7
6	Alpehue River	204.7	0.21	14.3	0.9	2.8
7	Trancura River	564.4	0.19	53.3	2.7	9.6
8	Voipir River	39.1	0.18	17.6	1.2	4.2
9	Palguin River	130.8	0.13	10.9	0.9	2.5
10	Liquiñe River	449.2	0.25	37.0	1.8	6.5
11	Caunahue River	456.8	0.30	26.1	1.3	4.4
12	Curriñe River	331.2	0.28	28.4	1.4	5.0
13	Nilahue River	476.8	0.15	37.1	2.2	7.1
14	Los Venados River	297.3	0.15	22.7	1.5	4.6
15	Chirre River	444.3	0.16	69.1	3.5	13.2
16	Gol-Gol River	714.2	0.17	27.0	1.7	4.9
17	Chanleufu River	73.4	0.01	15.2	2.8	5.6
18	Coihueco River	484.2	0.14	52.9	3.0	10.3
19	Blanco River at R-225	267.9	0.08	12.6	1.2	2.9
20	Chico River	198.9	0.17	25.9	1.6	5.3
21	Blanco River before Chamiza	183.2	0.09	14.6	1.3	3.4
22	Chamiza River	91.1	0.06	15.5	1.7	4.3